Limits on Microvalve Design

by

Kenneth H. Chiang

B.S., EE (Massachusetts Institute of Technology) 1992
B.S., CS (Massachusetts Institute of Technology) 1992
M.S., EECS (Massachusetts Institute of Technology) 1992

A dissertation submitted in partial satisfaction of the
requirements for the degree of
Doctor of Philosophy

in

Engineering — Electrical Engineering and Computer Sciences

in the

GRADUATE DIVISION
of the
UNIVERSITY of CALIFORNIA at BERKELEY

Committee in charge:

Professor Ronald S. Fearing, Chair
Professor Seth R. Sanders
Professor Masayoshi Tomizuka

2000

The dissertation of Kenneth H. Chiang is approved:

Chair Date

Date

Date

University of California at Berkeley

2000

Limits on Microvalve Design

Abstract

Limits on Microvalve Design

by

Kenneth H. Chiang

Doctor of Philosophy in Engineering — Electrical Engineering and Computer Sciences

University of California at Berkeley

Professor Ronald S. Fearing, Chair

Microvalve arrays provide the capability of controlling large amounts of power in a very small volume. Two potential applications for such an array are tactile displays and active surfaces. Unfortunately, construction of an array requires a microvalve in the first place.

In this dissertation, we discuss the limitations of microvalve design, starting with single seating and sliding valve designs, and moving on to multiple orifice and multiple stage designs.

Of particular note is the fact that the efficiency of most small actuators is poor at the speeds required to drive a microvalve, and consequently the necessary electrical input power is high. This suggests that a potential pathway to valve miniaturization is a self-driven multistage design, consisting of a fluid-driven secondary stage, and an electrically-driven primary stage that brakes that secondary.

Two realizations of the self-driven design are then set forth— the turbine brake valve (TBV) and the self-oscillating valve with electrostatic clamp— along with the associated experimental results. Calculations indicate that a power savings of up to three orders of magnitude can be

theoretically realized in comparison to a single stage piezoelectrically-driven valve.

Professor Ronald S. Fearing
Dissertation Committee Chair

To my family and friends,

without whom this thesis would not have been written.

Contents

List of Figures

List of Tables

Acknowledgements

I would like to thank my research group— S Avadhanula, G Moy, E Shimada, H Shinoda, U Singh, M Sitti, J Thompson, C Wagner, R Wood, J Yan, and W Zesch, not to mention Professor RS Fearing himself— for their insights and otherwise helpful discussions.

Chapter 1

Introduction

There is a need for a high-force, large-stroke milli-actuator, which can be arrayed for high power density applications.

In realizing such an actuator, pneumatics has a number of advantages:

- Its power density, neglecting valves and compressor, is sufficiently high. For instance, McKibben pneumatic actuators– effectively, flexible tubing that contracts when inflated– have an average power density of 1.1 W/cm^3, and a peak power density of 2.65 W/cm^3[Chou, 1996].
- Its components are simple and economic. Be they composed out of straightforward pistons in cylinders, or membranes stretched over cavities, pneumatic actuators are easy to design.
- Low-cost compressed air supplies are readily available. Most industrial facilities are either fitted with 5 atmosphere (atm) gage supplies, or can be easily retrofitted with such supplies.
- Some leakage is tolerable, since compressed air is nontoxic and nonflammable, as opposed to hydraulic fluids.

However, pneumatics has a number of disadvantages as well:

- Its power efficiency is low, on the order of 5% or so, as discussed below.
- Control is difficult due to air compressibility and flow nonlinearities. As compared with electrical components which largely obey linear relationships, or hydraulic components in which

density is constant and consequently not a factor, pneumatic components are highly nonlinear, as will be addressed in the next chapter.

- Both compressors and piping are required.
- Valves to control pressure or flow are usually large. For example, consider the McKibben actuators mentioned above. The ones in [Chou, 1996] are on the order of 20 cm^3 in volume, and massing approximately 20 g, whereas the valves that drive them are 30 cm^3 in volume, and have five times the mass.
- Pneumatic systems are relatively slow.
- Traditional pneumatic cylinders have high seal friction, leading to greater losses.
- Pneumatic systems are noisy. Mufflers reduce noise, but increase losses and complicate circuit design.

Despite low efficiency, 91 W of pneumatic power can be delivered by a 1.6 mm inner diameter tube with a 6 atm gage power supply, as shown in Section 1.4. With proper modeling of the pneumatic system, such as in [Chou, 1996], [Liu, 1988], or [Ben-Dov, 1995], reasonable control is obtainable.

Additionally, if a compact array of valves existed, the valves could be mounted much closer to the actuators, reducing the line losses and dead volume. A compact array would also have a lower amount of moving mass and consequently have higher bandwidth.

1.1 Contributions of This Thesis

The contributions of this thesis on a chapter-by-chapter basis are as follows:

- In Chapter 1, we provide motivation for attacking the valve design problem, and examine valve performance metrics, in order to provide some ranking among the commericially available valves. For the particular application of a finger-mounted tactile display, the best commercially available valve is five times too large and a hundred times too slow.

- In Chapter 2, we examine the fundamental limitations on valve design, discuss the minimum actuator stroke and force required for a given orifice diameter, and try to address why these size and bandwidth requirements have not been achieved. Some of the key limitations are that the actuators needed to drive moving elements in the valve must be sized to overcome the fluid force, and that the actuators are inefficient at the micro scale.

- Applying the valve design principles of Chapter 2, we explore the design and implementation of two candidate valves in Chapters 3 and 4, both of which are intended to minimize the electrical input power and hence actuator and valve size. In Chapter 3, we explore a rotary valve design that performs promisingly, but suffers from manufacturing difficulties with precision bearings. In Chapter 4, we explore a linear version of the valve design that promises power savings of two to three orders of magnitude over a conventional single-stage piezoelectrically-driven valve. However, this valve design has fabrication difficulties with its brake element.

- Finally, in Chapter 5, we draw conclusions from the two designs of the previous chapters. In particular, multi-stage valve designs are superior to single-stage ones.

1.2 Motivation for Microvalves: Pneumatic Tactile Display

One possible application for such a valve array is in a tactile display[Moy, 2000]. The display that we wish to drive is required to have a density of 25 tactel/cm^2, with each tactel[1] having a peak pressure of 50 N/cm^2, and a stroke of 1.5 mm, at a rate of 100 Hz. In particular, the goal of the tactile display is to provide adequate tactile sensation to the fingertip of the user, in the volume of a sugar cube. The required mechanical power density is then 7.5 W/cm^3, or 0.3 W for a single such actuator.

Other research groups have fabricated tactile displays. Peine and Howe have a 10x1 array of pins actuated by shape memory alloy wire[Peine/Howe]. Unfortunately, the display is large, and

[1] Tactile element.

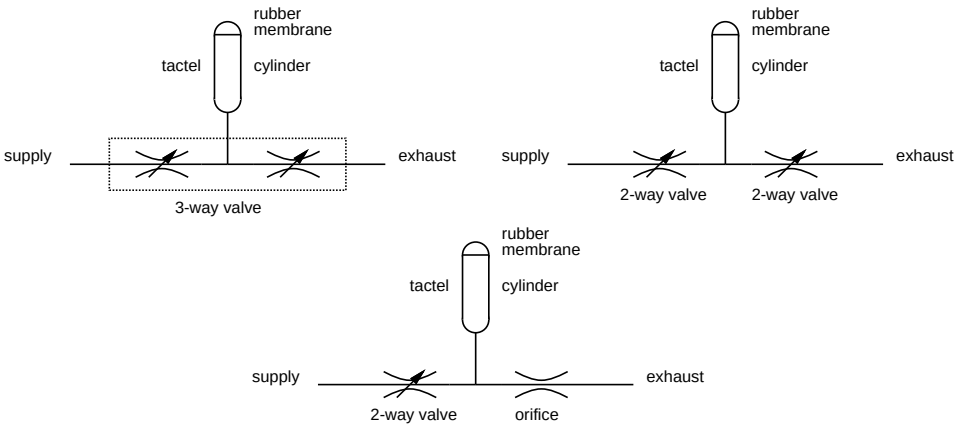

Figure 1.1: Arrangements for pneumatically actuating a tactel[Moy, 2000]. A single 3-way valve (top left), two separate 2-way valves (top right), or a single 2-way valve and a discharge orifice (bottom) may be used.

liquid-cooled to meet the bandwidth requirement. Pawluk and Johnson built a 20x20 array of pins actuated by voice coils[Pawluk]. Though the pin density is much higher than [Moy, 2000], the size of the whole construct, on the order of a floor-standing milling machine, is much greater than could be comfortably mounted on a tabletop, let alone the tip of a finger. Pneumatically-driven pin displays have also been built[Cohn, 1992, Caldwell, 1999].

More recently, pin displays have been replaced by membranes. In the scheme shown in Figure 1.1, a rubber membrane is stretched over a cylinder, forming a chamber. Controlling the air pressure in the chamber controls the pressure applied to a fingertip resting on the rubber membrane. The air pressure may be controlled by a single 3-way valve, two separate 2-way valves, or a single 2-way valve and a discharge orifice. Although pins have simply described dynamics, membranes do not leak, have lower frictional losses, and are relatively easy to construct.

In order to actuate such a tactile display, be it either pin- or membrane-based, there are a number of actuation technologies that can be used. Consider the micro-actuators plotted in Figure 1.2, the data for which was compiled in [Fearing, 1998]. None of these micro-actuators has the required power density of 7.5 W/cm^3. The closest type is rotary electromagnetic; that is, a motor. However, the output of a motor must be geared down in some fashion to achieve the required force

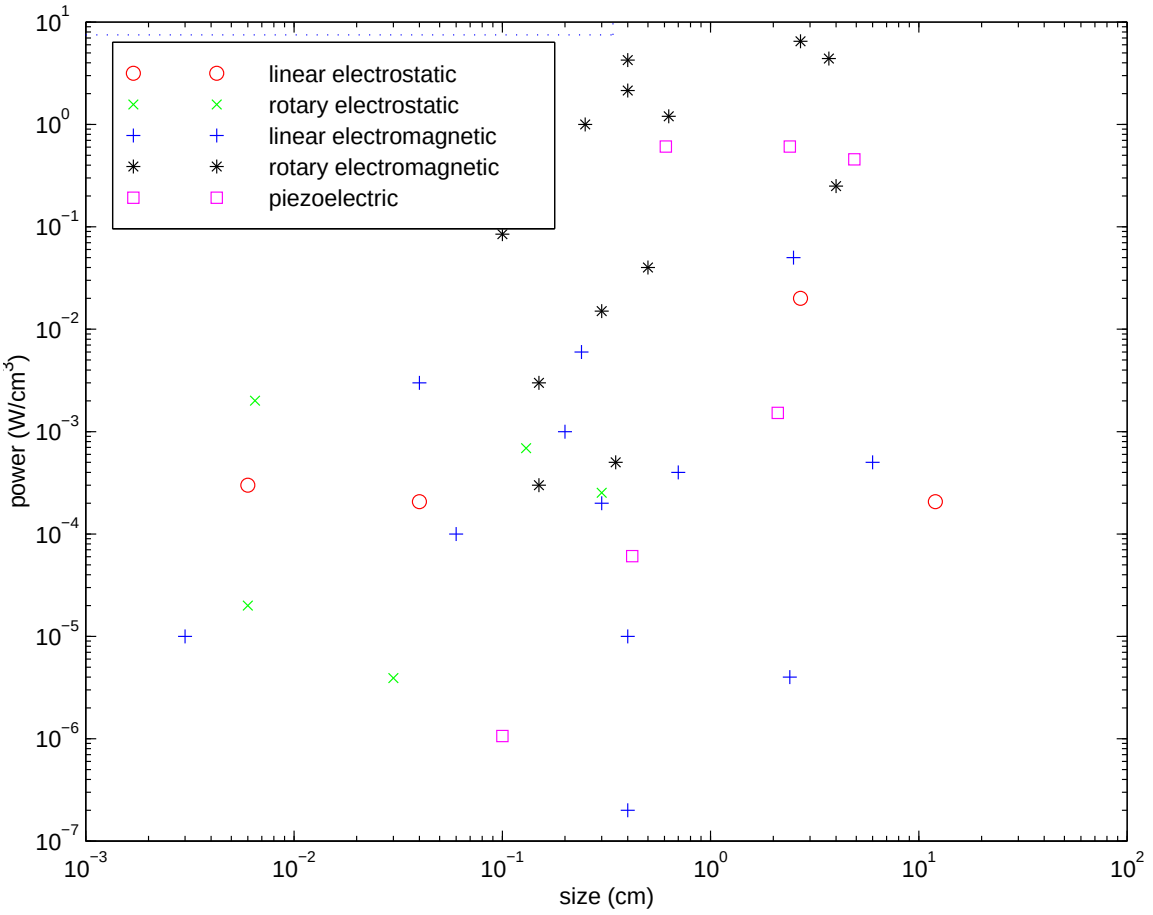

Figure 1.2: Power density v. size for various micro-actuators[Fearing, 1998]. Note that none has the required power density of 7.5 W/cm^3.

and stroke.

On the other hand, pneumatics does not require a transmission in order to apply the desired peak pressure to the fingertip; simply ensuring that air in the cylinder is at 5 atm will ensure that the peak pressure requirement is met.

However, choosing pneumatics means that a compact, relatively fast, arrayable valve is needed, especially if the entire display is to be worn on the finger of the user. Such a prototype display is shown in Figure 1.3.

As with any valve, we need to ensure the pressure drop across the valve is not significant

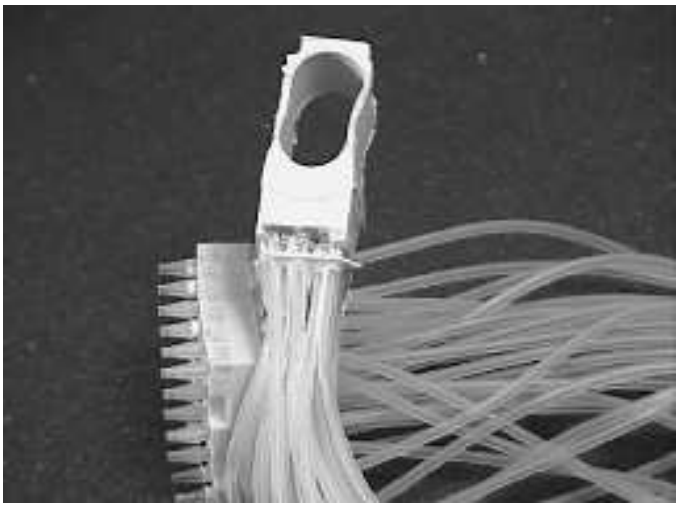

Figure 1.3: A wearable tactile display[Moy, 2000].

enough to greatly impact the resulting working pressure, and reduce the available power that can be transferred to the tactel.

With 25 tactel/cm^2 and a stroke of 1.5 mm, the volume per tactel that must be charged or discharged with fluid is $2 \times 2 \times 1.5$ mm^3, or 6 mm^3, assuming that sidewall thickness can be neglected. This 6 mm^3 volume should be increased by a factor of two to account for the volume of additional piping between the valve and the tactel chamber.

In addition, the tactile display density of 25 tactel/cm^2, together with a total volume limitation of 1 cm^3 imposes a restriction on the volume of the candidate valve.

1.2.1 PWM Control of Pressure

In order to control the pressure in the chamber, two methods can be used— binary or proportional. Of the two, binary control involves simpler mechanisms, but at the cost of more complicated control schemes. The model we employ assumes that the valve governing the pressure in the chamber is either open or closed, and that there is a fixed actuation time required to move the valve from its open state to its closed state and vice versa.

If we control the chamber pressure via pulse-width modulation at 100 Hz, one cycle of

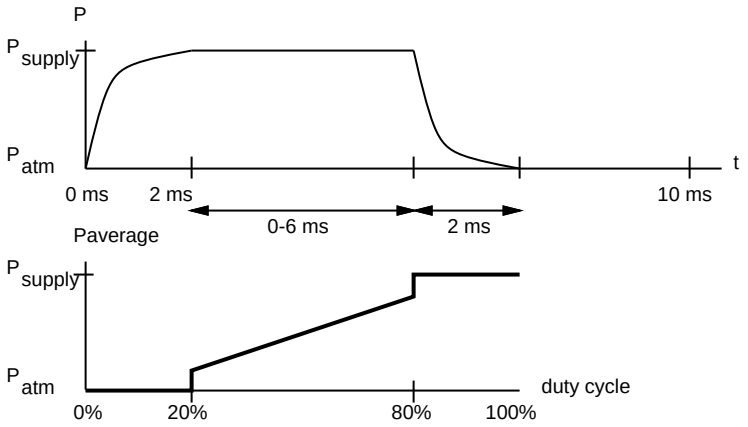

Figure 1.4: A representative 10 ms cycle of chamber pressure; with fixed times for valve actuation and chamber charging and discharging, the only variable is the length of time that the valve is held open. The resulting average pressure in the chamber is sketched as a function of duty cycle.

charging and discharging of the 12 mm^3 volume mentioned above must occur within 10 ms. Consider a representative 10 ms cycle, as illustrated in Figure 1.4. Assuming that the valve is initially closed and the chamber is at atmospheric pressure, the valve then opens and the chamber is charged. After some length of time, the valve then closes and the chamber discharges. Note that the only variable is the length of time that the valve is opened.

In order to have a reasonable range of average chamber pressures the sum of valve actuation time and chamber charging time is chosen to be less than 2 ms. This range of possible duty cycles that can be achieved is then plotted at the bottom of Figure 1.4. Assuming that charging and discharging rates are equal, the duty cycle will range continuously from 20% to 80%, as well as including 0% and 100%, corresponding to when the valve is fully closed or fully open, respectively.

1.2.2 Summary of Valve Requirements for Tactile Display

To summarize, any pneumatic microvalve that we would use in this display must meet the following specifications:

- withstand inlet pressures of up to 6 atm absolute
- does not result in an overly large pressure drop across the valve

- operate at a minimum of 100 Hz
- be able to charge and discharge a 12 mm^3 volume in 2 ms
- occupy a small enough volume to pack 25 such valves in 1 cm^3

1.3 Energy of Compressed Air

Following the development in [Cengel, 1998], the maximum energy contained in an amount of compressed air can be determined by first calculating the specific work potential ϕ_1, neglecting kinetic and potential energy terms:

$$\phi_1 = P_0(v_1 - v_0) - T_0(s_1 - s_0)$$

where P_0, T_0, v_0, and s_0 are the pressure, temperature, specific volume, and specific entropy of the dead state. The dead state is usually that of standard pressure and temperature, or 101 kPa and 25°C.

Treating air as an ideal gas, the first term becomes:

$$\begin{aligned} P_0(v_1 - v_0) &= P_0(\frac{RT_1}{P_1} - \frac{RT_0}{P_0}) \\ &= RT_0(\frac{P_0}{P_1} - 1) \end{aligned}$$

using the ideal gas law and assuming that $T_1 = T_0$.

The second term becomes:

$$\begin{aligned} -T_0(s_1 - s_0) &= -T_0(C_p \ln \frac{T_1}{T_0} - R \ln \frac{P_1}{P_0}) \\ &= RT_0 \ln \frac{P_1}{P_0} \end{aligned}$$

using the entropy change relation for ideal gases with constant specific heats, and assuming that $T_1 = T_0$.

Substituting, we arrive at:

$$\phi_1 = RT_0(\frac{P_0}{P_1} - 1 + \ln \frac{P_1}{P_0})$$

If the compressed air is at 6 atm absolute, ϕ_1 is 82.0 kJ/kg. Taking 1 cm^3 of air at this pressure, the density is 7.1 kg/m^3 and the corresponding mass is 7.1 mg. The work potential of this mass is then 0.58 J.

If the compressed air is at 1000 psi gage, or 69 atm absolute, ϕ_1 is 277.9 kJ/kg. Taking 1 cm^3 of air at this pressure, the density is 81.5 kg/m^3 and the corresponding mass is 81.5 mg. The work potential of this mass is then 22.7 J.

Compare this to an AA battery.[2] The volume energy density is 220 Wh/liter, [3] or 792 J/cm^3. Comparing this number to those above for compressed air, pneumatics does not appear to be a good source of energy. However, the energy density per unit mass for the AA battery is 260 kJ/kg, and in that respect, compressed air becomes a more viable alternative.

1.4 Power Transmission of Compressed Air

Consider an air motor driving a purely resistive load. To determine its efficiency, we choose a representative air motor, an Ingersoll-Rand M002RVR006AR3, and determine its efficiency when it delivers maximum power to its load. This maximum power is 0.17 hp, or 130 W, with an air consumption of 9.7 scfm, or 4.6 l/s, at a gage pressure of 90 psi, or 6.1 atm; the input fluid power is the product of the pressure across the motor and the volume flow rate, or 2.8 kW. The corresponding efficiency is then 4.5%.

This compares poorly to the efficiency of an electric motor driving a purely resistive load– most motors operate in the range of 80% to 90%.

However, it is another issue if there is a readily available power source whose output can be switched to control the power delivered to the load. The contention in this thesis is that this situation is much more applicable on the microscale.

Because we propose to use pneumatics, we must first understand the operation of a valve

[2] 14 mm diameter, 50 mm height, 23.5 g.
[3] http://www.porta-power.com/battery.htm

that controls the fluid power supplied to a pneumatic load. Therefore, we analyze the electrical analogue of the pneumatic circuit, as in Figure 1.5.

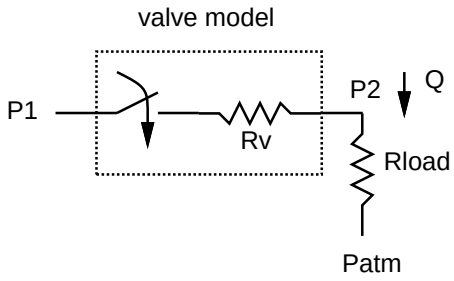

Figure 1.5: Electrical analogue for valve controlling fluid power to a pneumatic load. The valve is modeled as a switch in series with a nonlinear flow restriction, following the orifice equation. The pneumatic load is assumed to be purely resistive.

The valve is modeled as a switch in series with a nonlinear flow restriction that obeys the orifice equation:

$$\dot{m} = C_c A_0 \sqrt{P_1 \rho_1 \frac{2k}{k-1}} \sqrt{(\frac{P_2}{P_1})^{\frac{2}{k}} - (\frac{P_2}{P_1})^{\frac{k+1}{k}}}$$

where $\dot{m}$ is the mass flow rate, C_c is the contraction coefficient, A_0 is the area of the orifice, P_1 is the absolute upstream pressure, ρ_1 is the upstream density, P_2 is the absolute downstream pressure, and k is the ratio of specific heats. This equation is only valid when the ratio of downstream and upstream pressures $\frac{P_2}{P_1}$ is greater than 0.528. If the ratio is less than this value, then the flow is choked and 0.528 should be substituted for $\frac{P_2}{P_1}$.

The pneumatic load is assumed to be purely resistive, so that the circuit is dominated by the action of the valve. This assumption of the ideal resistive load also permits the power delivered to the load to simply be the product of the pressure drop across the load and the volume flow rate though the load. Assuming the valve is turned on and the load pressure is at absolute pressure P_2, the pressure ratio $\frac{P_2}{P_1}$ is known and the mass flow rate w through the flow restriction can be found.

Under the assumption of isentropic flow, the ratio $\frac{P}{\rho^k}$ is constant for any point in the flow. Comparing two points 1 and 2, if the pressure ratio between both points is known, and the density

parameter	symbol	value
ratio of specific heats	k	1.4
gas constant of air	R	287 J/kg – K
contraction coefficient	C_c	0.6
supply pressure	P_1	6 atm absolute
supply temperature	T_1	293 K
supply density	ρ_1	7.21 kg/m^3
atmospheric pressure	P_{atm}	1 atm absolute

Table 1.1: Parameter summary for fluid power calculation.

at one point is known, then

$$\rho_2 = \rho_1 (\frac{P_2}{P_1})^{\frac{1}{k}} \tag{1.1}$$

This equation is invalid if a shock occurs. Additionally, clearly entropy cannot be the same upstream and downstream of the orifice, because of all the turbulence downstream of the orifice. Both of these problems will be ignored in this analysis.

With the mass flow rate $\dot{m}$ and the density ρ, the volume flow rate Q can then be determined as:

$$Q = \frac{\dot{m}}{\rho} \tag{1.2}$$

Finally, the power delivered to the load is just the product of the pressure across the load, and the volume flow rate into the load.

With the parameters summarized in Table 1.1, the mass flow rate, volume flow rate, velocity through orifice, and power delivered to load, all as a function of absolute pressure across the load, are given for an orifice of diameter 1.6 mm in Figure 1.6, and for an orifice of diameter 0.5 mm in Figure 1.7.

The maximum power delivered to the load occurs at a load pressure of 4.2 atm. For an orifice of diameter 1.6 mm, the volume flow rate is 0.28 l/s, with a corresponding air velocity of 240 m/s. The power delivered to the load is 92 W. For an orifice of diameter 0.5 mm, the volume flow rate is 0.028 l/s, with the same air velocity. The power delivered to the load is 9.1 W.

If the assumption of the purely resistive load is valid, 9.1 W of pneumatic power is available

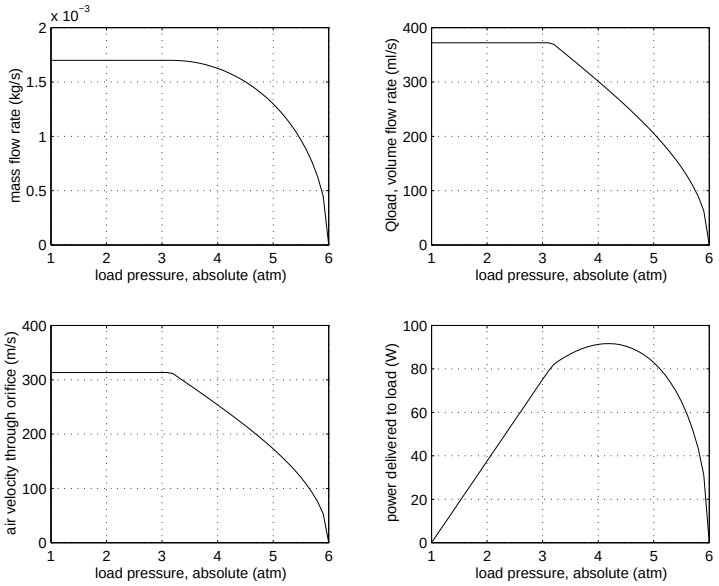

Figure 1.6: Mass flow rate, volume flow rate, velocity through orifice, power delivered to load, all as a function of absolute pressure across the load. The orifice diameter is 1.6 mm.

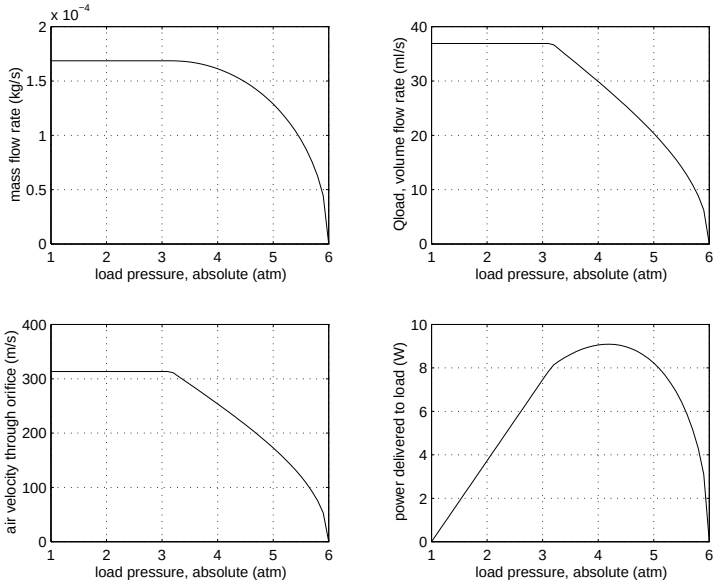

Figure 1.7: Mass flow rate, volume flow rate, velocity through orifice, power delivered to load, all as a function of absolute pressure across the load. The orifice diameter is 0.5 mm.

to drive one tactel in the display.

However, we wish to deliver power to a capacitive load. From Section 1.3, we know that the specific work potential of air at 6 atm absolute is 82.0 kJ/kg. The 12 mm^3 chamber volume mentioned in Section 1.2 then has a work potential of 7 mJ; if charged and discharged at the rate of 100 Hz, 0.7 W of pneumatic power are available, which fortunately is still more than the required 0.3 W per tactel, assuming that all the pneumatic power can be transformed into mechanical power.

A rough estimate of the power delivery capability of a valve can be obtained by multiplying the maximum flow rate through the valve by the maximum pressure drop across the valve; this is termed the *output power* for the valve. To apply this metric to the 0.5 mm orifice data, we first need to determine the volume flow rate; this can be obtained if the density ρ is known. However, there is then the issue of what density to use. There are two ways to determine this, the most straightforward being the average density between the upstream and downstream pressures; this then corresponds to an average density of 4.2 kg/m^3.

The more complicated way assumes that the density should be that associated with the lowest downstream pressure corresponding to the onset of choked flow. Because the flow is choked when the ratio of downstream to upstream pressure is less than 0.528, and the upstream pressure is 6 atm absolute, the corresponding downstream pressure is then 3.2 atm absolute. Using this pressure and Equation 1.1, we arrive at a density of 4.6 kg/m^3. Fortuitously, this value is close to the average density given above.

If we remain with the density of 4.6 kg/m^3, the corresponding maximum volume flow rate is $3.7 \cdot 10^{-5}$ m^3/s. With a pressure difference of 5 atm across the load, the output power for this valve is then 19 W. Note that the output power greatly overestimates the actual power delivered to a capacitive load, but at least it is within a factor of two of the power delivered to an ideal resistive load.

1.5 A Survey of Available Valves

A brief survey of available small pneumatic valves with electrical inputs is plotted in Figure 1.8 and tabulated in Table 1.2. Note that for the valves in the survey, the DC power density

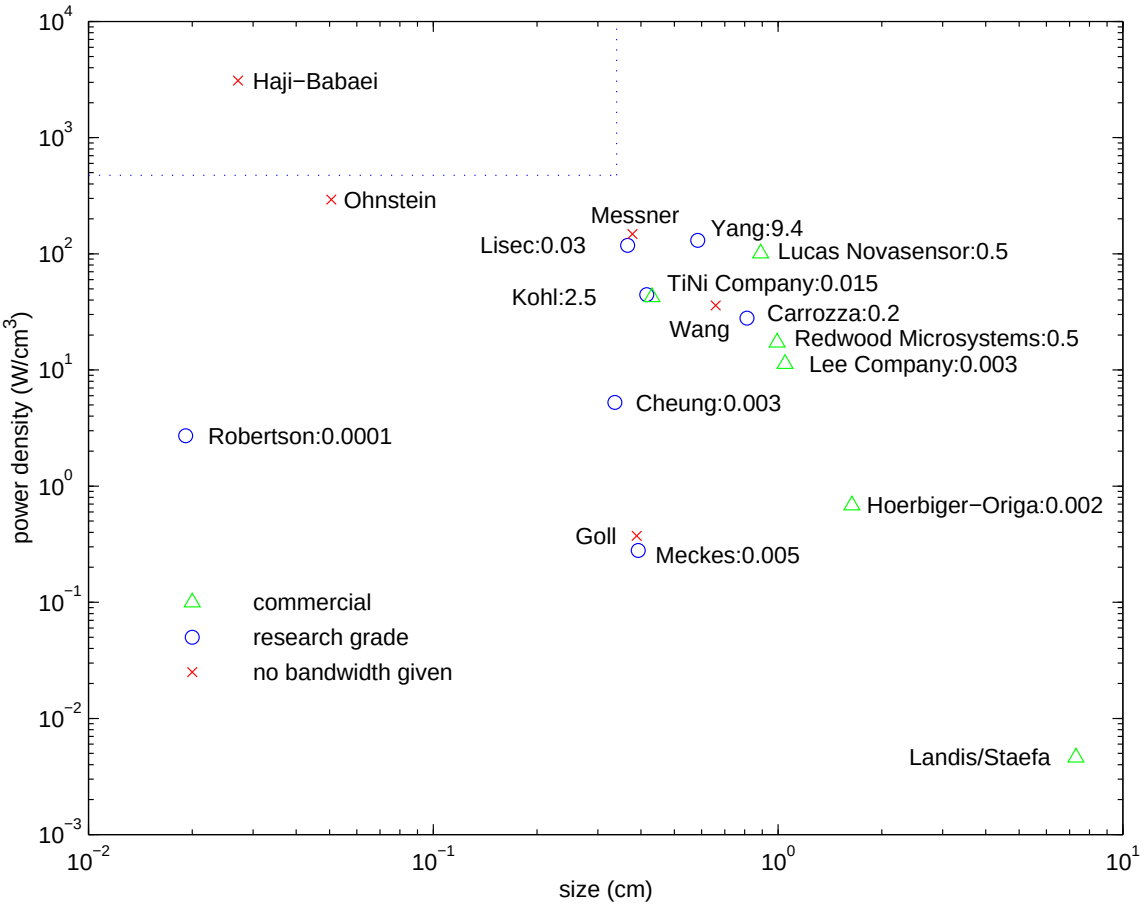

Figure 1.8: DC power density v. size, with size defined as the cube root of the volume, for both research-grade valves [Cheung, 1997, Carrozza, 1996, Goll, 1997, Haji-Babaei, 1997, Kohl, 1999] [Lisec, 1996, Meckes, 1997, Messner, 1998, Ohnstein, 1990, Robertson, 1996] [Yang, 1997, Wang, 2000] and commercial valves [Hoerbiger-Origa, Landis/Staefa, Lee Company] [Lucas Novasensor, Redwood Microsystems, TiNi Alloy]. Designs are labeled with author or company name, and actuation time in seconds. Valves with no data on bandwidth are indicated with crosses. Any designs in the upper left corner with actuation times less than 2 ms would satisfy the power density and size requirements for the tactile display of [Moy, 2000].

is defined as the output power divided by the volume of the valve, and that the output power is defined in Section 1.4 as the maximum pressure drop across the valve multiplied by the maximum volume flow rate through the valve. Because orifice size is usually not provided, it is not possible to

perform an analysis similar to that given in Section 1.4 for every valve, so the output power metric discussed at the end of that section is used instead. Note also, extrapolating from the 0.5 mm orifice data from the same section, that the output power metric may overestimate the available pneumatic power by a factor of two.

If we use the 0.5 mm orifice data of the previous section as a baseline, we would need 19 W/tactel, and at 25 tactel/cm^3, this would correspond to a power density of 480 W/cm^3 that would be required for the valve to drive the tactile display of [Moy, 2000]. As for the size, from the desired packaging density of 25/cm^3, each valve should have a side dimension of 0.34 cm, but the existing valves that satisfy the power density requirement are then too large.

For those valves that actually fall within the desired upper left corner of Figure 1.8, no actuation time has been given. Having the desired volume and DC power density is not enough—if the valve cannot be actuated within 2 ms, the load pressure cannot be controlled via PWM at 100 Hz.

	type	max flow rate max pressure drop	input power	output power	DC power gain	volume	actuation time
Shikida, Sato Hitachi	electrostatic slider	??? 300 kPa	???	???	???	???	???
Lee, Hamilton LLNL	electrostatic poppet	??? 24 kPa	$<$ 1mW	???	???	$0.2 \times 0.5 \times 0.5$ mm^3	0.1 s
Robertson, Wise U Michigan	electrostatic poppet	$8.7 \cdot 10^{-2}$ sccm 100 torr	$2.1 - 8.4$ μW	19 μW	2–9	$1 \times 0.7 \times 0.01$ mm^3	100 μs calculated
Hirano, Yanagisawa NTT	electromagnetic poppet	???	???	320 μW	???	???	???
Meckes, Benecke U Bremen	electromagnetic poppet	$2 - 20$ ccm expected $10 - 50$ kPa expected	340 mW	330 μW– 17 mW	0.001– 0.05	$4 \times 4 \times 3.8$ mm^3	5 ms expected
Goll, Bacher Karlsruhe, Germany	electrostatic slider	0.2 ml/s 110 kPa	???	22 mW	???	5 mm diam 3 mm	???
Ohnstein, Fukiura Honeywell	electrostatic poppet	150 sccm 114 mm Hg	???	38 mW	???	$3.6 \times 3.6 \times 0.01$ mm^3	???
Haji-Babaei, Kwok U New South Wales	electrostatic poppet	6 ccm 90 psi	???	62 mW	???	$0.5 \times 0.2 \times 0.2$ mm	???
Cheung, Berlin Xerox	electrostatic poppet	5 scfh 5 kPa	???	0.20 W	???	$5.8 \times 4.1 \times 1.6$ mm^3	3 ms
DPV Landis/Staefa	piezoelectric poppet	15 scim 15 psi	???	1.8 W	???	$150 \times 51 \times 51$ mm^3	???
Yang, Tai Caltech	thermopneumatic poppet	1.3 l/ min 20 psi	280 mW	3.0 W	11	$4.8 \times 5.8 \times 2.0$ mm^3	???
P9-NG-P-LR Hoerbiger-Origa	piezoelectric poppet	1.5 l/ min 1.2 bar	7 mW	3 W	430	$30 \times 19 \times 7.7$ mm^3	$<$ 2 ms
Kohl, Skrobanek Karlsruhe, Germany	SMA poppet	1600 sccm 1.2 atm	0.2 W	3.2 W	16	$6 \times 6 \times 2$ mm^3	2.5 s
TiNi microvalve TiNi Alloy	SMA poppet	1 l/ min 30 psi	$<$ 200mW	3.4 W	17	$8 \times 5 \times 2$ mm^3	10 ms on 15 ms off
Lisec, Wagner ISiT, Berlin	electrostatic bistable, poppet	500 ml/ min 7 bar	1.5 W	5.8 W	3.9	$7 \times 7 \times 1$ mm^3	$10 - 30$ ms
Messner, Muller IMIT, Villingen- Schwenningen	thermal poppet	800 ml/ min 600 kPa	1 W	8 W	8	$6 \times 6 \times 1.5$ mm^3	???
LHD A05 Lee Company	electromagnetic poppet	123 ml/s 15 psi	550 mW	13 W	24	7.1 mm diam, 29 mm	3 ms
Carrozza, Dario Pisa, Italy	SMA poppet	1.75 slm 0.5 MPa	???	15 W	???	6 mm diam, 19 mm	0.2 s
NC-1500 Redwood Microsystems	thermopneumatic poppet	1500 sccm 100 psi	500 mW typ	17 W	34	13 mm diam, 7.4 mm	500 ms
Williams, Maluf Lucas Novasensor	thermal slider	6.7 l/ min 10 bar	1.2 W	71 W	59	15 mm diam, 4 mm	500 ms
Wang, Kao SUNY, Stony Brook	thermal? slider	4500 sccm 20 psi	250 mW– 500 mW	6.9 W	14–28	9 mm diam, 4.5 mm	???

Table 1.2: Valve survey data.

Chapter 2

Principles of Valve Design

2.1 Basic Pneumatics

In studying pneumatics, the easiest way to proceed is by identifying the appropriate electrical analogues. Pressure P is the equivalent of voltage, and mass flow rate $\dot{m}$ the equivalent of current. However, power is the product of pressure and volume flow rate q, which is related to mass flow rate by the density ρ: $\dot{m} = \rho q$.

Assuming that air can be treated as an ideal gas, we have the well-known ideal gas relationship:

$$P = \rho RT$$

where T is the gas temperature and R is the gas constant. Thus, to fully determine the state of the air at any point in a pneumatic system, we also need to keep track of either the density or the temperature.

However, for small systems with small time constants, the time the air spends in the system is very low; effectively, little heat exchange occurs between the system and its surroundings. So, under the additional assumption that any process through which the air undergoes is adiabatic, and because the air is considered an ideal gas, the isentropic relations, assuming constant specific heats,

can be used to determine the state of the air from the pressure only:

$$\frac{P_2}{P_1} = (\frac{\rho_2}{\rho_1})^k = (\frac{T_2}{T_1})^{\frac{k}{k-1}}$$

where k is the ratio of specific heats.

Next to understand are the constitutive relationships of various pneumatic components. The most basic of these components are:

- the orifice
- the fixed-volume cylinder
- the variable-volume cylinder
- and the pneumatic line.

2.1.1 The Orifice

Following the development in [Stadler, 1995], assume the fluid is inviscid; that is, there are no shear forces.

Starting from Euler's equation for one dimensional flow in the x direction:

$$-\frac{dP}{dx} = \rho(\frac{dv}{dt} + v\frac{dv}{dx})$$

If the flow is steady, $\frac{dv}{dt} = 0$, so:

$$-\frac{dP}{dx} = \rho v\frac{dv}{dx}$$

In differential form:

$$\frac{1}{\rho}dP + vdv = 0$$

If the gas is ideal and isentropic:

$$\begin{aligned} \frac{P}{\rho^k} &= C \\ P &= C\rho^k \\ dP &= Ck\rho^{k-1}d\rho \end{aligned}$$

Substituting this into the differential form gives:

$$\begin{aligned} \frac{1}{\rho} Ck\rho^{k-1} d\rho + vdv &= 0 \\ Ck\rho^{k-2} d\rho + vdv &= 0 \end{aligned}$$

Integrating this gives:

$$\frac{Ck}{k-1}\rho^{k-1} + \frac{1}{2}v^2 = \text{const}$$

Since $P = C\rho^k$,

$$\frac{k}{k-1}\frac{P}{\rho} + \frac{1}{2}v^2 = \text{const}$$

Referring to Figure 2.1, at upstream station 1:

$$\frac{k}{k-1}\frac{P_1}{\rho_1} + \frac{1}{2}v_1^2 = \text{const}$$

At downstream station 2:

$$\frac{k}{k-1}\frac{P_2}{\rho_2} + \frac{1}{2}v_2^2 = \text{const}$$

Subtracting station 1 from station 2:

$$\begin{aligned} \frac{k}{k-1}[\frac{P_2}{\rho_2} - \frac{P_1}{\rho_1}] + \frac{1}{2}[v_2^2 - v_1^2] &= 0 \\ v_2^2 - v_1^2 &= \frac{2k}{k-1}[\frac{P_1}{\rho_1} - \frac{P_2}{\rho_2}] \\ v_2^2 - v_1^2 &= \frac{P_1\rho_1}{\rho_2^2}\frac{2k}{k-1}[\frac{\rho_2^2}{\rho_1^2} - \frac{P_2\rho_2}{P_1\rho_1}] \end{aligned}$$

Since $\rho_1 = (\frac{P_1}{C})^{\frac{1}{k}}$ and $\rho_2 = (\frac{P_2}{C})^{\frac{1}{k}}$:

$$v_2^2 - v_1^2 = \frac{P_1\rho_1}{\rho_2^2}\frac{2k}{k-1}[(\frac{P_2}{P_1})^{\frac{2}{k}} - (\frac{P_2}{P_1})^{\frac{k+1}{k}}]$$

Assuming that the velocity at station 1 is zero:

$$v_2 = \frac{1}{\rho_2}\sqrt{P_1\rho_1\frac{2k}{k-1}}\sqrt{(\frac{P_2}{P_1})^{\frac{2}{k}} - (\frac{P_2}{P_1})^{\frac{k+1}{k}}}$$

Assume that the fluid flows through an orifice of cross-sectional area A_0, resulting in an actual flow of cross-sectional area A_2, also known as the *vena contracta*, as shown in Figure 2.1. The

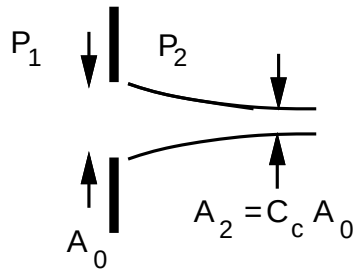

Figure 2.1: The orifice equation applies when a fluid flows through a constriction with cross-sectional area A_0 from a region at pressure P_1 to a region of lower pressure P_2. The product of the empirical contraction coefficient C_c and A_0 gives the actual cross-sectional area of the flow.

empirically determined coefficient that relates A_2 to A_0 is known as the contraction or discharge coefficient, denoted C_c. Depending on the geometry of the orifice, the coefficient takes on values from 0.6 to 1.0. In the case of a sharp-edged orifice, $C_c = 0.6$; if the edges are rounded or flattened, C_c may rise to 0.8 or 0.9[Blackburn, 1960, p. 181], and is exactly equal to 1.0 if the orifice geometry follows that of a streamline on the outermost edge of the flow[Munson, 1994, p. 122]. With the contraction or discharge coefficient as C_c, then the volume flow rate is:

$$\begin{aligned} q &= A_2 v_2 \\ &= C_c A_0 v_2 \\ &= C_c A_0 \frac{1}{\rho_2} \sqrt{P_1 \rho_1 \frac{2k}{k-1}} \sqrt{(\frac{P_2}{P_1})^{\frac{2}{k}} - (\frac{P_2}{P_1})^{\frac{k+1}{k}}} \end{aligned}$$

The associated mass flow rate is then:

$$\dot{m} = C_c A_0 \sqrt{P_1 \rho_1 \frac{2k}{k-1}} \sqrt{(\frac{P_2}{P_1})^{\frac{2}{k}} - (\frac{P_2}{P_1})^{\frac{k+1}{k}}}$$

This is sometimes referred to as the orifice equation. Note that all pressures given are absolute pressures, not gage pressures.

If the downstream pressure is much lower than the upstream pressure, the flow will be choked; that is, limited by the speed of sound. This can be derived by maximizing v_2 above; the ratio of pressures at which this maximum occurs is:

$$\frac{P_2}{P_1} = 0.528$$

In short, if $\frac{P_2}{P_1} > 0.528$, the flow is unchoked and

$$v_2 = \frac{1}{\rho_2}\sqrt{P_1\rho_1\frac{2k}{k-1}}\sqrt{(\frac{P_2}{P_1})^{\frac{2}{k}} - (\frac{P_2}{P_1})^{\frac{k+1}{k}}}$$

If $\frac{P_2}{P_1} \leq 0.528$, the flow is choked and

$$\begin{aligned} v_2 &= \sqrt{kRT} \\ &= \sqrt{(1.4)(286.9J/kgK)(273K)} = 331.1\ m/s \quad \text{for } T = 273 \text{ K} \\ &= \sqrt{(1.4)(286.9J/kgK)(298K)} = 346.0\ m/s \quad \text{for } T = 298 \text{ K} \end{aligned}$$

In summary, the mass flow rate can be obtained from:

$$\dot{m} = \begin{cases} C_c A_0 \sqrt{P_1\rho_1\frac{2k}{k-1}}\sqrt{(\frac{P_2}{P_1})^{\frac{2}{k}} - (\frac{P_2}{P_1})^{\frac{k+1}{k}}} & \text{if } \frac{P_2}{P_1} \leq 0.528 \\ C_c A_0 \sqrt{P_1\rho_1\frac{2k}{k-1}}\sqrt{(0.528)^{\frac{2}{k}} - (0.528)^{\frac{k+1}{k}}} & \text{otherwise} \end{cases} \tag{2.1}$$

where C_c is the contraction coefficient, A_0 is the effective cross-sectional area of the orifice, P_1 is the upstream pressure, ρ_1 is the upstream density, P_2 is the downstream pressure, and k is the ratio of specific heats.

This equation is valid under the assumptions that the flow is steady, inviscid, and one-dimensional, and that the upstream velocity is low.

The orifice equation, although unfortunately nonlinear, provides a method to determine the mass flow rate from the upstream and downstream pressures; it is the constitutive relationship for the pneumatic analogue of a nonlinear resistor.

An orifice of 0.5 mm in diameter results in a cross-sectional area that provides a reasonably short charging time, as discussed in Subsection 2.1.5. With this charging time, an acceptable step response can be then achieved with the PWM control method, mentioned in Subsection 1.2.1.

2.1.2 The Fixed-Volume Cylinder

To find the relationship between the mass flow rate $\dot{m}$ and the rate of change of pressure $\dot{P}$ for an ideal gas inside a cylinder of fixed volume V, we note that

$$m = \rho V$$

where m is the mass inside the cylinder, V is the cylinder volume, and ρ is the density of the gas inside. Differentiating with respect to time gives

$$\dot{m} = V\dot{\rho} + \rho\dot{V}$$

but the second term can be neglected if the volume is fixed.

An ideal gas obeying the polytropic relation exhibits the following relation between its pressure P and its density ρ:

$$P = C\rho^n$$

where C is some constant, and n is either 1 in the isothermal case or k, the ratio of specific heats c_p/c_v, in the adiabatic case. Differentiating with respect to time gives

$$\dot{P} = Cn\rho^{n-1}\dot{\rho} = \frac{Ck}{\rho}\frac{P}{C}\dot{\rho} = \frac{nP}{\rho}\dot{\rho}$$

Since the gas is ideal, $\frac{P}{\rho} = RT$, so

$$\dot{P} = nRT\dot{\rho}$$

Substituting this into the expression above for $\dot{m}$ leads to

$$\dot{m} = V\dot{\rho} = \frac{V}{nRT}\dot{P}$$

or

$$\dot{P} = \frac{nRT}{V}\dot{m} \tag{2.2}$$

For very small volumes, the process can be assumed to be adiabatic, because the volume charges and discharges quickly enough that no heat transfer occurs. For much larger volumes, the charging and discharging happens much more slowly that heat transfer can occur, so that the isothermal case is valid.

One last thing of note: what is to be done about the temperature T? Clearly, if the system is isothermal, T is constant. However, if the system is adiabatic, then T should be replaced utilizing one of the isentropic relations. On the other hand, [Shearer, 1956] remarks that there really is not

much difference between replacing T and leaving it equal to the stagnation temperature, which is simply the temperature of the air entering the cylinder.

The fixed volume cylinder is the pneumatic analogue of the electrical capacitor, with a capacitance of $\frac{V}{nRT}$.

2.1.3 The Variable-Volume Cylinder

To find the relationship between the mass flow rate $\dot{m}$ and the rate of change of pressure $\dot{P}$ for an ideal gas inside a cylinder of variable volume V, we begin as above with

$$\dot{m} = V\dot{\rho} + \rho\dot{V}$$

Once again, from the polytropic relation we obtain

$$\dot{P} = nRT\dot{\rho}$$

which can be substituted into the above to give

$$\dot{m} = \frac{V}{nRT}\dot{P} + \rho\dot{V}$$

Solving for $\dot{P}$,

$$\dot{P} = \frac{nRT}{V}(\dot{m} - \rho\dot{V})$$

If V is composed of an initial volume V_0 and a displacement dependent portion Ax, we have $V = V_0 + Ax$ and $\dot{V} = A\dot{x}$, assuming a constant cross-sectional area A. The pressure-mass flow rate relationship then becomes

$$\dot{P} = \frac{nRT}{V_0 + Ax}(\dot{m} - \rho A\dot{x}) \tag{2.3}$$

$$= \frac{n}{V_0 + Ax}(RT\dot{m} - PA\dot{x}) \tag{2.4}$$

2.1.4 The Pneumatic Line

Tubing or some enclosed rigid-wall feature usually forms the connection between pneumatic components. From [Andersen, 1967], for a circular tube of diameter D and length L, the flow is

termed a Poiseuille flow, and the relationship between mass flow rate $\dot{m}$ and pressure drop ΔP is:

$$\dot{m} = \rho_{avg} \frac{\pi D^4}{128\mu} \frac{\Delta P}{L}$$

where ρ_{avg} is the average density along the length of the tube and μ is the fluid viscosity.

This relationship is valid only under the assumption of laminar flow. The Reynolds number Re is a dimensionless number comparing inertial effects on a fluid to viscous effects:

$$Re = \frac{\rho v d}{\mu}$$

where ρ is the fluid density, v is the fluid velocity, d is a length characteristic of the problem, and μ is the fluid viscosity. Here, d is the tube diameter D; in terms of $\dot{m}$ above, the Reynolds number becomes:

$$Re = \frac{\rho v D}{\mu} = \frac{\rho A v D}{A\mu} = \frac{4\dot{m}}{\pi D \mu}$$

For a fluid to be considered laminar, its Reynolds number must be less than 2000.

With this restriction, for tubes of 0.1 m in length and 0.5 mm in diameter, pressure drops of up to 0.125 atm are accounted for. However, for tubes of the same length but 1.5 mm in diameter, as encountered in the laboratory, Poiseuille flow is only valid for pressure drops of 0.007 atm or so.

Fortunately, if the diameter of a pneumatic line is sufficiently large, such that the cross-sectional area of line is much greater than that of any orifice placed on that line, then the losses through the orifice dominate that of the line, and the pressure drop across the line may be neglected. In laboratory situations, supply tubing is typically of 3.2 mm in diameter or greater, with orifices of much smaller diameter. Consider a 0.5 mm diameter orifice connected via a 3.2 mm inner diameter pneumatic line to an air supply at 6 atm absolute. If the orifice discharges to atmospheric pressure, the mass flow rate through the orifice is $1.7 \cdot 10^{-4}$kg/s; this same mass flow rate must pass through the pneumatic line. If the line is 0.6 m in length, the line can handle that mass flow rate with a pressure drop of 0.001 atm, but the corresponding Reynolds number is 3700, and Poiseuille flow is not valid.

supply pressure	charging time	initial pressure	discharging time
2 atm abs	0.39 ms	2 atm abs	0.40 ms
3.5 atm abs	0.49 ms	3.5 atm	0.56 ms
6 atm abs	0.56 ms	6 atm	0.75 ms

Table 2.1: Charging and discharging times for a 12 mm^3 volume through a 0.5 mm diameter orifice with a contraction coefficient of 0.6. Charging times are from an initial pressure of 1 atm to the listed supply pressure, whereas discharging times are from the listed initial pressure to a 1 atm exhaust pressure. Times are determined by observing when the volume pressure reaches within 1% of the supply pressure for charging, and 1% of atmospheric pressure for discharging.

Realistically, most supply lines were less than 0.3 m in length and 1.5 mm in diameter. For supply pressures on the order of 2 to 4 atm gage, the pressure drops observed on the pneumatic lines were on the order of tenths of atmospheres, and considered negligible compared to the losses across the attached orifices.

2.1.5 Charging and Discharging Times for Orifice/Cylinder Combinations

A fully open valve may be modeled using the orifice equation, with a cross-sectional area equal to that of the open valve. Connecting this valve to a fixed-volume pneumatic cylinder then forms the simplest dynamic pneumatic circuit. The times required to charge a small 12 mm^3 volume through a 0.5 mm orifice from an initial pressure of 1 atm are obtained by numerical integration of Equations 2.1 and 2.2, and tabulated in Table 2.1. Because the volume is small, the process is adiabatic. Note that there is not much difference between charging and discharging times for small pressure differences, but the discharge time increases as the pressure difference increases.

The charging and discharging times for larger volumes can be extrapolated from the values given in Table 2.1, since the charging and discharging times are proportional to the volume of the cylinder.

2.2 Single Orifice Valve Designs

Most pneumatic valves have a single orifice whose cross-sectional area is varied to control the mass flow through the valve. This area variation is usually accomplished by actuating some movable element in the valve so that it opens up or closes off that orifice.

The force, stroke, and bandwidth required to shift that moving element are what determine the "goodness" of a valve design. Clearly, the lower the force, the lower the stroke, and the higher the bandwidth, the better the design, because actuators with lower power densities may be used.

To analyze this problem, consider the quasistatic forces on a single moving element varying the area of a single orifice. The motion of this moving element divides the space of all possible valves in two. If the movement is parallel to the flow through the orifice, the valve is a seating valve. If the movement is perpendicular to the flow through the orifice, the valve is a sliding valve.

Determining the forces on this moving element is a critical problem in valve design. The literature has many references to the forces on hydraulic valves, of which some representative references include [Johnston, 1991], [Hayashi, 1975], and [Smelnitskii, 1972]. However, the bulk of references to pneumatic valves concern sliding valves only, such as in [Louis, 1976] and [Nakada, 1980]. This is not surprising, considering that the flow regime is turbulent and compressible, and usually approached through finite element modeling.

2.2.1 Seating Valves

For a seating valve, the quasistatic forces arise from two different causes. When the valve is closed, the moving element, or the poppet, sits right on top of the orifice. As can be seen by examining Figure 2.2, the net force on the moving element results simply from the pressure difference across the moving element:

$$F = A\Delta P$$

In the case of a 5 atm pressure drop across a 0.5 mm orifice, the force on the poppet is 100 mN.

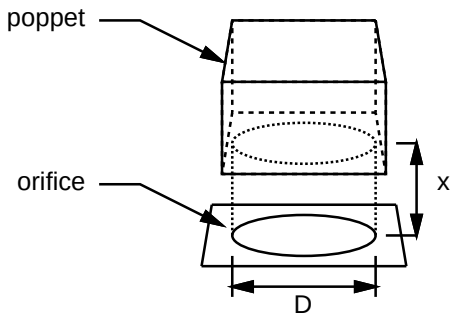

Figure 2.2: Illustrating the relevant dimensions for the poppet.

From the orifice equation, if the upstream and downstream pressures remain constant, the mass flow rate is solely a function of the cross-sectional area of the orifice. For a round orifice, as the valve is opened, the effective cross-sectional area A_{eff} is the sidewall of a cylinder whose base diameter is that of the orifice D and whose height is equal to the displacement x of the poppet away from the orifice, as shown in Figure 2.2:

$$A_{eff} = \pi D x$$

As a general rule of thumb, when the poppet has displaced one quarter of the orifice diameter or more, the cross-sectional area is then equal to that of the orifice. The poppet has moved far enough away that it no longer has an effect in obstructing the orifice and controlling the flow:

$$A_{eff} = \pi D \frac{D}{4} = \frac{\pi}{4} D^2 = A_{orifice}$$

When the valve is open, an upper bound on the force on the poppet can be determined from the momentum transfer from the air to the poppet, regardless of whether or not the pressures imposed across the valve tend to force it open or closed. Using the orifice equation, we can determine the mass flow rate, and the product of the mass flow rate and the change in velocity between the incoming air and the outgoing air is the force on the poppet:

$$F = \dot{m} \Delta v$$

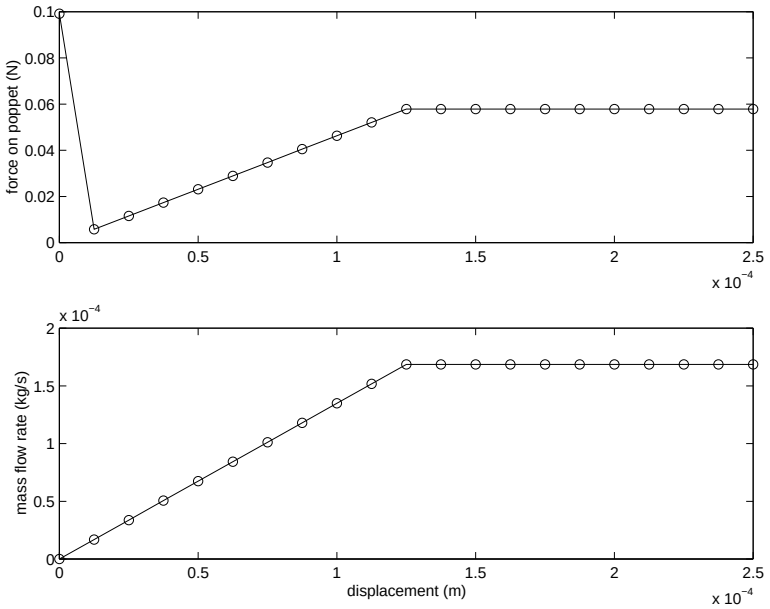

Figure 2.3: Modeled poppet force v. displacement for an orifice of diameter 0.5 mm, with an absolute upstream pressure of 6 atm and a downstream pressure of 1 atm.

An upper bound on this force can be determined by assuming all the flow momentum is translated into force on the poppet.

$$\begin{aligned} F &= \dot{m} v_2 \\ &= \frac{\dot{m}^2}{\rho_2 C_c A_0} \end{aligned}$$

As a sanity check, we know from impulse turbines that the force on a turbine blade can be determined from $\dot{m}\Delta v$. Assuming that the flow comes in perpendicular to the blade and goes out parallel to the blade, Δv is just the incoming air velocity, and the force is just $\dot{m}v$, as surmised above.

For a 0.5 mm diameter orifice with a contraction coefficient of 0.6, corresponding to that of a sharp-edged orifice, the force and mass flow rate are plotted as in Figure 2.3.

Figure 2.3 shows that the force falls as the orifice is opened, and then reaches a maximum as the poppet moves away from the orifice. However, the actual force would not drop as drastically at small displacements as indicated in Figure 2.3, mainly because with displacements on the order of $\frac{D}{16}$ or so, the pressure difference across the poppet, although no longer equal to the supply pressure

less the downstream pressure, would still be significant. In addition, for large displacements, the force on the poppet should fall to zero as the poppet moves farther away from the orifice. These issues are not reflected in the simplistic momentum transfer assumption.

To ground this discussion in some semblance of reality, consider check valves. These are largely seating type valves, with poppets mounted across orifices, as in [Wang, 1999]. When the valve is biased in the reverse direction, the flow through the valve is minimal. However, when the valve is biased in the forward direction, the pressure drop across the valve forces the poppet away from the seat, and if the suspension stiffness and poppet displacement are known, then the actual fluid force on the poppet can be found.

From [Wang, 1999], displacement as a function of pressure across the valve is given. However, a number of assumptions must be made before anything can be extracted from that data. First, no orifice size is given, so it was assumed that the orifice has a side s of 370 μm in length. This is justifiable, because the article mentions that this was one of the orifice sizes tested. Second, the exhaust pressure is assumed to be at atmospheric pressure. Finally, the suspension is assumed to be three cantilever beams with a length l of 80 μm, a width w of 80 μm, and a thickness t of 8 μm. From cantilever theory, the beam stiffness k_{beam} is $\frac{3EI}{l^3}$, where E is the Young's modulus of 2.8 GPa, and I is the moment of inertia of $\frac{t^3 w}{12}$. The suspension stiffness $k_{suspend}$ is then $3k_{beam}$, because there are three beams. The actual force F_{actual} is then $k_{suspend}x$, where x is the poppet displacement.

The calculated force F_{calc} can be estimated from the equation given above, using an effective area A_0 equal to $4sx$, where s is orifice side length, and x is poppet displacement. Because this is a square orifice, $4sx$ is just the sidewall area. Note that the fluid used in [Wang, 1999] is nitrogen, but that fluid has the same k as air, with a gas constant of 297 J/kgK.

For the purposes of comparison, we can also look at the force on the poppet F_0 at zero displacement, which is just $A\Delta P$.

For an upstream pressure of 20 kPa gage, the displacement is 50 μm. The calculated force

F_{calc} is 1.1 mN, the zero displacement force F_0 is 2.7 mN, and the actual force F_{act} is 8.4 mN.

For an upstream pressure of 70 kPa gage, the displacement is 80 μm. The calculated force F_{calc} is 5.7 mN, the zero displacement force F_0 is 9.6 mN, and the actual force F_{act} is 13.4 mN.

Apparently, our supposed upper bound is a failure. However, the assumptions are probably suspect— for instance, if the beam thickness is reduced by 2 μm, the "actual force" drops by 2.4, which is enough to get the calculated force within a factor of 3 with the actual force in the 20 kPa gage case, and have them equal in the 70 kPa case. Most likely, the beam dimensions and orifice size are incorrect; after all, they were not necessary, considering that the data was intended for a different purpose— to show that an alternate suspension had a greater displacement, and was therefore a better choice for check valves.

Clearly, more work needs to be done in determining these forces, and a search of the literature reveals no papers that address these concerns for pneumatic seating valves, although absence of evidence is not evidence of absence. Though both incompressible flow and low speed compressible flow situations are more easily computed, this case is more difficult, with its high velocity, turbulent compressible flow, and usually tackled by finite element analysis. To check those theoretical results, a useful experiment to run would be the fabrication of a number of orifices with cantilevers across the orifices. The deflections of those cantilevers, combined with their stiffnesses, would provide a measure of the actual poppet forces.

Still, as a back-of-the-envelope estimate, nothing could be simpler than $A\Delta P$. It is this author's contention that poppet valve actuators are oversized in force anyway by a factor of 2 or more, so as to generate enough force to push the poppet into some compliant seating material and consequently reduce leak rates.

2.2.2 Sliding Valves

In a sliding valve, the moving element, or slider, moves perpendicular to the direction of flow. When the flow is fully developed, it forms a jet of air at the mouth of the orifice. This jet

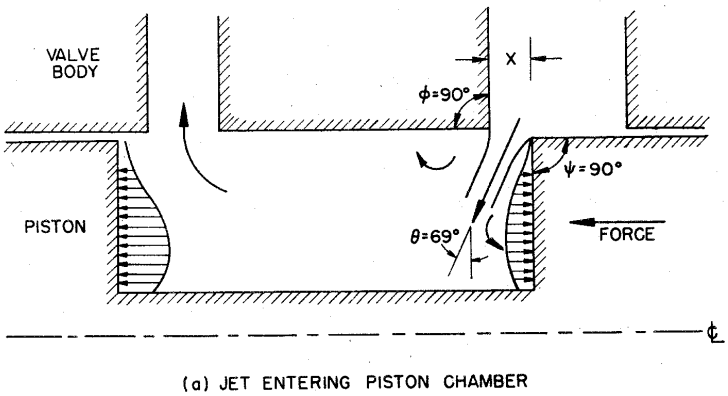

Figure 2.4: As air passes through an orifice, it forms a jet at an angle of 69°, and exerts a force on the valve's moving element, tending to close the orifice. Here, the moving element is denoted as the piston. This figure is taken directly from [Blackburn, 1960].

force may be estimated from momentum transfer, as for seating valves. However, because of the geometry of the sliding valve, there is an additional factor to take into account.

For displacements much greater than the clearance between the orifice and the slider, the resulting jet forms an angle of 69° as indicated in Figures 2.4 and 2.5 [Blackburn, 1960]. Also, regardless of whether the fluid is flowing into or out of the notch in the rotor, the fluid exerts a force on the slider that causes the orifice to close. Note that the figures above indicate a slider that fully reverses the flow back into the valve body. A sliding valve need not do that though; it may just be a simple block that is constrained to move perpendicular to the flow, as indicated in Figure 2.6. With the slider completely blocking the orifice, all the force on the slider is parallel to the flow. With the slider partially blocking the orifice, the fluid exerts a force that causes the orifice to open.

In either configuration, assuming that the slider is suspended so that its motion parallel to the flow can be neglected, the only component of the fluid force on the slider is that perpendicular to the flow. When the valve is closed, this perpendicular component is zero. When the valve is open and its displacement is greater than the clearance between the orifice and the slider, the jet force is reduced by a factor of $\cos 69°$.

Once again, from the orifice equation, if the upstream and downstream pressures remain

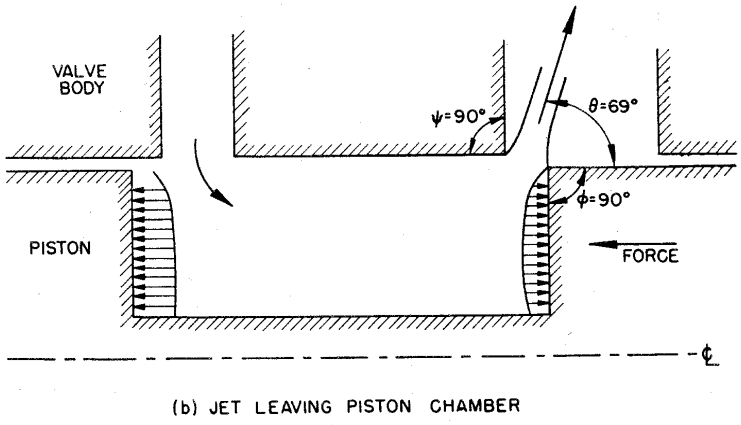

Figure 2.5: In this case, the air flows out from the moving element and into the stator. However, it still exerts a force on the valve's moving element that tends to close the orifice. This figure is also taken directly from [Blackburn, 1960].

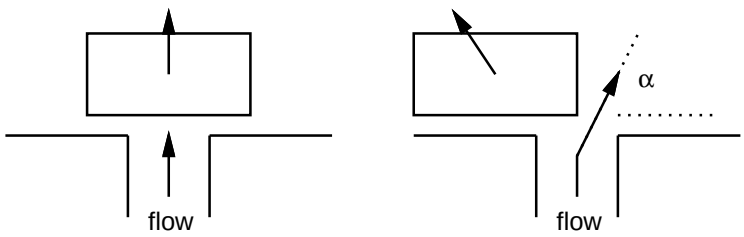

Figure 2.6: A simple slider blocking an orifice (left). With the valve partially open (right), the jet force on the slider causes the slider to stop blocking the orifice.

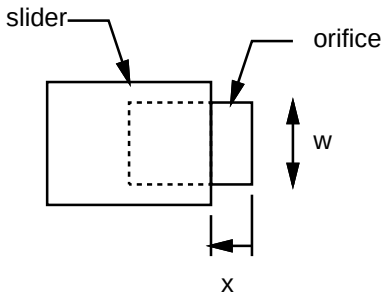

Figure 2.7: Illustrating the relevant dimensions for the slider from a top view.

constant, the mass flow rate is solely a function of the cross-sectional area of the orifice. For a sliding valve with a square orifice, the effective area of the orifice is:

$$A_{eff} = \begin{cases} wx & \text{if } x < x_{max} \\ wx_{max} & \text{if } x > x_{max} \end{cases}$$

where w is the orifice width, and x is the slider displacement, as illustrated in Figure 2.7.

Following arguments similar to those of the previous section, with the addition of the factor of $\cos 69°$, the perpendicular force on the slider is given by:

$$\begin{aligned} F &= \dot{m} v_2 \cos 69° \\ &= \frac{\dot{m}^2}{\rho_2 C_c A_0} \cos 69° \end{aligned}$$

For a square orifice with an area equivalent to that of a 0.5 mm diameter round orifice with a contraction coefficient of 0.6, the force and mass flow rate are plotted as in Figure 2.8.

Thus, for sliding valves, the maximum force an actuator must produce is approximately one third of that for a seating valve. On the other hand, the displacement is increased by a factor of four, because the entire slider must clear the orifice for full flow. The assumption that there is negligible motion parallel to the flow may also be difficult to implement, since any parallel movement should be sufficiently small to maintain the clearance seal between the orifice and the slider, and consequently prevent jamming. Balancing the pressures on the slider so that they cancel each other out, and employing stiff bearings would be possible approaches to successful implementation.

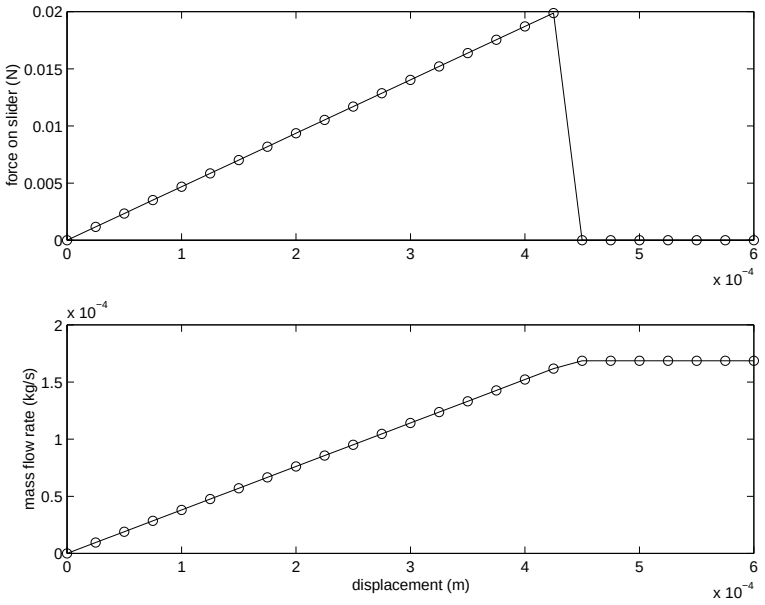

Figure 2.8: Modeled slider force v. displacement for a square orifice with area equivalent to a round one of diameter 0.5 mm, with an absolute upstream pressure of 6 atm and a downstream pressure of 1 atm.

Therefore, sliding valves in their simplest embodiment appear to be more difficult to construct and apparently have fewer advantages compared to seating valves. However, successful sliding valves have been made, most notably spool valves in servocontrol applications.

Readers with some familiarity with spool valves may recall that these examples of sliding valves do not require suspensions. They typically use some liquid for lubrication; this liquid provides a self-centering bearing. Simply relying on the air itself to provide such a bearing is a much more difficult problem, and may be hard to stabilize because of the compressibility of the air, as compared with the incompressibility of a liquid.

In Sections 2.3 and 2.4, refinements are presented that increase the appeal of sliding valves.

2.2.3 Pressure Balancing

Both seating and sliding valves require high forces. By clever arrangement of the valve inlets and outlets, it is possible to trade lower peak actuator forces for higher complexity in valve

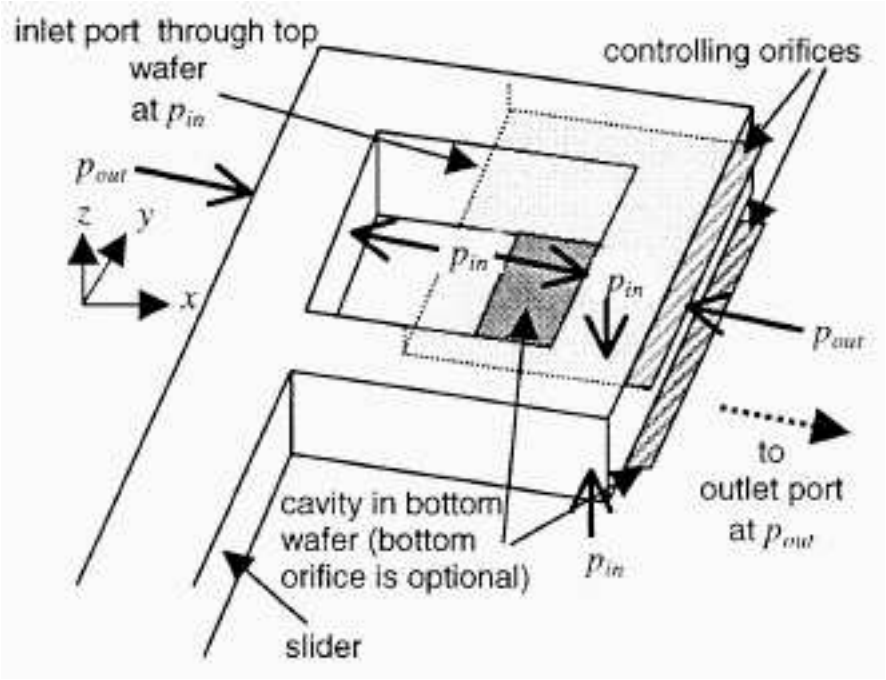

Figure 2.9: Illustrating the force balancing for the Lucas Novasensor valve [Lucas Novasensor].

construction. This arrangement is referred to as *pressure balancing*.

In general, it is more straightforward to pressure balance a sliding valve than a seating valve, because the sliding valve moves perpendicular to the flow. Spool valves, sometimes balanced to lower the actuator forces required, are commonly available in 10 cm or larger sizes, as second stages for power amplification purposes.

On the millimeter scale, one of the most promising valve designs appears to be the balanced design of Lucas Novasensor[Lucas Novasensor], soon to be available commercially. As shown in Figure 2.9, the Lucas valve is a sliding valve. Further discussion of the actuation of this valve is given in Section 2.3.

Statically, it is obvious when a design is balanced so that the forces on the moving element have been reduced in magnitude. However, it is not so obvious that the design remains balanced dynamically; as flows increase, pressures may drop on the side upon which the flow occurs while pressures on sides with little flow remain relatively constant, so that the statically balanced design

is no longer balanced dynamically.

2.2.4 Sealing

Depending on the use of valve, good sealing may or may not be an issue. In process control applications, where a precise concentration of reagents is desired, having a valve that leaks appreciably when it is supposed to be closed is not optimal. On the other hand, in positioning applications, a small leak that does not move a driven pneumatic cylinder much is probably acceptable.

Seating valves seal well with a surplus of force, but compliant materials are also needed to form good seals if leaks are unwanted. However, if the seal is too compliant, there is the potential for the valve to jam up completely with the poppet stuck to the seat.

Seating valves also tolerate dirt well, as long as the poppet moves away from the seat far enough so that the dirt can travel through the orifice and be flushed out of the valve.

Sliding valves require tight clearances, because they depend on those clearances being as tight as possible. By their nature, these valves leak. Also, tight clearances require stiff suspensions to prevent the slider from being driven into the body and jamming, although appropriate pressure balancing would reduce that tendency.

In addition, sliding valves do not tolerate dirt as well as seating valves. Particles are caught in the clearance seal can abrade both the slider and valve body and result in a larger clearance and greater leak.

2.3 Valve Actuation

Consulting Figures 2.3 and 2.8, it appears that large forces are needed in order to drive the moving element of a valve. However, these large forces exist only for unbalanced valve designs. With proper force balancing, these forces may be reduced to manageable magnitudes.

The current best practice in valve design appears to be the balanced design of Lucas

Novasensor [Lucas Novasensor], as discussed in Subsection 2.2.3. The Lucas valve is a sliding valve, the slider being the easier of the two valve types to balance statically. In the valve, a silicon lever is pivoted in front of a square orifice. This lever is actuated by a series of ribs through which current is passed, generating a high force with low displacement. The displacement is amplified by the lever, resulting in motion of the lever to block or unblock the orifice.

From the dimensions and values provided in the paper, enough current passing through ten pairs of ribs to generate a 100 K temperature rise results in a blocked force of 1.5 N and a free displacement of 7.5 μm. The tip of the lever is also claimed to move more than 100 μm. From these numbers, it is reasonable to believe that the thermal actuator generates a force of 750 mN with a displacement of 3.75 μm; at the tip of the lever where the orifice is, the displacement is 100 μm, and the associated force is then (3.75/100)750 mN, or 28 mN. Unfortunately, the lever is not pivoted about a frictionless pin joint, but by another short cantilever beam, whose dimensions and stiffness are not provided. So it is unclear what percentage of the 28 mN available goes towards bending the pivot beam, and what proportion actual goes towards actuating the valve mechanism itself.

Other portions of the paper indicate that 1.2 W of power are actually provided to the thermal actuator to generate this theoretical force. It is also unclear what mechanical power is really required, since thermal actuators are not exactly the desired choice for low power actuators.

From mail correspondence with Kirt Williams at Lucas Novasensor, it is clear that certain data is being withheld for proprietary purposes. It is speculated that the company will probably replace the thermal actuator with one of higher speed, and then target the valve towards a different market.

For valves without force balancing, following the development of Subsection 2.2.1, for an orifice of 0.5 mm diameter and a pressure difference of 5 atm, a worst-case force of 100 mN needs to be generated over a stroke of 0.125 mm to actuate the poppet of a seating valve. At an actuation rate of 100 Hz, this works out to a mechanical power of 1.25 mW.

Following the development of Subsection 2.2.2, for an orifice of 0.5 mm diameter and a

pressure difference of 5 atm, a worst-case force of 20 mN needs to be generated over a stroke of 0.425 mm to actuate the slider of a sliding valve. At an actuation rate of 100 Hz, this works out to a mechanical power of 0.85 mW.

With the required power on the order of 1 mW, we note that the efficiency of small actuators is generally poor [Trimmer, 1989], especially at the low speeds necessary for valve actuation. To generate that 1 mW of mechanical power, we may need a surfeit of electrical input power. This then suggests a potential pathway to valve miniaturization— by minimizing the electrical power consumed by a particular valve design, we can then minimize the size of that valve design.

2.4 Multiple Orifice Valve Designs

In a straightforward comparison of multiple orifice designs against single orifice designs, multiple orifice designs apparently have no great benefit.

Consider a valve with a single orifice of area A, and compare it to a valve with ten orifices of area $\frac{A}{10}$, as in Figure When the valve is closed, there is no change in the force required to hold the valve in that position. If the valve is a seating valve, the cross-sectional area is still the same; if the valve is a sliding valve, the force perpendicular to the flow is zero. When the valve is open, $\dot{m}$ is the same for both the single orifice and multiple orifice designs, if the upstream and downstream pressures are the same. The fluid velocity v_{fluid} also is not changed. So there is no change in the force required.

However, displacement is another story. The maximum displacement required for a single orifice seating valve is $\frac{D}{4}$, where D is the diameter of that orifice; for a single orifice sliding valve, the maximum displacement is D. For the multiple orifice seating valve, that maximum displacement becomes $\frac{D}{4\sqrt{10}}$, and for the multiple orifice sliding valve that displacement is $\frac{D}{\sqrt{10}}$. In general, the displacement for n orifices is reduced by a factor of $\sqrt{n}$.

There are other tradeoffs as well. The volume required for the overall valve is obviously

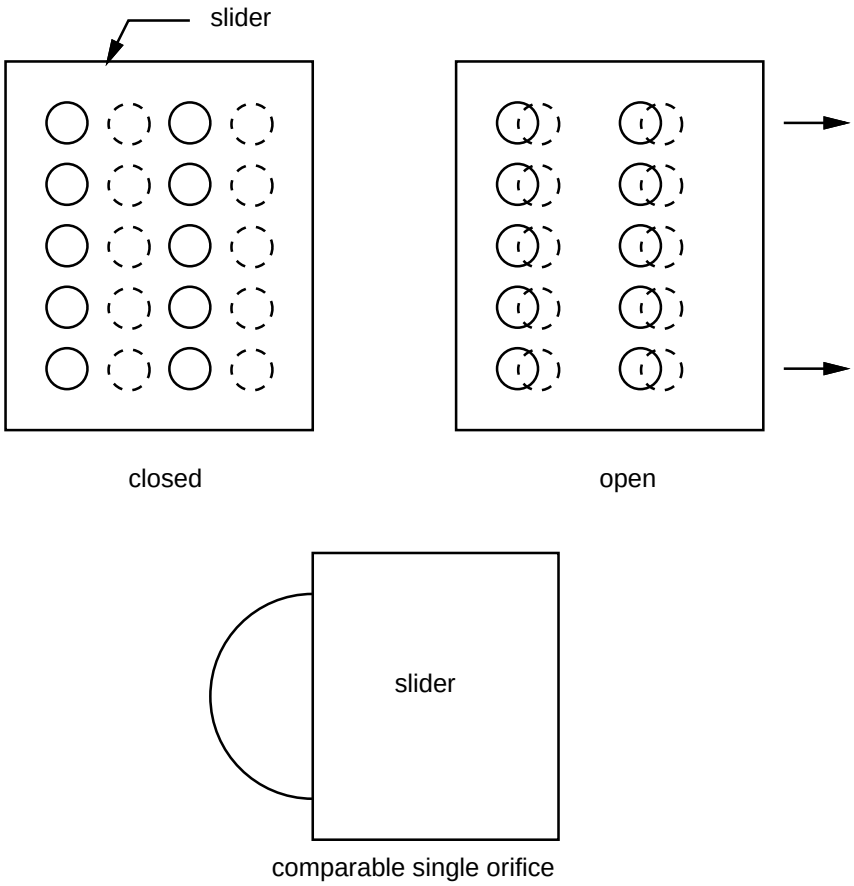

Figure 2.10: Multiple orifice valve design, showing open and closed positions, along with comparable single orifice design.

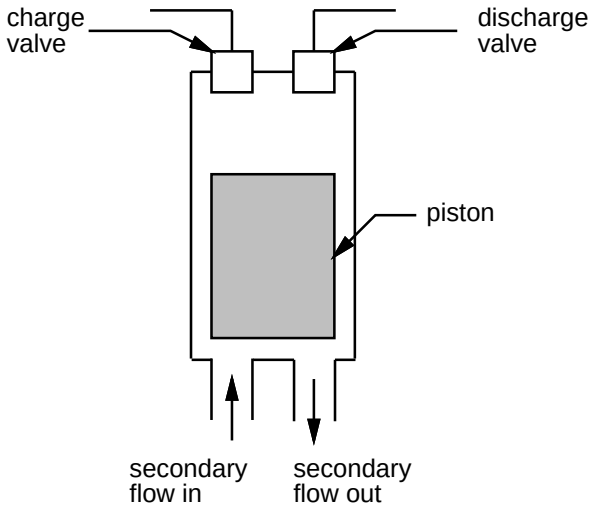

Figure 2.11: Multistage valve design.

higher, because of the additional spatial overhead necessary to separate the individual orifices. Also, orifices with smaller cross-sectional areas have more stringent filtration requirements.

2.5 Multistage Valve Designs

Multistage designs [Wang, 2000] sacrifice bandwidth and volume for lower forces and displacements in the primary actuator. In these designs, two small pilot valves are used to charge and discharge a variable-volume cylinder, which in turn drives a pneumatically-actuated valve, as shown in Figure 2.11. Alternatively, a single pilot valve and a discharge orifice may be used instead, with some loss of flexibility in utilizing the resulting multistage valve design. Actuation time is increased, because of the additional time required to charge the cylinder which drives the second stage, and overall valve size is increased, because of the additional volume of the primary pilot valve and variable-volume cylinder.

To determine the effectiveness of such a design, consider a single orifice poppet valve with an orifice of diameter D, and assume that the valve can be actuated in time T, and that T is on the order of milliseconds. Now, compare this to a two-stage design, with a pneumatically-actuated

valve having the same diameter orifice, that can also be actuated in time T. Assume that this secondary stage is a piston in a cylinder, and the piston needs to be moved a minimal distance so that the diameter D orifice can be uncovered; this is accomplished by charging up the variable-volume cylinder from atmospheric pressure to supply pressure, creating a pressure difference that will move the piston. This secondary stage is driven by two smaller primary poppet valves, with an orifice of one tenth the cross-sectional area of the secondary valve; the corresponding diameter is then $\frac{D}{\sqrt{10}}$. Because the secondary is a seating valve, the minimal displacement required is $\frac{D}{4}$. The variable volume is of diameter D, with maximum height $\frac{D}{4}$.

If D is 0.5 mm, and the piston is made of silicon, with a 1.0 mm diameter and a 1 mm thickness, we can apply $F = ma$ to determine the piston position, along with Equations 2.1 and 2.4, and then numerically integrate the system of equations. If the primary charging poppet charges the variable volume cylinder from an initial pressure of 1 atm absolute to 6 atm absolute, the resulting time it takes to move the piston 0.125 mm and open up the second stage poppet is 35 μs. If the primary discharging poppet discharges the variable volume cylinder from an initial pressure of 6 atm absolute to 1 atm absolute, the resulting time it takes to move the piston back 0.125 mm and close up the second stage poppet is the same 35 μs; the limiting factor is the mass of the piston. Therefore, the overall actuation time is increased by this amount. However, it is negligible, because the valve actuation time T is usually on the order of milliseconds, so the bandwidth does not change appreciably.

The maximum force required can be estimated by using $A\Delta P$. Because the area is reduced by a factor of ten for the primary valve of the two stage design, but ΔP is the same, an order of magnitude less force is necessary, while the displacement required is $\frac{D}{4\sqrt{10}}$.

For a two stage design with a primary valve whose cross-sectional area is n times smaller than that of the pneumatically-driven secondary, the overall energy required to actuate the primary is $n\sqrt{n}$ times less than a single stage design. However, the complete design is more complicated than that of a single stage, and two primary valves are required to charge and discharge variable volume

cylinder. Because the cross-sectional areas of the primary valves are smaller, filtering requirements also need to be tightened, and good seals also need to be provided in three places, instead of just one. There is also the crucial issue that a primary valve still needs to be designed, although its force and stroke requirements are admittedly relaxed.

In [Wang, 2000], one particular implementation of the multistage concept has been fabricated, with the particular fluid dynamics of the pneumatically-driven secondary analyzed in [Yang, 2000]. Unfortunately, not much data has been provided to buttress the theoretical conclusion given above.

2.6 Self-Driven Designs

In typical MEMS applications, actuation is accomplished directly by converting electrical input power to useful mechanical power. Direct valve actuation is simpler, but many tasks require higher forces and strokes. On the other hand, using a set of primary and secondary actuators trades simplicity and bandwidth for lower forces and strokes in the primary actuator. Moreover, if there is power available from other non-electrical sources and bandwidth to spare, the secondary actuator can be driven with the alternative power source, providing power gain for the electrically-driven primary actuator.

As argued above, indirect drive is preferable to direct drive, and there is already an alternate source of power available in the valve— the compressed air itself. A piloted servovalve is usual practice in such situations; the output of a small primary valve is amplified by the larger secondary servovalve. Unfortunately, we still need an actuator for the pilot valve, although the force and stroke are reduced.

However, we can also:

- use the available fluid power to drive the secondary actuator.
- and employ the input electrical power to drive a primary actuator that brakes the secondary

actuator.

This is analogous to stopping a piece of machinery by throwing a wrench into the spinning gears of the machine, although we would wish to have a rather more repeatable braking action.

The effectiveness of such a brake may be quantitatively measured by comparing the power gain of a directly driven valve with that of a fluid-actuated valve with a brake. In the next two chapters, we present two implementations of such a brake, and provide evidence for the validity of the brake idea presented above.

Chapter 3

Turbine Brake Valve (TBV)

Following the terminology of the previous chapter, we propose a rotary valve, with a pneumatically driven turbine as the secondary actuator and an electrically driven brake as the primary actuator. Central to the design is the rotary control valve, composed of a rotor and stator. The orientation of this rotor with respect to its matched stator determines the flow through the valve.

The turbine continually drives the control rotor, whereas the brake opposes the motion of the control rotor and acts to slow and stop it. By appropriately modulating the brake to determine the orientation of the control rotor, the pressure of the load volume may be varied.

In this chapter, the theoretical design of such a turbine brake valve will be presented, followed by experimental results on large-scale prototypes of each section. In addition, future work concerning the reduction of this valve to milliscale dimensions will be discussed.

3.1 Theoretical Design

The valve is composed of three sections: a control section, a drive section, and a brake section, as illustrated in Figure 3.1.

All three sections are integrated by stacking the stators and mounting the rotors on a

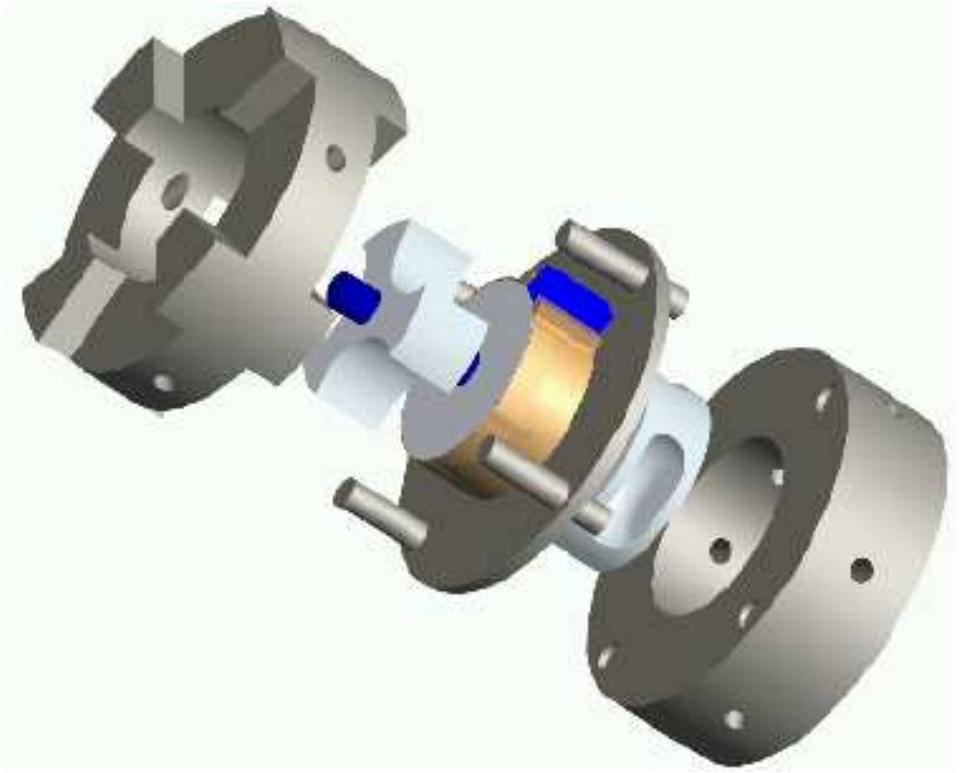

Figure 3.1: The TBV exploded, with its three sections. The drive section, with its fluid jet stator and three bladed rotor appears at the top. The brake section is in the center, with its rotor surrounded by a band brake. The control section appears at the bottom, with its stator and three bucket rotor.

common shaft. Writing the torque balance for the entire valve gives:

$$J\ddot{\theta} = \tau_{drive} - \tau_{control} - \tau_{brake} - \tau_{damping}$$

The control rotor is driven by the air emanating from the drive stator ports and impinging upon the blades of the drive rotor. The drive stator ports are angled so that the air flow tends to turn the drive rotor. The brake section is used to slow and stop the motion of the brake rotor, and consequently, all three rotors. When the brake is disengaged, the rotors are free to spin; with the brake engaged, the rotors can be stopped at any angle, and thereby change the load pressure.

In the next three subsections, the theory behind each of the three sections is discussed. Finally, the operation of a complete valve with the three sections integrated together is presented.

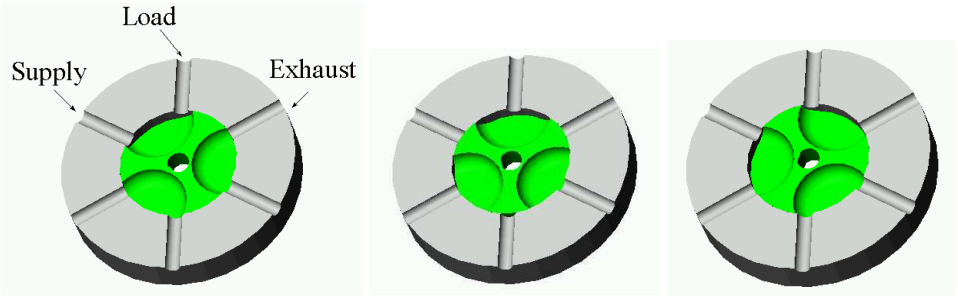

Figure 3.2: The control section of the TBV is comprised of a stator centered around a smaller rotor. The position of the rotor in the control section determines the pressure at the load. The load is charged from the supply (left), the load pressure is held approximately constant (middle), and the load is discharged into the exhaust (right).

3.1.1 Control Section, Theoretical Considerations

The control section is composed of two parts– a stator and a rotor. The stator has three ports, the first of which is connected to the air supply, the second to the load, and the third to the exhaust. The rotor has three notches, each of which can connect two adjacent ports together. The orientation of the rotor determines whether the load is charged upwards towards the supply pressure, held at a constant pressure, or discharged to atmospheric pressure, as shown in Figure 3.2. By changing the orientation of the control rotor, the load pressure can be modulated and controlled.

An orifice effectively exists between the edge of the rotor and the stator as the rotor obstructs the fluid ports of the stator. The mass flow rate $\dot{m}$ through this orifice is given by the orifice equation of Subsection 2.1.1.

The fluid also exerts a torque on the rotor as it passes through the control section. An upper bound on this torque is:

$$\tau_{control} = \dot{m} v_{fluid} r \cos\theta \tag{3.1}$$

where $\dot{m}$ is the mass flow rate from the orifice equation above, v_{fluid} is the fluid velocity, which can be estimated from the mass flow rate, the orifice cross-sectional area, and the fluid density, r is the radius of the rotor, and θ is the jet angle. This is an upper bound, because it assumes that all the momentum of the air is converted into torque.

When the flow is fully developed, it forms a jet of air at the mouth of the orifice. For rotor displacements much greater than the clearance between the rotor and the stator, the jet forms an angle of 69° as indicated in Figures 2.4 and 2.5. Also, regardless of whether the fluid is flowing into or out of the notch in the rotor, the fluid exerts a force on the rotor that causes the orifice to close.

Note that the fabrication of such a control section requires tight tolerances between the rotor and stator, because of the clearance seal that exists between the two. If the tolerances were too loose, it would be difficult to hold the load pressure constant, as in the center illustration of Figure 3.2. On the other hand, if the valve is operated in a purely binary fashion, continually charging or discharging the load, this is less of an issue, because a large leak in the clearance seal would simply reduce the maximum pressure that the load could reach, while reducing the discharge time. However, an appreciable leak may not be acceptable in the first place.

3.1.2 Drive Section, Theoretical Considerations

The drive section is simply an impulse turbine, with its own rotor and a stator, as illustrated in Figure 3.3. The stator has four supply ports, each with air at the supply pressure; the rotor has three blades. The section is arranged so that at least one air jet hits the rotor at all times, so that a torque can be exerted to drive the control section. An upper bound on the drive torque is:

$$\tau_{drive} = k_{jet,avg} \dot{m} v_{fluid} r \tag{3.2}$$

where $k_{jet,avg}$ is the average number of jets impinging on the rotor blades, $\dot{m}$ is the mass flow rate from the orifice equation above, v_{fluid} is the air velocity, and r is the radius of the rotor. This is also an upper bound, because of the assumption that all the momentum of the air is transferred to the drive rotor.

From geometrical considerations, there are approximately 1.5 jets impinging on the drive rotor, so $k_{jet} = 1.5$ on average. Although this is an estimate, its impact on the drive torque is much less of a factor than the momentum assumption mentioned above.

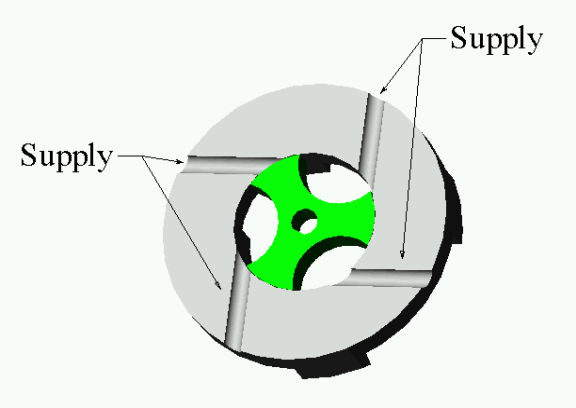

Figure 3.3: The drive section is an impulse turbine. Air impinges on the drive rotor from four supply ports, arranged such that at least one air jet fully hits the rotor at any given position. The exhaust is both in and out of the plane of the paper.

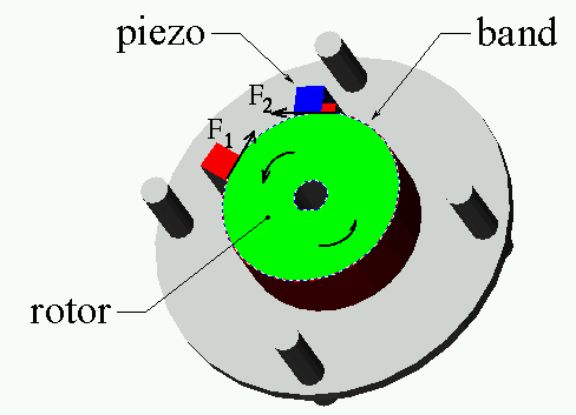

Figure 3.4: The brake section is a simple band brake. Currently, the band brake is actuated by a voice coil actuator, but a piezoelectric actuator could also be used. Note that the band is pulled in the direction of rotation. This reduces the force required to actuate the brake.

3.1.3 Brake Section, Theoretical Considerations

The brake section is needed to oppose the drive torque and stop the control rotor at the desired angular position, in order to control the pressure at the load. Its current implementation is as a band brake, as illustrated in Figure 3.4. The force on the two ends of the band F_1 and F_2 are related by[Orthwein, 1986]:

$$F_1 = F_2 e^{\mu\alpha}$$

where μ is the coefficient of friction, and α is the wrap angle in radians of the band about the brake rotor. The torque exerted by the brake section is then:

$$\tau_{brake} = (F_1 - F_2)r$$

where r is the radius of the rotor. Note that one of the forces on the band is much greater than the other. If the band is fixed to the stator on the side opposing the rotation of the rotor, the actuator for the brake section can exert a much lower force. For a wrap angle of 270° and a coefficient of friction of 0.2, this is a factor of 2.6.

Of course, there is no free lunch; the band wears away at a higher rate towards the fixed end, and the surface of the rotor also wears, but uniformly.

Currently, the band brake is pulled tight by a voice coil actuator. However, the brake could be any actuator acting on the brake rotor in a wearing or nonwearing fashion, and used to generate braking torque. Other braking methods could include:

- any actuator pulling on one end of a band brake.
- any actuator forcing a high-friction brake shoe into the rotor.
- an electrostatic actuator acting in the same fashion as an electrostatic motor.
- an eddy-current brake.
- a brake rotor immersed in an electrorheological or ferromagnetic fluid.

3.1.4 Integrated Valve, Theoretical Considerations

The easiest way to consider the operation of the integrated TBV is in a bang-bang, minimum time control fashion, using pulse width modulation to control the average load pressure, as touched upon in Subsection 1.2.1. Since the control section has three similar buckets, the control rotor needs only to rotate through $\frac{2\pi}{3}$rad before we return effectively to the same angular position. Because the drive section only turns the rotor assembly in one direction, once a position has been passed, we need to wait another $\frac{2\pi}{3}$rad before that same position is reached again.

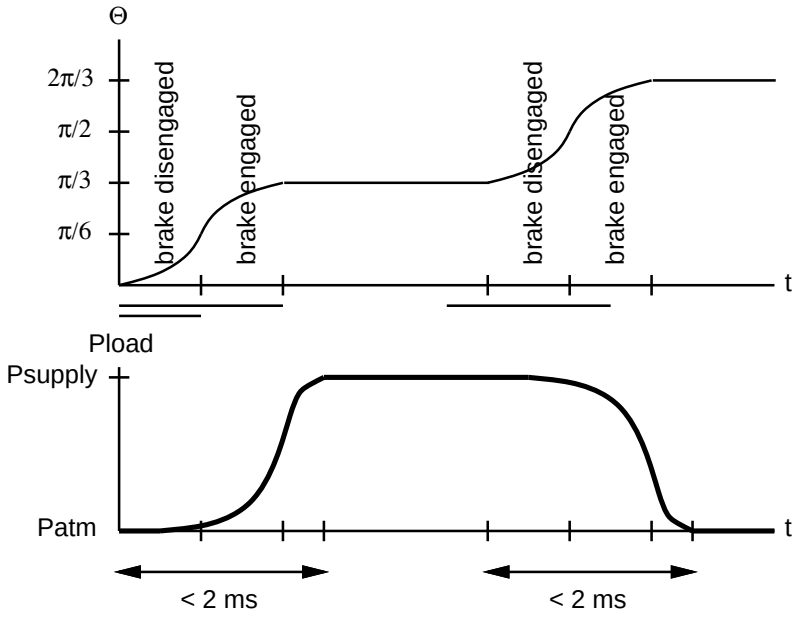

Figure 3.5: Illustrating the operation of the TBV. To raise the load pressure, the brake is released and then reengaged to stop the control rotor in such a position that the supply can charge the load. To lower the load pressure, the brake is released again and then reengaged to stop the control rotor so that the load can discharge through the exhaust.

Suppose we wish to increase the average load pressure. Figure 3.5 indicates how such an operation takes place with the TBV. Initially, assume the load pressure is at atmospheric pressure, with the angular position θ at 0 and the control rotor connecting the load port to the exhaust port, as at the right of Figure 3.2. The brake is released, and the drive section accelerates the rotor assembly. As the assembly reaches $\theta = \frac{\pi}{6}$rad, the brake is engaged, and decelerates the rotor against the torque from the drive section, finally stopping it at $\theta = \frac{\pi}{3}$, with the control rotor now connecting the supply port to the load port, as at the left of Figure 3.2. The load pressure begins to rise, and finally reaches supply pressure after the charging time of the load cell is reached. Following the specifications of Section 1.2, this entire process of brake release, brake reengagement, and load charging must occur in less than 2 ms.

The control rotor is held charging the load until the average load pressure is close to its desired value. Then the brake is disengaged again, and the drive section accelerates the rotor assembly through $\theta = \frac{\pi}{2}$, whereupon the brake is engaged, stopping the assembly at $\theta = \frac{2\pi}{3}$. With

the control rotor now connecting the load port to the exhaust port again, the load pressure falls to atmospheric pressure. Once again, this entire process of brake release, brake reengagement, and load charging must occur in less than 2 ms. The process then repeats.

The average load pressure is controlled by the length of time that the rotor assembly is at $\theta = \frac{\pi}{3}$. By varying this time, the average load pressure can be controlled to any value between 20% and 80% of the difference between the supply pressure and atmospheric pressure, subject to leaking.

Also, by keeping the rotor at $\theta = 0$ or $\theta = \frac{\pi}{3}$, the average load pressure can be made equal to atmospheric or supply pressure respectively.

Since the angular displacement θ is related to the rotor inertia J and the torque τ by $\ddot{\theta} = \frac{\tau}{J}$, the relationship between the displacement θ and the time Δt required to move that displacement is:

$$\theta = \frac{1}{2}\frac{\tau}{J}(\Delta t)^2 \tag{3.3}$$

To estimate the turn-on and turn-off times, we need to determine an upper bound on the time Δt. This occurs when torque is at a minimum, and the worst case torque is $\tau_{drive} - \tau_{control}$, when the drive section must spin the rotor assembly to counter the maximum control torque. If the acceleration time is to be equal to the deceleration time, the total turn-on time is then $2\Delta t$.

3.2 Large-Scale Prototype, Experimental Results

As a proof of concept for the secondary drive and primary braking idea, a 5:1 scale prototype of the TBV was fabricated. The choice of a larger size permitted the use of traditional machining techniques and made apparatus construction and testing more tolerable. A nominal rotor diameter of 12.7 mm was selected, to make tooling considerations easier. For testing purposes, a Maxon motor with shaft encoder was attached to each of the three sections in turn, so that static tests could be performed, as shown in Figure 3.6. The rotor of each section was mounted on bearings and centered to ensure that the rotor spun freely. The shaft of each section was then connected to the motor shaft by a shaft coupler. To determine angular position, a shaft encoder with a resolution of 2000

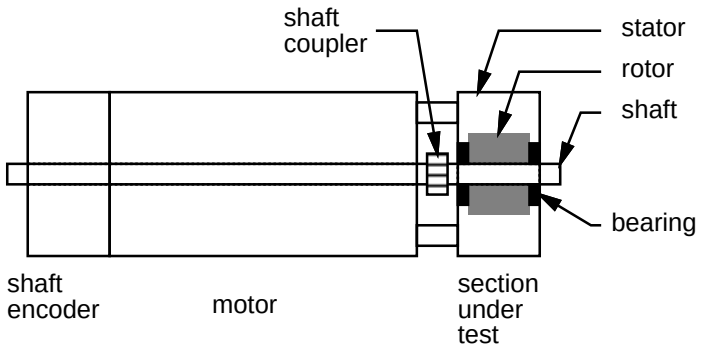

Figure 3.6: Illustrating the testing of each of the three individual TBV sections.

counts per revolution was attached to the backshaft of the motor.

Before testing could proceed, the motor was characterized to determine the relationship between the motor input current and the output torque. By hanging standard weights off the shaft and determining the input current i required to start the shaft turning, the output torque τ was determined to be:

$$\tau = Ki + K_0$$

where $K = 36$ mNm/A and $K_0 = -0.52$ mNm, as shown in Figure 3.7. The offset K_0 is due to Coulomb friction in the motor, which must be overcome in order to move the rotor of the motor. Because the tests conducted require the motor to be moved to some position and then generate enough torque to counter an opposing torque, the holding torques consequently recorded will be off from the actual holding torques by $\pm|K_0|$.

3.2.1 Control Section, Experimental Results

The first section to be tested was the control section, mainly because if the clearance seal between the rotor and stator were ineffective, the entire point of the valve would be moot without a means of governing the load pressure. After mounting the control section in its stator, the entire assembly was attached to the motor characterized in the previous section, as in Figure 3.6. Next,

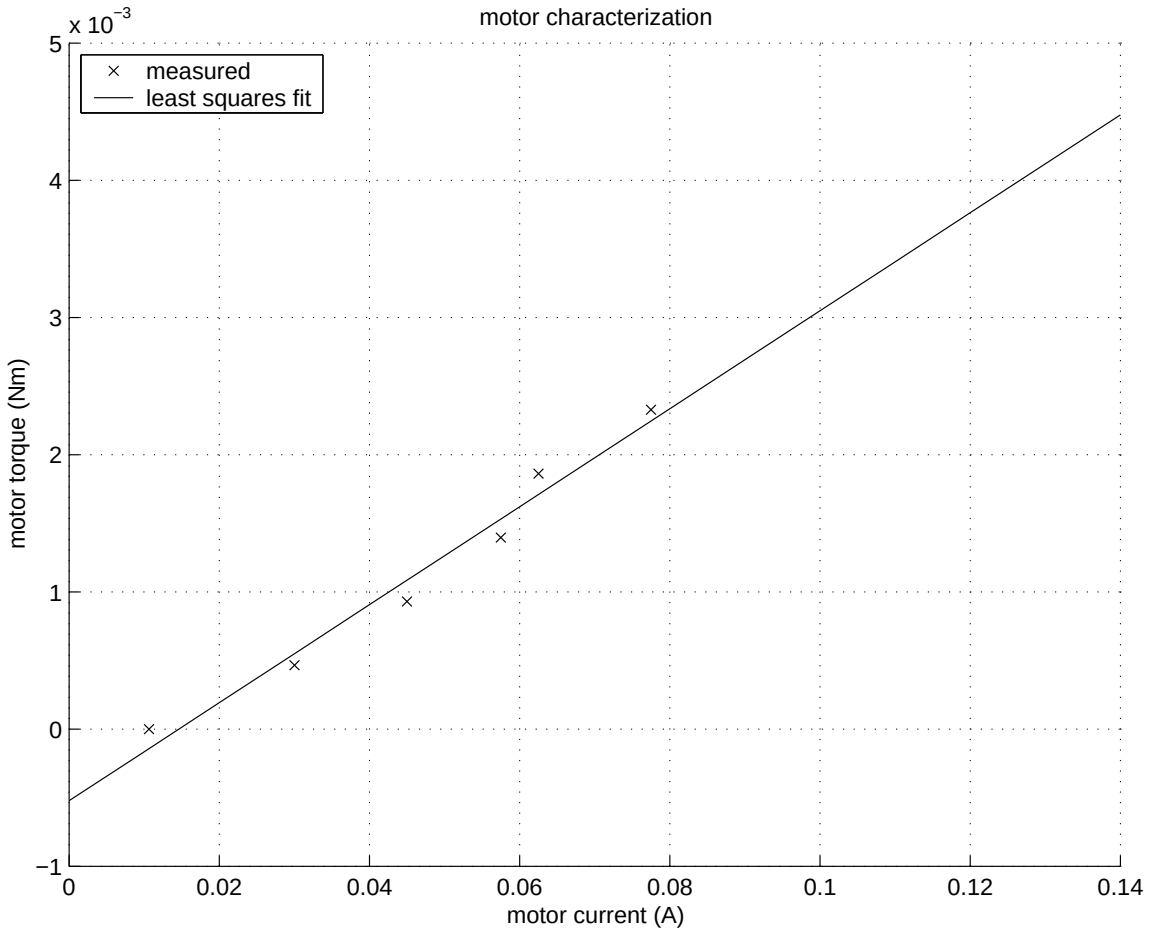

Figure 3.7: Motor torque v. motor current.

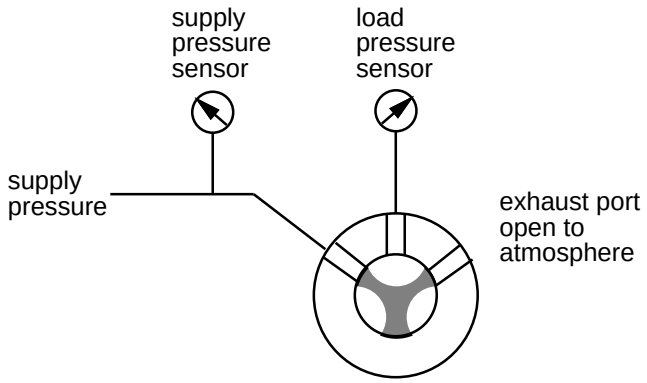

Figure 3.8: Pneumatic connections for testing the TBV control section.

the air supply was connected to the supply port, along with a pressure sensor; an additional sensor was connected to the load port, and the exhaust port was left open to the atmosphere, as shown in Figure 3.8. A simple proportional control loop commanded the motor to various angular positions, and the holding current and load and supply pressures were recorded, as the motor drove the control section through three revolutions. This process was repeated for supply pressures from 0 atm gage to 4 atm gage.

In Figure 3.9, load and supply pressures were measured and plotted as a function of angular position and supply pressure. From the 0 atm gage supply pressure plot, everything is at atmospheric pressure. The only thing that can be drawn from that data set is that sensor noise does not seem significant, being less than 0.05 atm in magnitude.

However, the other plots require some more interpretation in order to be clearly understood. With the encoder set to 2000 counts per revolution, each plot shows three complete revolutions of the control rotor within its stator: 0-2000 counts, 2000-4000 counts, and 4000-6000 counts. Consider one such revolution, from 0 to 2000 counts. Because the rotor has three blades, the plots should exhibit three distinct peaks over one revolution. In particular, the ranges of 400-600 counts, 1100-1300 counts, and 1700-1900 counts correspond to when the supply is charging the load, as shown at the left of Figure 3.2, while the ranges of 100-300 counts, 700-900 counts, and 1400-1600 counts

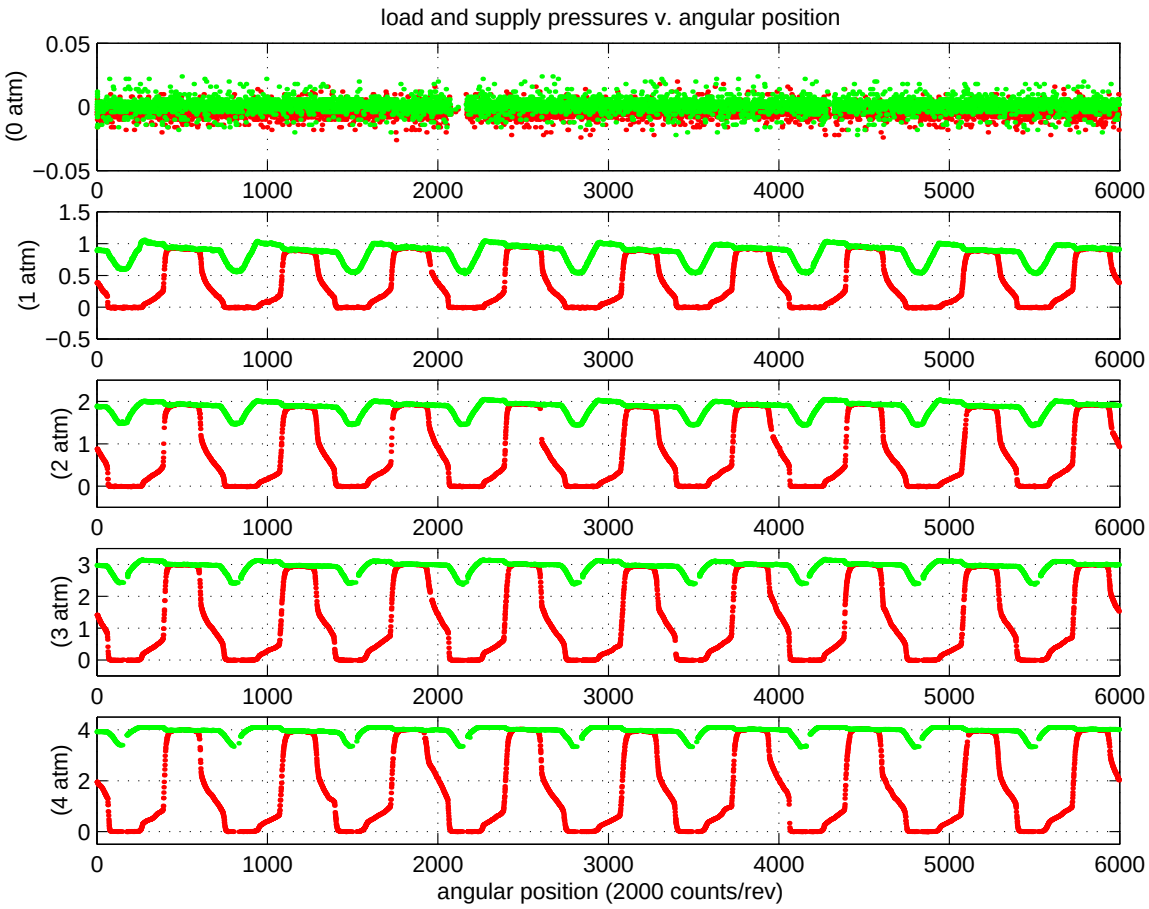

Figure 3.9: Control section: load and supply pressures plotted as a function of angular position for various supply pressures from 0 atm gage to 4 atm gage.

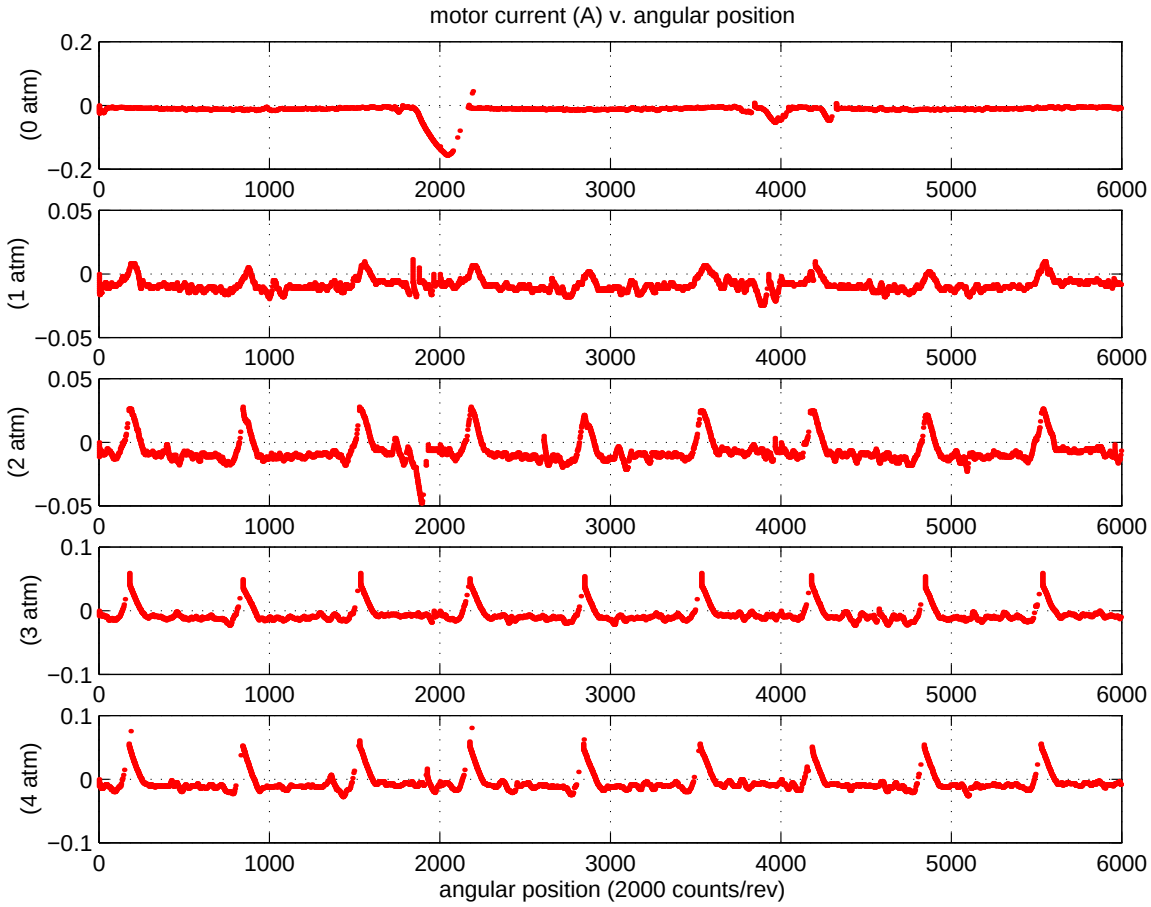

Figure 3.10: Control section: motor current required to hold current angular position, plotted as a function of angular position for various supply pressures from 0 atm gage to 4 atm gage.

correspond to when the load is discharging through the exhaust, as shown at the right of Figure 3.2. The hold position is more difficult to see, but corresponds to 650 counts, 1350 counts, and 1950 counts, as the load pressure falls due to the leaky clearance seal.

Note also that the supply pressure, measured right at the supply port of the control section, drops by 0.5 atm. Because the control stator was constructed with six ports to ensure a symmetric part that could be more easily fabricated on a lathe, the supply port is connected directly to a port that was left open to the atmosphere, as shown at the right of Figure 3.2.

In addition, the current required to hold the current angular position was also recorded and plotted in Figure 3.10 as a function of angular position and supply pressure. Upon further

examination of the figure, it is clear, for each supply pressure greater than atmospheric pressure, that each plot must show three peaks per revolution, and that there are indeed three revolutions in each plot. Ignoring the stickiness of the rotor that is evident in the uppermost plot around 2000 counts and the corresponding stickiness in the 2 atm gage plot, the peak positive current required to hold the control rotor in its current angular position is 75 mA, when the absolute supply pressure is nominally 5 atm. From Figure 3.7, this corresponds to a torque of 2.2 mNm.

The bottom line is that, for the prototype with its nominal control rotor diameter of 12.7 mm, the control section exerts a torque of 2.2 mNm, when the supply pressure is 5 atm absolute.

For a sanity check, we can compare this maximum experimentally determined torque of 2.2 mNm to that calculated using Equation 3.1. This maximum torque would occur when the mass flow rate is a maximum, which happens when the air at supply pressure rushes into the load chamber, initially at atmospheric pressure. With a supply pressure of 5 atm absolute, the mass flow rate $\dot{m}_{control}$ through the control port orifice of 1.6 mm diameter is then $1.4 \cdot 10^{-3}$ kg/s. Since the flow is choked, the velocity at 293K is then 343 m/s, with a corresponding force of 0.17 N and a torque of 1.1 mNm acting on a rotor radius of 6.35 mm. Amazingly, this is within a factor of 2 of the experimental result, although the astute reader will wonder if such a calculation is applicable to the results of a static test, especially since the flow into the load should have gone to zero, assuming leaks are small. However, as pointed out above, the peaks in the test correspond to points when the supply port is directly connected to an exhaust port, as shown in the rightmost drawing of Figure 3.2. And it is this condition that is assumed in the theoretical calculation, so although the peak torque value does not directly correspond to the case of the supply charging the load, it does give a measure of the magnitude of that torque. So the peak torque value is actually a relevant and useful number to have been determined both theoretically and experimentally in this fashion.

Because the peaks in the commanded motor current correspond to points when the supply port is connected to an exhaust port— a situation which mimics that which happens initially when

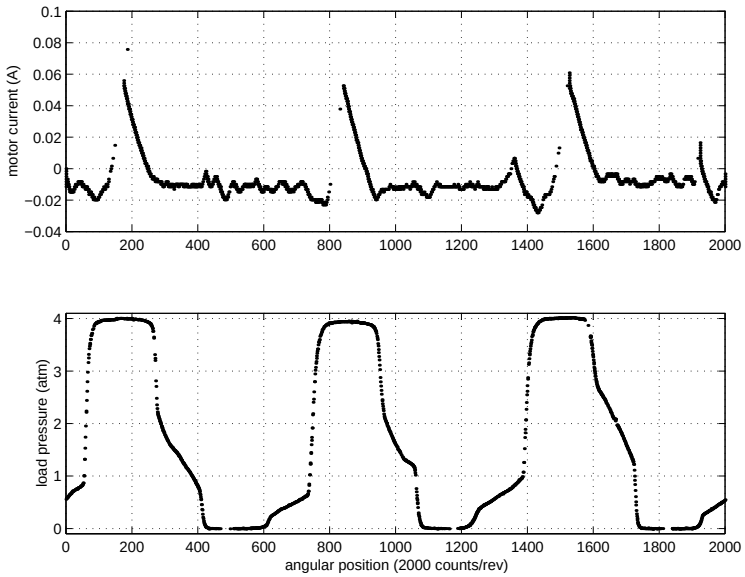

Figure 3.11: Commanded motor current and load pressure, both as a function of angular position, for a supply pressure of 4 atm gage. This is just a magnification of the lowermost plots of Figure 3.10 and a shifted version of Figure 3.9, as discussed in the text.

the supply port is connected to the load port— it seems reasonable to shift the load pressure plot by $\frac{\pi}{3}$rad, or $\frac{2000}{6} = 333$ counts, and replot the motor current and load pressure against the same angular position axis, as in Figure 3.11. This gives a measure of maximum load pressure and worst case control torque for the same angular position. Note that points of zero commanded motor current— and zero control torque— correspond approximately to the trailing edges of the peaks in the load pressure at counts 250, 900, and 1600. It is then possible to assume that there are angular positions that can charge the load while little torque is required to hold that position, that the drive section can be sized just to overcome the worst case control torque, and that the brake section can be sized purely in relation to the drive section.

In addition, it is obvious that the control torque can help or hinder the movement of the control rotor. By appropriate selection of the orientation of the control rotor with respect to the drive rotor, the control rotor can actually assist in moving itself.

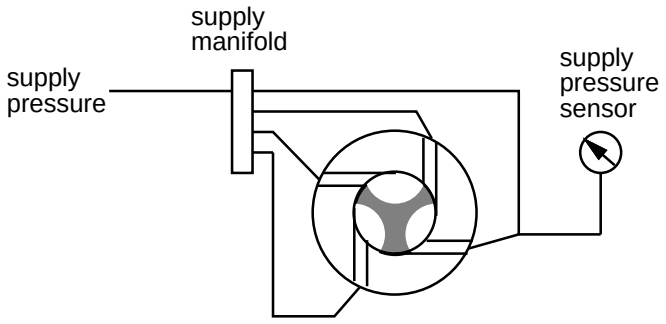

Figure 3.12: Pneumatic connections for testing the TBV drive section. Note that supply pressure is measured at one of the four supply ports of the drive stator, and also that each of the pneumatic tubes that connecting the manifold to one of supply ports is of equal length.

3.2.2 Drive Section, Experimental Results

The drive section was also tested in a similar fashion, by first mounting the drive rotor so that it spun freely in its matched stator, and then coupling the assembly to the motor. Next, the four supply ports were connected to a common air supply, as schematically shown in Figure 3.12. Finally, a simple proportional control loop commanded the drive rotor to various angular positions, and the holding current recorded for those positions. For each of the supply pressures from 0 atm gage to 4 atm gage, the motor drove the rotor through three revolutions, and the average holding current was plotted in Figure 3.13.

For correct operation of the TBV, we must choose the drive section to exert enough torque to break the control section away from its point of maximum torque. Since the control section was determined to exert a maximum torque of 2.2 mNm, we add in a margin of safety and require the drive section to generate 50% more torque in magnitude; this allows the drive section to perform as advertised and actually drive the control section. For the purposes of this analysis, we consult Figure 3.7 and select the torque corresponding to a motor current of 100 mA; this torque is then 3.1 mNm. From Figure 3.13, we know that the drive section can generate an average torque of 3.1 mNm with a nominal supply pressure of 3.5 atm gage, so this value is not a problem.

For those interested in how well theory predicts reality, with a drive port diameter of

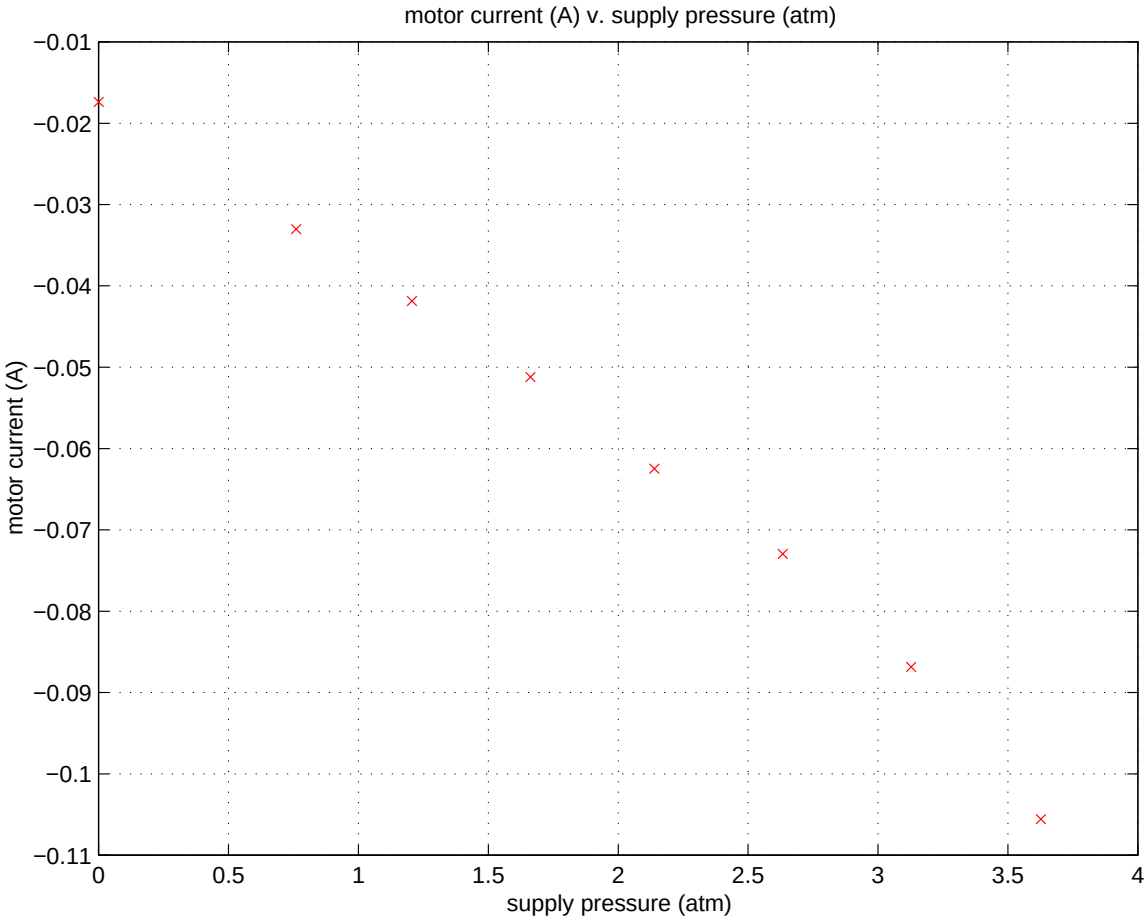

Figure 3.13: Drive section: average motor current required to hold current angular position, plotted as a function of supply pressure.

1.6 mm, an upstream pressure of 4.5 atm absolute, a downstream atmospheric pressure, and a choked flow, the corresponding mass flow rate is $1.3 \cdot 10^{-3}$ kg/s, and Equation 3.2 predicts a torque of 4.3 mNm, which is remarkable close to experimental reality.

3.2.3 Brake Section, Experimental Results

For the brake section, the simple band brake provides an uncomplicated means of slowing and stopping the rotors. A prototype band brake was constructed, consisting of a brass brake rotor press-fit onto a shaft, and fitted between two base plates held apart by spacer tubing. A strip of stainless steel shim stock served as the band, anchored to one of the base plates.

Two opposing forces must be applied to the opposite ends of the band in order to slow or stop the rotor. However, one of these forces– the one at the end of the band in the same direction as the direction of rotation– is much less than the other.

For testing purposes, the brake section was driven by the same motor/shaft encoder used in driving the control and drive sections. With the motor and brake assembly mounted horizontally, standard weights were hung from one end of the band, as shown in Figure 3.14. A simple proportional control loop was used to drive the rotor to various angular positions, and commanded motor current recorded for each of those positions. Three revolutions with each weight were recorded. The commanded current was limited to 250 mA; the test terminated when 66.6 mN was applied to band brake, and the commanded current railed into this limit. The average motor current required over the three revolutions for a given weight was then plotted in Figure 3.15.

3.2.4 Theoretical Mechanical Power Required for Band Brake

We find that a commanded motor current of 100 mA can counterbalance a brake force of approximately 40 mN. Extrapolating from the same data, an F_{min} of 80 mN must be applied to the band brake, 40 mN to generate the torque to oppose the drive section in the worst case, and

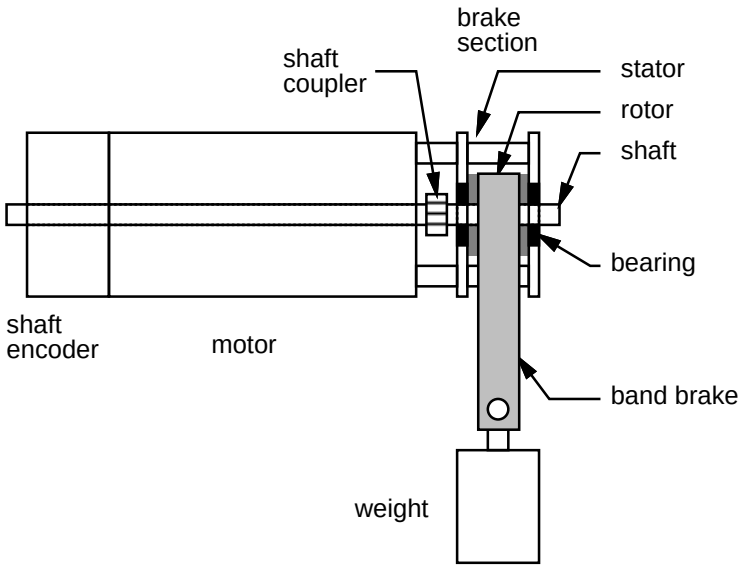

Figure 3.14: Illustrating the testing of the TBV brake section. The motor and brake assembly are mounted horizontally, with weights hung off the end of the band brake.

another 40 mN to slow the rotor down to a stop.[1]

As the minimum force is doubled to $F_{min} = 80$ mN, the torque to be generated by the band brake must also be doubled to 6.2 mNm. The torque τ is related to the forces at both ends of the band brake by the relation:

$$\tau = r(F_{max} - F_{min})$$

for a rotor radius r of 6.35 mm, the minimum force of 80 mN, and the torque of 6.2 mNm, the resulting value of the maximum force is then $F_{max} = 1.1$ N.

In addition, the minimum band brake force F_{min} applied at one end of the band is related to the maximum band brake force F_{max} by

$$F_{max} = F_{min} e^{\mu\alpha}$$

where μ is the coefficient of friction and α is the angle that the band subtends as it wraps around the rotor. With a maximum force of 1.1 N, a minimum force of 80 mN, and a wrap angle of 240°,

[1] Selection of the forces in this manner implies that the starting time and the stopping time are equivalent, since the magnitudes of the torque from the drive section will be equal to the magnitude of the torque from the brake section.

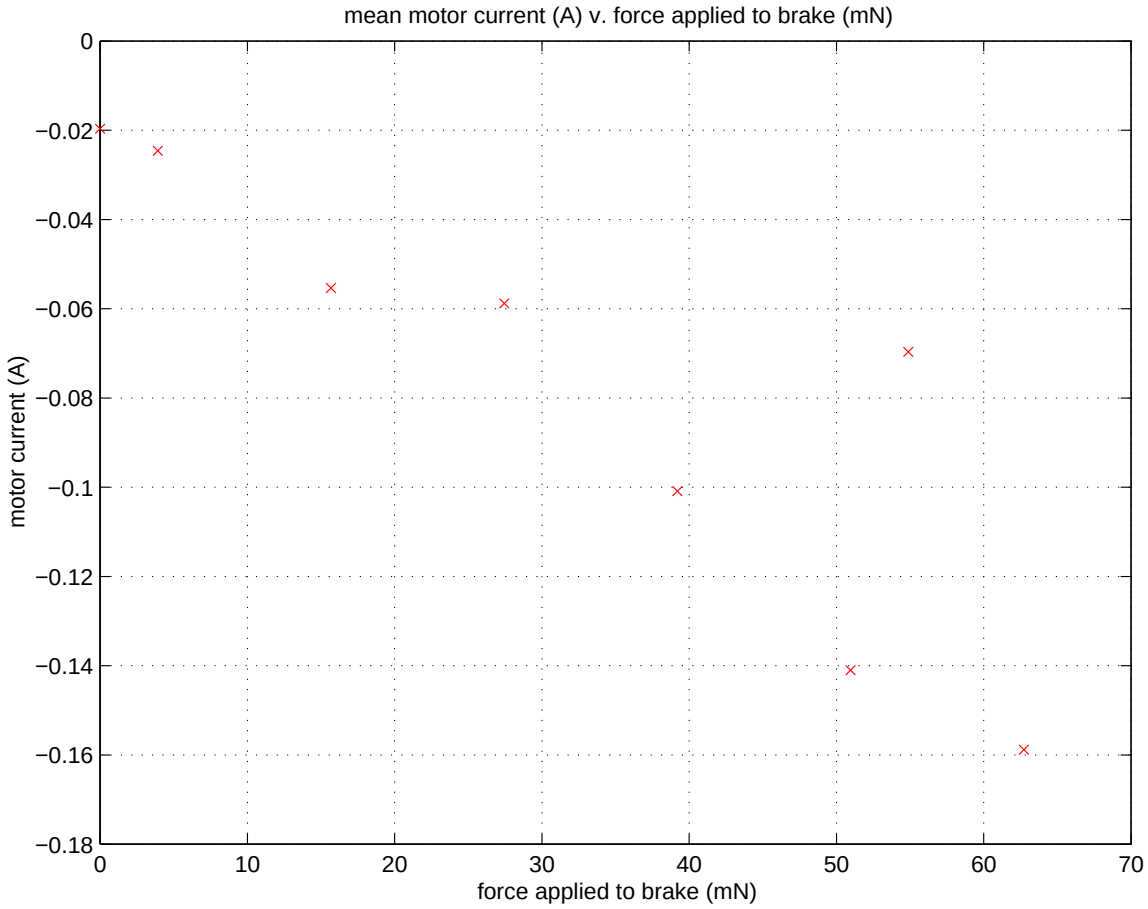

Figure 3.15: Average commanded motor current v. force applied to band brake. Amusingly, the outlier point was the first dataset recorded, before the brake rotor and band wore in.

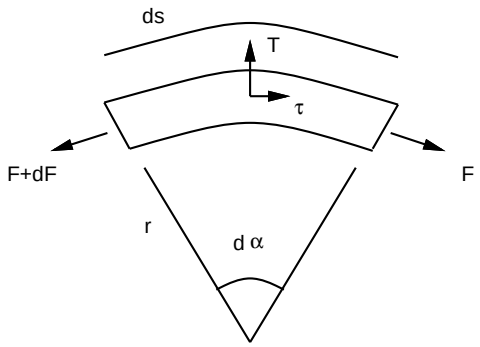

Figure 3.16: Differential element of band brake.

μ is experimentally found to be 0.62 for brass on stainless steel.

We also need to determine the length by which the band stretches when these two forces are applied to its ends. Considering a differential element of the band brake, there are four forces acting upon it, as shown in Figure 3.16: two largely opposing forces F and $F + dF$ acting at the ends of the element, another force T acting normal to the band, and force τ acting parallel to the band. Assuming $dF = \tau$ is small enough to be neglected, and that T can also be neglected since it is perpendicular to the direction of strain, the elongation of the band Δ is:

$$\begin{aligned}
\Delta &= \int_0^L \epsilon(s)ds \\
&= \int_0^{\frac{240}{360}2\pi} \epsilon(\alpha)rd\alpha \\
&= \int_0^{\frac{240}{360}2\pi} \frac{F(\alpha)}{AE}rd\alpha \\
&= \int_0^{\frac{240}{360}2\pi} \frac{F_{min}e^{\mu\alpha}}{AE}rd\alpha \\
&= \frac{rF_{min}}{AE}\frac{1}{\mu}e^{\mu\alpha}|_0^{\frac{240}{360}2\pi} \\
&= \frac{rF_{min}}{AE}\frac{1}{\mu}(e^{\mu\frac{240}{360}2\pi} - 1) \\
&= \frac{r}{\mu AE}(F_{max} - F_{min})
\end{aligned}$$

With a maximum force F_{max} of 1.1 N, a minimum force F_{min} of 80 mN, a friction factor μ of 0.62, a cross sectional area A of 5 mm by 25.4 μm, the Young's modulus of stainless steel at 210 GPa,

and a rotor radius of 6.35 mm, the resulting elongation Δ is 0.38 μm. This assumes that the band brake is chosen as short as possible, with a length of 26.7 mm, the arc length that results from the wrap angle above and the rotor radius.

Lest the 0.4 μm figure be contested, a back of the envelope calculation can be made to show its feasibility. Suppose the band brake experiences a force of 1.1 N down its entire length. The strain of the band is then $\epsilon = \frac{\sigma}{E} = \frac{F}{AE}$, and the corresponding elongation is $\Delta = L\epsilon = \frac{LF}{AE}$. Substituting the same values as above, with a length of 26.7 mm, the displacement is 1.1 μm. Since this is supposed to be an upper bound on the true displacement, the 0.38 μm value seems more reasonable.

The theoretical energy used by the brake over a single cycle is the product of F_{min} and this displacement, and if the brake is to applied at a frequency of 200 Hz, the mechanical power required is 6.2 μW.

Our figure of merit for this actuator is the power gain at 100 Hz, the power gain being defined as the ratio of the fluid power controlled and the power necessary for braking. However, we first need to determine the fluid power.

For the prototype, air at an absolute pressure of 5 atm flows through channels with a diameter of 1.6 mm. The maximum power delivered to an ideal dissipative load, as discussed in Section 1.4, occurs when the absolute load pressure is 3.6 atm, with a corresponding volume flow of 0.27 l/s and a velocity of 230 m/s. The power delivered to the load is 72 W.

With the power gain defined as the ratio of the output power to the input power, this gives us an insane power gain of $1.2 \cdot 10^7$ at 100 Hz.

For comparison, consider a DC motor that acts as both drive and brake sections, driving the control section. Because the motor can brake itself, the maximum necessary torque is half that required of the brake section, or 3.1 mNm. Because the drive section has three blades, the required angular velocity is one third of nominal frequency of actuation, or $2\pi\frac{100}{3}$rad/s. The power to the motor is then their product, or 0.65 W, and the corresponding power gain is 110.

Comparison of the two power gains reveals that the idea of the brake has merit– the TBV theoretically uses five orders of magnitude less power than a DC motor directly driving the control section. Although a practical implementation will certainly use more power, even having an order of magnitude power reduction is significant. Comparable 0.5 W Maxon motors are available at 12 mm diameters, with lengths of 17 mm. With appropriate design, the entire TBV could be fabricated to approximately the same dimensions, [2] but require significantly less mechanical power to control the same amount of fluid power.

On the other hand, this analysis assumes that there is enough slack in the band for the rotor to spin freely when the brake is not engaged. An actual implementation of the band brake would require much more care in the construction and actuation of the brake section.

3.2.5 Theoretical Actuation by Piezoelectric Stack

From the previous section, the theoretical band displacement was determined to be 0.4 μm. However, we have not yet addressed actuation of the band brake itself. To ground this discussion in a bit more reality, we assume that a 1 mm by 1 mm by 10 mm piezoelectric stack of PZT-5H is used to actuate the band brake. Consulting the product literature for [Morgan-Matroc] gives the material parameters and relations for actuator in this section.

Assuming a layer thickness of 200 μm, this gives a stack with 50 layers. Considering the theoretical band displacement, we give ourselves a huge margin of safety, and require the piezo to move 5 μm. This is a strain of $5 \cdot 10^{-4}$.

With this displacement, we can figure out the necessary voltage that should be applied to the stack. Since the displacement x is just the product of the voltage, the number of layers N, and material parameter d_{33}, the voltage is then:

$$V = \frac{x}{N d_{33}}$$

[2] The integrated prototype, with press-fit blocks joining the three sections together, stands 35 mm in height, but more than 10 mm is excess due to overdesign.

With a displacement of 5 μm, an N of 50, and a d_{33} of $593 \cdot 10^{-12}$, the voltage V should then be 170 V. Fortunately, this value is below the maximum voltage of 200 V, assuming that the maximum field is 1 kV/mm over a layer thickness of 200 μm.

The blocked force generated by the piezo F_{block} is:

$$F_{block} = \frac{\epsilon A}{S_{33}^{e}}$$

where ϵ is the strain, A is the stack cross sectional area, and S_{33}^{E} is the material compliance. With an ϵ of $5 \cdot 10^{-4}$, an A of 1 mm^2, and an S_{33}^{E} of $20.8 \cdot 10^{-12}$ m^2/N, the blocked force is 24 N, more than enough to actuate the band brake.

The final quantity to check is the power consumed by the piezo. First, we determine the piezo capacitance C:

$$C = N\frac{K_{33}^{T}\epsilon_0 A}{t}$$

where K_{33}^{T} is the material dielectric constant, ϵ_0 is the free space dielectric constant, A is the stack cross sectional area, N is the number of layers, and t is the layer thickness. With a K_{33}^{T} of 3400, an ϵ_0 of $8.85 \cdot 10^{-12}$F/m, an A of 1 mm^2, an N of 25, and a t of 200 μm, we arrive at a capacitance of 7.5 nF.

The power consumed by the piezo is then:

$$P = CV^2 f$$

With the capacitance and applied voltage from above, at 200 Hz we find a power consumption of 43 mW. The resulting power gain is then a slightly more down to earth value of $1.7 \cdot 10^3$.

Note that charge recovery techniques using an inductor and a pair of switches can reduce power consumption by an additional factor of five, so a power consumption of less than 10 mW would be reasonable.

3.2.6 Theoretical Actuation by Piezoelectric Bimorph

On the other hand, the stack with its surfeit of force is slightly overpowered for the job. Perhaps a better fit would be if the brake section were to be actuated by a parallel piezoelectric bimorph. Once again, consulting the product literature [Morgan-Matroc] leads us to the relevant material parameters and relations.

Consider a parallel piezoelectric bimorph of dimensions 5 mm by 4 mm by 0.5 mm, with an applied voltage of 100 V, the free deflection y at the tip of the bimorph is given by:

$$y = 3\frac{d_{31}VL^2}{t^2}$$

where d_{31} is a material parameter relating the applied voltage to the displacement, V is the applied voltage, L is the bimorph length, and t is the bimorph thickness. For a d_{31} of $274 \cdot 10^{-12}$ m/V, the displacement is 8.2 μm.[3]

The blocked force F_b is given by:

$$F_b = \frac{1}{2}Ed_{31}V\frac{Wt}{L}$$

where E is the Young's modulus, d_{31} is the same material parameter as before, V is the applied voltage, W is the bimorph width, L is the bimorph length, and t is the bimorph thickness. With an E of $5 \cdot 10^{10}$ N/m^2 and all other values given above, the blocked force is 270 mN.

If we assume that we operate in a regime where half the blocked force results in a displacement of half the free deflection, then the bimorph can actuate the brake section.

The capacitance of the bimorph can be found by using:

$$C = 2K_{33}^T\epsilon_0\frac{WL}{t}$$

where K_{33}^T is the material dielectric constant, ϵ_0 is the free space dielectric constant, W is the bimorph width, L is the bimorph length, and t is the bimorph thickness. With a K_{33}^T of 3400, an ϵ_0 of $8.85 \cdot 10^{-12}$F/m, and the piezoelectric dimensions given above, the capacitance is 2.4 nF.

[3] The maximum voltage across the bimorph is the maximum field of 10^6 V/m, over a thickness of 0.25 mm, or 250 V.

The power consumed by the piezo is then:

$$P = CV^2 f$$

With an f of 200 Hz, and the rest of the values above, the power consumed by the bimorph is then 4.8 mW, and could be on the order of 1 mW with appropriate charge recovery techniques.

The corresponding power gain for the valve with bimorph actuation is then $1.5 \cdot 10^4$, which is higher than that using the stack, because the bimorph is sized much more closely to the task at hand.

The resonant frequency of the piezoelectric bimorph sets a lower bound on the actuation speed of the bimorph. This resonant frequency f_r is given by:

$$f_r = \frac{N_1 t}{3L^2}$$

where t is the bimorph thickness, L is the bimorph length, and N_1 is a material frequency constant. For PZT-5H, N_1 is 1420 Hzm. The resulting resonant frequency is 9.5 kHz, giving a bimorph actuation time of 0.11 ms.

3.2.7 Summary of Prototype Theoretical Analysis

The valve, using a fluid drive section and a stack-actuated brake section, has a power gain 15 times greater than that of the control section directly driven by a DC motor.

The valve, using a fluid drive section and a bimorph-actuated brake section, has a power gain 140 times greater than that of the control section directly driven by a DC motor.

Note that these numbers were obtained by extrapolating from DC values obtained from a 5:1 scale prototype. Of particular concern is the brake section, whose correct operation is critical; theoretically, the numbers work out, but practically having a band riding just 1 μm or so away from the spinning rotor without jamming is asking for trouble. Once the brake has been engaged, disengaging it may prove to be problematic. To overcome such a difficulty, an actuator with larger

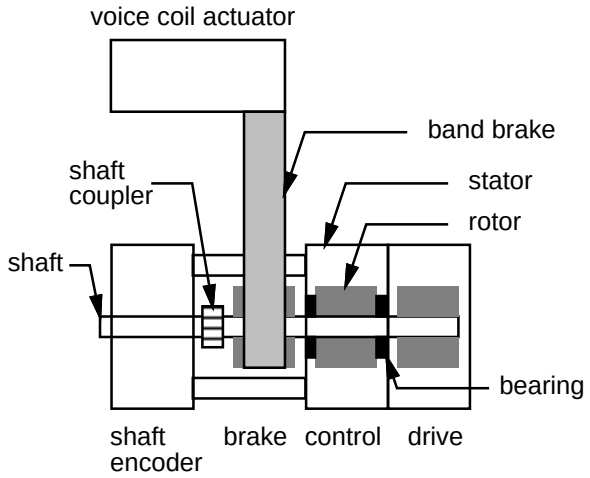

Figure 3.17: Illustrating the testing of the integrated TBV. Braking actuation is performed by a voice coil actuator pulling on the band brake.

stroke but little force for most of the stroke can be employed using a cam or toggle mechanism to disengage the brake.

Note also that the above analysis was performed assuming an unbalanced control section. If the control section had been balanced to reduce the torque from jet forces, both the drive torque required to accelerate the rotor assembly and the brake torque required to decelerate that assembly would be correspondingly reduced. Therefore, it is assumed that power gains in the balanced case will scale appropriately.

3.2.8 Experimental Results for Integrated Prototype

Calculations are nice, but having actual data is even better. In order to determine if a complete TBV could operate at all, the three sections were integrated together, as shown in Figure 3.17. Although pneumatic connections are not shown, the connections for both the control and drive sections are the same as shown in Figures 3.8 and 3.12. To ensure that the brake was actually disengaged, the brake section was actuated with a voice coil actuator (VCA) instead of a piezoelectric actuator.

Tests on the integrated prototype were performed by turning up the supply pressure of the

control section to approximately 1.25 atm gage, turning up the supply pressure of the drive section to break the control rotor away from its equilibrium position, and then actuating the brake section with a square wave at 28 Hz and a duty cycle of 75%. Note that this test was open loop, with the signal driving the VCA from a function generator.

The actuating square wave, VCA position, encoder count, and load pressure are plotted in Figure 3.18.

As the uppermost plot of Figure 3.18 shows, the band brake is disengaged when no current is driven through the VCA, and engaged otherwise. The VCA position is unfortunately uncalibrated, so although no quantitative conclusion can be drawn, it is obvious that the brake does not smoothly engage, but exhibits a second order response as it bounces into its final engaged position. Note that the angular position in the thirdmost plot of Figure 3.18 is approximately equivalent to that sketched in Figure 3.5.

The inertia of the solid brake disk J_{disk} is $\frac{\pi}{2}\rho r^4 h$, where ρ is the density, r is the disk radius, and h is the disk height. The inertia of the three bladed rotor J_{3blade}, with each blade occupying a $\frac{\pi}{3}$rad sector, is $\frac{\pi}{4}\rho r^4 h$, where ρ is the density, r is the rotor radius, and h is the rotor height. The total inertia of the rotor assembly J is then $2J_{3blade} + J_{disk}$. For the original brass rotors with a density of 8.47 g/cm^3, a radius of 6.35 mm, and a height of 5 mm, the inertia J is $2.2 \cdot 10^{-7}$ kgm^2. Following the development of Subsection 3.1.4, the time required to turn $\frac{\pi}{6}$rad is 16 ms, and the corresponding turn-on time is 32 ms.

To reduce inertia, the brass rotors were replaced with ones made of Delrin, with a density of 1.41 g/cm^3. The corresponding inertia J is then $3.6 \cdot 10^{-8}$ kgm^2. The time required to turn $\frac{\pi}{6}$rad is then 6.5 ms, and the corresponding turn-on time is 13 ms.

The pressure sensor has a dead volume of 20 mm^3, attached with 25 mm of 1.6 mm inner diameter tubing, to make a total volume of 70 mm^3. The charging time for the given supply pressure is on the order of 0.25 ms.

So it can be determined from the lower two plots of Figure 3.18, that the limiting factor is

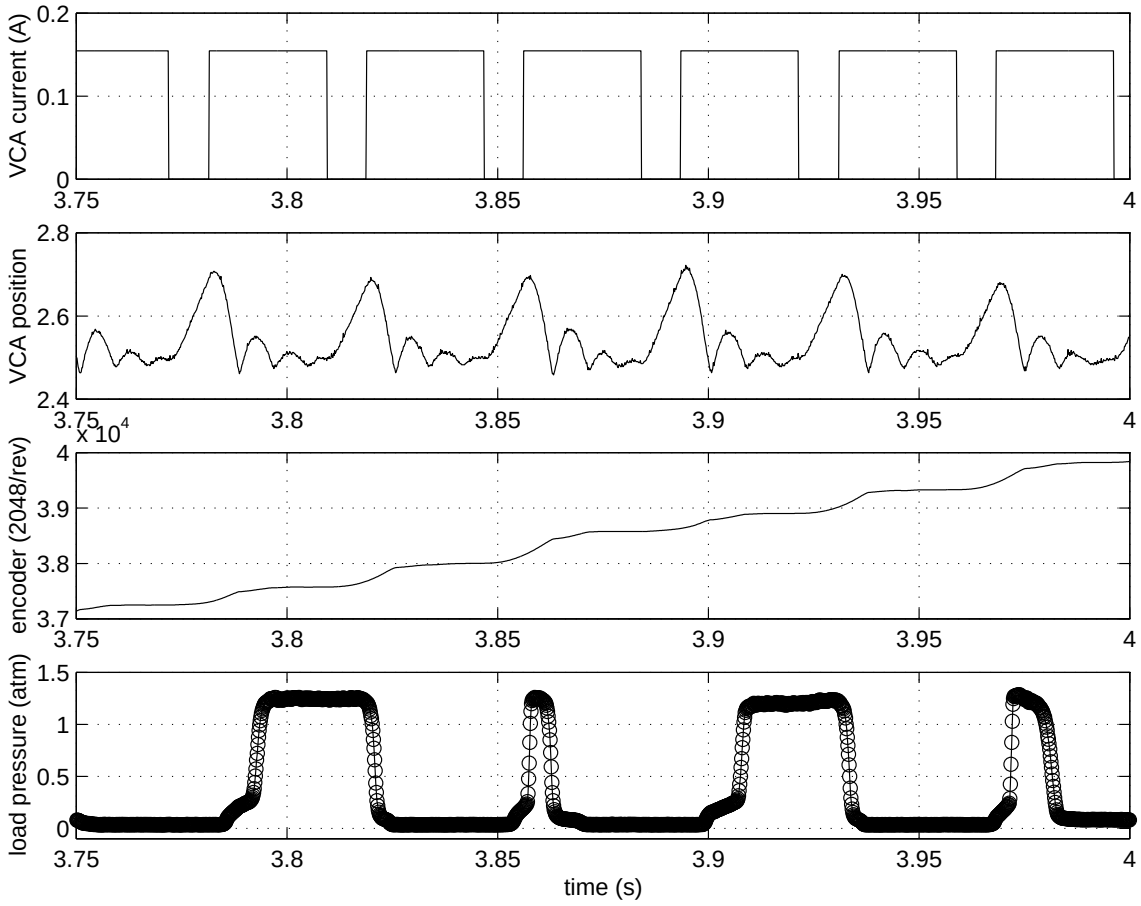

Figure 3.18: Open loop performance of valve prototype, with the brake driven by a square wave at 28 Hz (top). The brake is released when the current is zero, and actuated when the current is high; note that the units of the VCA position are arbitrary. The load pressure rises to a maximum as the brake holds the control rotor so that it charges the load. The brake is then released, and the load pressure falls as it is discharged to atmospheric pressure. The supply pressures for both the control and drive sections were purposely set low to prevent deafening of the operator and innocent bystanders.

the slowness of brake actuation.

Note that, from the periodicity of the uppermost two plots of Figure 3.18, we expect the bottom plot of load pressure to also be periodic. However, this is not necessarily the case, as the load pressure is dependent on the angular position of the control rotor. Small variations in the stopping position of the control rotor, unapparent on the plot of the angular position, could mean the difference between the supply pressure being connected to or disconnected from the load. This is why there is such a variation in the width of the pulses in the plot of load pressure.

3.3 Milliscale Extrapolation

In the previous section, the 5:1 scale prototype of the TBV was discussed. We now turn to an at-scale version of the TBV and analyze it for feasibility.

If we choose to construct the composite rotor for all three sections out of silicon, its density ρ is $2.33 \cdot 10^3$ kg/m^3. Selecting the rotor radius r_{rotor} to be 1 mm and the rotor height h_{rotor} to be 1.5 mm, assuming each of the three sections is 0.5 mm in height, the rotor mass m_{rotor} is $\rho\pi r^2 h$, or $1.1 \cdot 10^{-5}$ kg. Assuming a solid rotor, the resulting inertia J_{rotor} is $\frac{1}{2}mr^2$, or $5.5 \cdot 10^{-12}$ kgm^2.

As noted above, Newton's second law governs the operation of the TBV:

$$J_{rotor}\ddot{\theta} = \tau_{drive} - \tau_{control} - \tau_{brake} - \tau_{damping}$$

We reexamine all three sections of the TBV in turn, utilizing the equations of Section 3.1, and then include other damping terms, such as viscous damping and bearing losses, that were previously ignored.

3.3.1 Control Section, Milliscale Extrapolation

Estimating the torque from the control section is problematic. Following the discussion of the sliding valve in Subsection 2.2.2, although the control section is rotary, the control rotor can be

thought of as as a sliding valve. With its three buckets, one cycle– consisting of charging the load, discharging the load, and then returning to the same initial position– occurs over 120° or 2.1 rad.

Referring back to the theoretical discussion of Subsection 3.1.1, assuming that the control section has ports of 0.5 mm in diameter, with an absolute supply pressure of 6 atm, the maximum torque that the control section can generate occurs when the downstream pressure is at 1 atm absolute, and the flow is choked so that the maximum air velocity v_{max} is $\sqrt{kRT}$, or 343 m/s. The corresponding mass flow rate $\dot{m}_{control}$ is $1.7 \cdot 10^{-4}$ kg/s. Substituting into Equation 3.1, we arrive at a maximum control torque of $\tau_{control}$ of 21 μNm.

Parameters for an at-scale prototype of the control section are summarized in Table 3.1.

3.3.2 Drive Section, Milliscale Extrapolation

For the drive section, an optimistic estimate of the torque obtainable from this section can be obtained by referring to Subsection 3.1.2. Assuming that the absolute drive supply pressure of 6 atm is applied over drive ports of 0.5 mm diameter, and that a 2 atm pressure drop occurs through those ports, the corresponding mass flow rate $\dot{m}_{drive}$ is $1.6 \cdot 10^{-4}$ kg/s, with a corresponding velocity v_{drive} of 171 m/s. Substituting into Equation 3.2, we arrive at a maximum drive torque τ_{drive} of 41 μNm. Since this is greater than the control torque $\tau_{control}$ of 21 μNm, it is possible to drive the control section with the drive section. Including in the damping terms from Section 3.3.3, there is still sufficient torque available.

To determine the time required to move the control section to turn on or turn off the valve, we employ Equation 3.3. Taking the worst case torque as the drive torque, less the torques from the control section and the various bearing torques calculated in the next section, Δt is 0.65 ms. The turn-on/turn-off time is then twice this, or 1.3 ms.

Parameters for an at-scale prototype of the control section are summarized in Table 3.1.

parameter	symbol	value
rotor radius	r_{rotor}	1 mm
total rotor height	h_{rotor}	1.5 mm
rotor mass	m_{rotor}	$1.1 \cdot 10^{-5}$ kg
rotor inertia	J_{rotor}	$5.5 \cdot 10^{-12}$ kgm^2
shaft radius	r_{shaft}	0.5 mm
air temperature	T	293 K
air gas constant	R	287 J/kgK
ratio of specific heats	k	1.4
upstream control pressure	$P_{up,control}$	6 atm abs
downstream control pressure, worst case	$P_{down,control}$	1 atm abs
control port diameter		0.5 mm
maximum mass flow rate through control port	$\dot{m}_{control}$	$1.7 \cdot 10^{-4}$ kg/s
jet velocity	$v_{control}$	343 m/s, choked
control torque	$\tau_{control}$	21 μNm
drive port diameter		0.5 mm
upstream drive pressure	$P_{up,drive}$	3 atm abs
downstream drive pressure	$P_{down,drive}$	1 atm abs
mass flow rate through drive port	$\dot{m}_{drive}$	$8.5 \cdot 10^{-5}$ kg/s
jet velocity	v_{drive}	343 m/s, choked
jet force	F_{jet}	29 mN
average number of jets	$k_{jet,avg}$	1.5
drive torque	τ_{drive}	44 μNm
turn-on/turn-off time	$2\Delta t$	1.3 ms

Table 3.1: Summary of parameters for control and drive sections of a proposed at-scale prototype of the TBV.

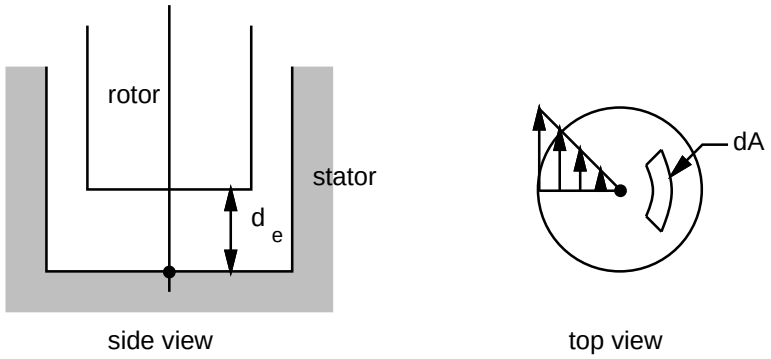

Figure 3.19: Viscous damping on the end of the rotor. Assuming that the velocity profile is linear, the velocity on the end $v_e(r)$ is sketched as shown, with d_e being the end clearance.

3.3.3 Other Damping Terms for Milliscale Extrapolation

There are other factors reducing the torque available to drive the TBV. The two primary ones are viscous damping of the rotor due to the air in the clearance between the rotor and the stator, and bearing friction from the two bearings upon which the rotor shaft is mounted.

To determine the viscous damping on the rotor, we follow the analysis presented in [Field, 1991], and first examine the damping at the ends of rotor, and then the damping on the sidewall of the rotor.

For the ends of the rotor, consider the rotor in its housing, as shown in Figure 3.19. Adopting a cylindrical coordinate system and assuming a linear velocity profile, the magnitude of the velocity on the ends of the rotor $v_e(r,z)$ is:

$$v_e(r,z) = \frac{z}{d_e}\omega r$$

with d_e defined as the end clearance, ω the angular velocity of the rotor, and R the rotor radius. On the ends of the rotor, a differential area element dA experiences a torque $d\tau$ equal to $\sigma_{z\theta} r dA$, where $\sigma_{z\theta}$ is the shear stress, on a plane with its normal in the z direction, acting in the θ direction. In this case, $\sigma_{z\theta}$ is related to the velocity gradient in the z direction by

$$\sigma_{z\theta} = \mu\frac{dv_e}{dz} = \frac{1}{d_e}\mu\omega r$$

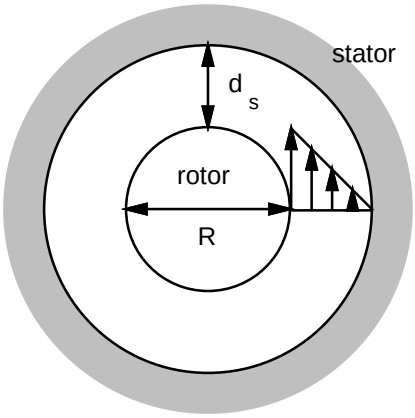

Figure 3.20: Viscous damping on the sidewall of the rotor. Assuming that the velocity profile is linear, the velocity on the sidewall $v_s(r)$ is sketched as shown, with d_s being the sidewall clearance.

where μ is the viscosity of air. Integrating over the end of the rotor, the viscous damping torque $\tau_{vd,e}$ is

$$\begin{aligned} \tau_{vd,e} &= \int\int \sigma_{z\theta} r dA \\ &= \int_{r_1}^{r_2} \int_0^{2\pi} \frac{1}{d_e} \mu\omega r^2 r dr d\theta \\ &= \frac{\pi}{2} \frac{\mu}{d_e} (r_2^4 - r_1^4)\omega \end{aligned}$$

With a μ of $1.8 \cdot 10^{-5}$ Ns/m^2, a clearance d_e of 5 μm, an inner radius r_1 of 500 μm, and an outer radius of r_2 of 1 mm, the viscous damping term can be reduced to $\tau_{vd,e} = K_{vd,e}\omega$, where $K_{vd,e}$ is $5.3 \cdot 10^{-12}$ Nsm.

On the sidewall of the rotor, adopting a cylindrical coordinate system and assuming a linear velocity profile, the velocity on the sidewall $v_s(r)$ is:

$$v_s(r) = \frac{R + d_s - r}{d_s} \omega R$$

with d_s defined as the sidewall clearance, ω the angular velocity of the rotor, and R the rotor radius.

A sidewall area element experiences a torque $\tau_{vd,s}$ proportional to the shear stress σ_{rr}, on a plane normal to the r direction, acting in the r direction. The magnitude of σ_{rr} is related to the

velocity gradient in the r direction by the viscosity of air μ:

$$|\sigma_{rr}| = \mu|\frac{dv_s}{dr}| = \frac{1}{d_s}\mu\omega R$$

Given the rotor radius R and the rotor height h, the torque $\tau_{vd,s}$ is then:

$$\tau_{vd,s} = |\sigma_{rr}|RA = (\frac{1}{d_s}\mu\omega R)R(2\pi Rh) = 2\pi\mu\frac{R^3h}{d_s}\omega$$

With a μ of $1.8 \cdot 10^{-5}$ Ns/m^2, a clearance d_s of 5 μm, a rotor radius R of 1 mm, and a rotor height h of 1.5 mm, the viscous damping term can be reduced to $\tau_{vd,s} = K_{vd,s}\omega$, where $K_{vd,s}$ is $3.4 \cdot 10^{-11}$ Nsm.

The total viscous damping torque τ_{vd} is then

$$\tau_{vd} = K_{vd}\omega$$

where $K_{vd} = 2K_{vd,e} + K_{vd,s}$, because there are two ends and one sidewall. With the values above, K_{vd} is $4.5 \cdot 10^{-11}$ Nsm.

However, even if the angular velocity is 5000 rad/s, the resulting viscous damping torque is only on the order of 0.22 μNm in magnitude, which is negligible compared to the torques from the control, drive, or brake sections.

Although viscous damping can be neglected, bearing friction is of greater concern. From [RMB Bearings], a starting torque of 18 μNm is required to overcome the friction in a UL1304X stainless steel radial bearing with an applied radial load of 0.75 N. Throughout the rest of this section, it is assumed that the applied radial load is linear with the starting torque.

The trick is now to determine the worst case radial load from each section. For the control rotor, this occurs when one of the buckets sits directly opposite the supply port and a pressure drop ΔP of 5 atm occurs, putting a radial load of $A\Delta P$ on the bearing. From geometrical considerations, each of the three buckets has an angular measure of $\frac{\pi}{2}$, leading to an area A of $\frac{\pi}{2}rh$ where r is the inner radius of the rotor and h is the rotor section height. For an inner radius of 0.5 mm, and a section height of 0.5 mm, this gives a radial load of 0.20 N, which translates into a starting torque of 4.8 μNm. This is appreciable compared to the control torque.

For the drive rotor, the worst case radial load occurs when one of the jet ports is blocked by the rotor. With an upstream pressure of 3 atm absolute and a downstream atmospheric pressure across a cross sectional area of 0.5 mm in diameter, the radial load is 40 mN, corresponding to a friction torque of 0.95 μNm. This is negligible, compared to both control and drive torques.

For the brake rotor, assuming a band brake, the worst case radial load is dependent on the force on the band. For a wrap angle of 300° and a friction coefficient of 0.25, the worst case radial load is 0.14 N, corresponding to a friction torque of 3.3 μNm. This is also appreciable compared to the control torque.

Appropriate design can reduce each of these radial loads, and consequently lower the starting torque required for the bearing. For the control rotor, switching to a two bucket control rotor with two supply ports, two load ports, and two exhaust ports leads to a radially balanced rotor. This however doubles the control torque and increases actuation time. For the drive rotor, more supply ports and blades can be introduced, as long as the ratio of ports to blades remains $\frac{n}{n-1}$. For the brake rotor, three band brakes can be used— one in the middle pulling to one side, and two others above and below the middle band, pulling to the other side.

Parameters for damping are given in Table 3.2.

3.3.4 Brake Section, Milliscale Extrapolation

For the brake section, we select the same band brake of 1 mil stainless steel used in the analysis of the prototype. To size the brake section appropriately, we choose the starting time to be equal to the stopping time; that is, the time to spin the rotor up from rest to a maximum speed is equivalent to the time to spin the rotor down from that maximum speed back to rest. Following the discussion in Subsections 3.2.1 and 3.2.4, we need only have brake torque be twice the drive torque.

The required brake torque is then 87 μNm.

For the purposes of calculation, we use a PZT-5H stack to actuate the band brake, with a safety margin of 3 in the displacement. Following an analysis similar to that of the prototype

parameter	symbol	value
end clearance	d_e	5 μm
sidewall clearance	d_s	5 μm
viscous damping constant from end of rotor	$K_{vd,e}$	$5.3 \cdot 10^{-12}$ Nm
viscous damping constant from sidewall of rotor	$K_{vd,s}$	$3.4 \cdot 10^{-11}$ Nm
total viscous damping constant	K_{vd}	$4.5 \cdot 10^{-11}$ Nm
viscous damping torque at $\omega = 5000$ rad/s	τ_{vd}	0.22 μNm
worst case radial load		
from control section		0.20 N
from drive section		0.040 N
from brake section		0.14 N
worst case starting torque		
from control section		4.8 μNm
from drive section		0.95 μNm
from brake section		3.3 μNm

Table 3.2: Summary of parameters for damping torques of an at-scale prototype of the TBV.

presented above, we summarize the results in Table 3.3. The bottom line is that the stack will consume 0.90 mW, with a power gain of $1.0 \cdot 10^4$ at 100 Hz.

The stack is tremendously overpowered for the application at hand. Suppose we replace the stack with a piezoelectric bimorph, following Subsection 3.2.6. Assuming a desired force equal to that of the minimum brake force and a desired displacement with a safety factor of 3, the results are summarized in Table 3.4.

In comparison, consider a piezoelectric bimorph sitting over a 0.5 mm diameter orifice, controlling air at a supply pressure of 6 atm absolute. The resulting flap valve is one of the simplest possible seating valves, with a maximum force $A\Delta P$ of 99 mN and a maximum displacement $\frac{D}{4}$ of 125 μm.

Following the equations of Section 3.2.6, we can search for a bimorph that can actuate the flap valve while consuming minimum power. Sweeping the length from 1 to 25 mm in increments of 0.5 mm, the width from 1 to 10 mm in increments of 0.5 mm, and the thickness from 0.1 to 2 mm in increments of 0.1 mm, the results are summarized in Table 3.5. Comparing the resulting power

parameter	value
brake torque	87 μNm
maximum brake force	120 mN
minimum brake force	32 mN
brake friction	0.25
band width	0.5 mm
band thickness	1 mil, or 25.4 μm
wrap angle	300°
band length	5.2 mm
Young's modulus	$2.1 \cdot 10^{11}$N/m^2
band displacement	0.13 μm
brake energy per cycle	4.3 nJ
brake frequency	200 Hz
theoretical brake power required	0.85 μW
fluid power controlled	9.1 W
theoretical power gain	$1.1 \cdot 10^7$
piezo stack dimensions	0.5 mm by 0.5 mm by 3.0 mm
layer thickness	200 μm
number of layers	15
stack maximum voltage	200 V
stack applied voltage	89 V
stack free displacement	0.8 μm
stack strain	$2.7 \cdot 10^{-4}$
stack blocked force	3.2 N
stack capacitance	0.56 nF
stack power at 200 Hz	0.90 mW
power gain at 100 Hz with stack	$1.0 \cdot 10^4$

Table 3.3: Parameter summary of theoretical PZT-5H stack actuation of stainless steel band brake for at-scale TBV.

parameter	value
desired force	32 mN
desired displacement	0.4 μm
bimorph dimensions	4 mm by 1.8 mm by 0.7 mm
applied voltage	30 V
blocked force	65 mN
free displacement	80 μm
resonant frequency	21 kHz
bimorph actuation time	0.048 ms
bimorph power at 200 Hz	56 μW
power gain at 100 Hz with bimorph	$1.6 \cdot 10^5$

Table 3.4: Parameter summary of theoretical PZT-5H bimorph actuation of stainless steel band brake for at-scale TBV.

parameter	value
desired force	99 mN
desired displacement	125 μm
bimorph dimensions	17.5 mm by 8 mm by 0.4 mm
applied voltage	160 V
blocked force	200 mN
free displacement	252 μm
bimorph resonant frequency	620 Hz
bimorph actuation time	1.6 ms
power consumption at 100 Hz	54 mW

Table 3.5: Parameter summary of theoretical PZT-5H bimorph actuation of flap valve.

parameter	as built	projected
turn-on time, turn-off time	20 ms	1.1 ms
on/off pressure ratio	≥ 20	≥ 20
orifice	diameter 1.6 mm	diameter 0.5 mm
volume flow rate	0.28 l/s	0.028 l/s
supply pressure	5 atm	6 atm
working pressure	2.6 atm	3.2 atm
controlled fluid power	72 W	9.1 W
ideal actuation power	6.2 μW	0.85 μW
theoretical brake power using bimorph at 200 Hz	4.8 mW	56 μW
power gain using brake	15 000	160 000
dimensions	25 mm diameter, 17 mm height	5 mm, 3 mm, 2 mm
volume	33000 mm^3	18 mm^3

Table 3.6: Turbine brake valve parameter summary.

consumption to that of the bimorph required for the TBV band brake, it appears as if we can realize a three order of magnitude savings in power consumption.

3.4 Conclusions/Summary

Table 3.6 provides a brief summary of the data presented in this chapter.

Though this implementation of a self-driven design seems to be successful at the prototype scale, there are a number of issues that need to be resolved:

- Tight clearances are required to ensure that leaks are negligible.

- In order to preserve tight clearances, alignment between sections is critical.
- To preserve alignment and reduce frictional losses, bearings are required, increasing volume and cost.
- Crucial to the operation of the band brake is that it not jam. Unfortunately, ensuring that the band remains just off the brake rotor until the brake is engaged is nontrivial; having an actuator that would provide minimum force over a large displacement for full disengagement and maximum force over a small displacement to full engagement would be useful.
- The lifetime of the TBV is also an unresolved question. Wear on the stainless steel band and brake rotor were observed in the operation of the integrated prototype, and such wear not only reduces the lifetime of the device, but also necessitates that the brake actuator be able to handle the extra displacement required to engage the brake as the brake rotor shrinks in size.
- Angular position needs to be sensed, so that control can be effective. A potential solution to this problem that requires no sensing would be the addition of another section to the valve, with appropriate detents. These detents could be aligned with the control section so that the drive section just needs to overcome the fluid torque from the control section and the additional torque imposed by the detents.

However, compare the 56 mm^3 volume of the piezoelectric bimorph for the flap valve with the 5.0 mm^3 of the brake bimorph. The order of magnitude reduction in actuator volume might be worth overcoming the above problems.

Although the TBV seems to be a reasonable design, the design tradeoffs between the tight clearances required to keep leakage low and the bearing play that widens those clearances, coupled with the problem of aligning the entire rotor so that it does not jam in the stator, make the design less appealing. In the next chapter, we explore another design that attempts to remedy these problems.

Chapter 4

Pneumatic Oscillator and Electrostatic Clamp

The turbine brake valve requires bearings in order to maintain the necessary clearance seals on the control section, and brake wear certainly reduces the overall lifetime of the valve.

Following the terminology introduced at the end of Chapter 2, we propose a hybrid actuator with a pneumatic oscillator as the secondary actuator and a electrostatic clamp as the primary actuator. By clamping the oscillator at the extremes of its motion, the hybrid actuator can be turned on and off. The oscillator/clamp design combines the simplicity of a seating valve with the advantage of a brake actuator that needs zero displacement.

In our design, the pneumatic oscillator has a membrane that moves back and forth as the pressure difference across the membrane changes. As the membrane moves to one side, a magnet embedded in the membrane triggers a magnetically-actuated valve to switch open. Because of positive feedback, opening the valve alters the pressure difference across the membrane, forcing it back. The magnet then moves away from the valve, closing it again. The pressure difference falls again as air discharges through an orifice, and the membrane moves towards the valve again,

repeating the cycle.

By clamping the membrane at either end of its range of travel, the oscillator can be stopped. This clamping can be accomplished by an electrostatic actuator. By energizing the clamp at the appropriate time, the oscillation frequency can be modulated. Because the membrane is moved by the oscillator and not the electrostatic primary actuator, the primary only needs to clamp and hold the membrane.

For the 10:1 scale prototype that was constructed, at 5 Hz, such a primary actuator consumes a theoretical 0.22 mW. For comparison, consider the Hoerbiger-Origa Piezo 2000, a commercially available directly-driven valve, that consumes 0.14 mW at the same frequency, at an operating pressure of 2.2 atm absolute with nominal flow rate of 25 ml/s[Hoerbiger-Origa]. It is expected that an at-scale prototype would have a lower power consumption.

In this chapter, we report on progress towards fabricating such a hybrid actuator, intended to operate at 100 Hz with a stroke of 0.5 mm and a peak force of 100 mN. We have demonstrated operation of a 40x40x30 mm^3 oscillator at $5-6$ Hz with a stroke of 2.5 mm and a peak force of 1.1 N.

4.1 Oscillator, Theoretical Basis

We begin with an electrical analogue to a pneumatic oscillator, as shown in Figure 4.1. The operational amplifier and three lower resistors form a Schmitt trigger, whose output switches from 5 V to 0 V as the voltage on the inverting terminal rises past 3.75 V, and from 0 V back to 5 V as the inverting voltage falls below 1.25 V. With the addition of a resistor and capacitor combination connecting the output voltage to the inverting terminal, a self-starting electrical oscillator is formed. Assuming the output voltage is initially at 5 V and the capacitor is initially uncharged, the capacitor charges up until the inverting terminal voltage rises above 3.75 V. The output voltage then falls to 0 V, discharging the capacitor; when the capacitor voltage falls to 1.25 V, the output voltage switches

again to 5 V, and the cycle repeats. The oscillation frequency is controlled by the time constant of the resistor-capacitor combination, as well as the switching voltages of the Schmitt trigger positive feedback, and the supply voltage.

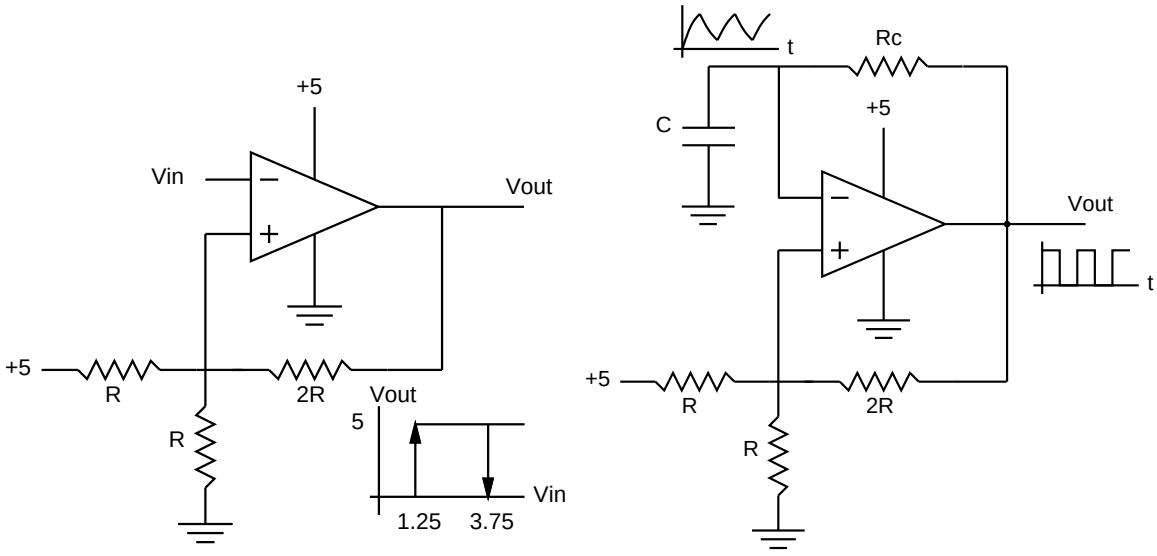

Figure 4.1: An electrical analogue to a pneumatic oscillator. The Schmitt trigger at left switches at 1.25 V and 3.75 V. Adding a resistor and capacitor gives the electrical oscillator at right. The waveforms for V_{out} and the voltage across capacitor C are also sketched.

The key elements of the electrical oscillator are the Schmitt trigger with its hysteretic relay characteristic, and the capacitor with its integrating action. A pneumatic oscillator should then have both of these elements, with mechanical feedback between the pressure in the accumulator and whatever serves as the relay.

A pressure-actuated normally closed diaphragm valve could realize that relay characteristic, with the appropriate diaphragm design prestressed so that it opens above a certain pressure and closes below a lower pressure. However, it was felt that critical elements should be material-independent and repeatedly realizable.

Fortunately, there are other ways to provide the desired characteristic; for instance, a single-ended pneumatic cylinder whose rod is mechanically attached to a normally closed valve forms a pressure actuated valve. Hysteresis can then be added by putting detents on the rod with the right

spring loading, so that the rod stays in one of two positions. This is illustrated in Figure 4.2. If the

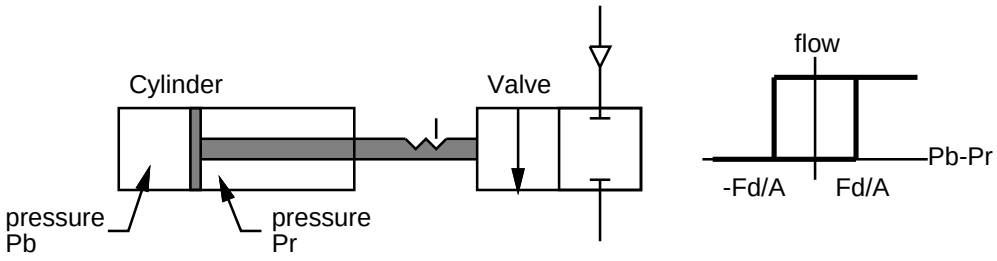

Figure 4.2: A pneumatic relay with hysteresis can be constructed from a single-ended pneumatic cylinder and two-position normally-closed valve (left). The valve is mechanically connected to the cylinder, and the detents on the rod result in the hysteretic relay transfer function between the pressure difference across the cylinder piston and the flow through the valve (right).

piston has cross sectional area A and the force required to move between the detents is F_d, when $P_b - P_r$ is greater than F_d/A, the valve should open, assuming the rod occupies negligible area on the face of the piston. When the pressure difference is less than $-F_d/A$, the valve should close. This gives the desired hysteretic relay transfer function.

With the appropriate connections, the relay above can then be turned into an oscillator. First, the valve inlet is connected to the air supply, and the valve outlet to the rod side of the cylinder, where flow through the valve charges the cylinder, closing the valve when the cylinder pressure reaches a critical value. Second, the blind side of the cylinder is connected a pressure reference that ensures the valve will tend to be opened; this is analogous to the voltage divider in the Schmitt trigger of Figure 4.1. Finally, orifices are added to discharge the cylinder rod side and limit the charging rate through the valve. The resulting pneumatic circuit is shown in Figure 4.3.

4.2 Oscillator, Implementation

A realization of the pneumatic circuit of Figure 4.3 is in Figure 4.4. To eliminate leakage between the rod and blind sides of cylinder, as well as reduce friction effects, a moving membrane is substituted for the moving piston. Hysteresis is provided by embedding a permanent magnet in this membrane, and placing two steel pieces at each end of the cylinder, instead of using detents.

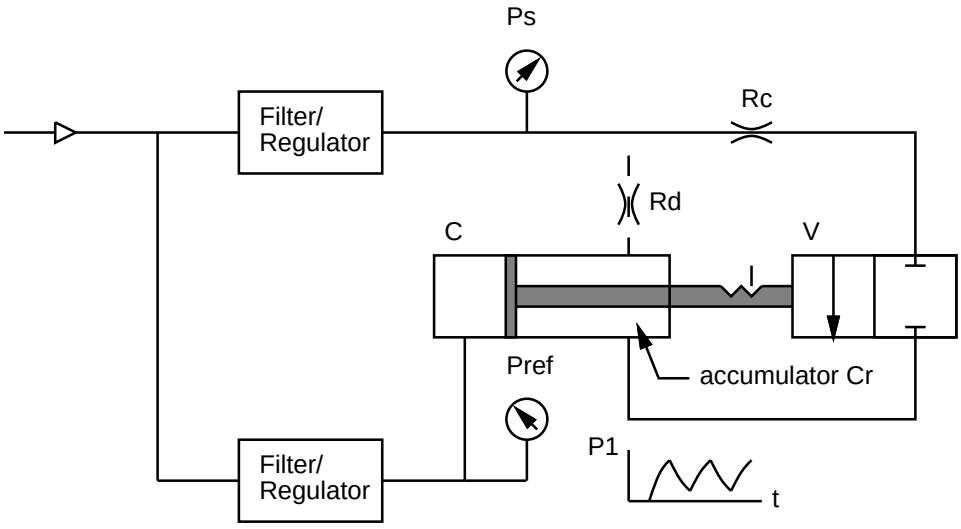

Figure 4.3: Pneumatic oscillator. The rod side of single-ended cylinder C is an accumulator C_r whose pressure alternately rises and falls as the rod travels back and forth, opening and closing valve V to charge C_r through restriction R_c. C_r discharges through R_d. The detents on the rod provide hysteresis.

To eliminate leakage from the cylinder, the mechanical connection between the valve and cylinder is replaced with a magnetic one. The valve is made magnetically actuated by fabricating the poppet out of steel; this is the leftmost of the steel pieces shown. Note that the chamber formed by the membrane and the valve body, to which the reference pressure source is connected, is referred to as the reference chamber, and that the chamber to which the magnetically-actuated valve is attached is referred to as the working chamber.

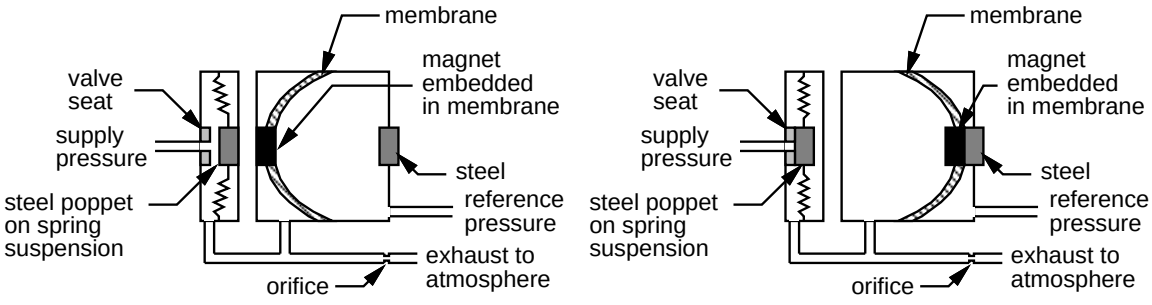

Figure 4.4: A realization of the pneumatic oscillator shown schematically in Figure 4.3, showing the oscillator at both extremes of motion, with magnetically-actuated valve open at left, and the same valve closed at right.

A more detailed description of the operation of the oscillator is given in the next section.

4.3 Oscillator, Simulation and Analysis

There are a number of equations that govern the resulting system:

- the deflection of the membrane due to the pressure difference across the membrane,
- the force from the magnet on the membrane,
- the mass flow rate through the magnetically-actuated valve,
- the mass flow rate through the discharge orifice,
- and the variable volume cylinder formed by the oscillator body and the membrane.

Assuming that the membrane moves slowly enough so that quasi-static approximations apply, the forces on the membrane determine the position of the membrane, which in turn determines the opening or closing of the magnetically-actuated valve. As the pressure difference across the membrane changes with the opening and closing of the valve, the balance of forces changes, closing the loop and causing the system to oscillate.

From [Timoshenko, 1959, p. 69], the deflection w of the membrane center due to a point load P is:

$$w = \frac{Pa^2}{16\pi D}$$

where a is the membrane radius, and $D = \frac{Eh^3}{12(1-v^2)}$, with E being the membrane modulus, v Poisson's ratio for the membrane, and h the membrane thickness. From [Hermida, 1998], the deflection w of the membrane center due to a pressure difference q across the membrane is:

$$w = \alpha a \sqrt[3]{\frac{qa}{Eh}}$$

where $\alpha = 0.278$ for material with Poisson's ratio of 0.5, a is the membrane radius, E is the membrane modulus, and h is the membrane thickness. Assuming superposition applies, the total deflection of the membrane center is the sum of these two quantities.

The force on the membrane is approximated as a point load from the embedded cylindrical magnet on the steel pieces at either end of the cylinder. Following [Magnet Sales and Manufacturing] to determine this point load, the flux density $B(x)$ at a distance x away from the surface of a cylindrical magnet with radius R and length L is:

$$B(x) = \frac{B_r}{2}\left(\frac{L+x}{\sqrt{R^2+(L+x)^2}} - \frac{x}{\sqrt{R^2+x^2}}\right)$$

where B_r is the residual flux density of the magnet and the distance is measured along the centerline of the magnet. In this case, the cylindrical magnet lies between two steel pieces. Assuming that the steel pieces are perfect ferromagnetic half-planes, if they are a distance d apart, then one face of the magnet lies a distance x away from one steel piece and a distance $d-L-x$ away from the other. The flux density is then $2B(x)$ and $2B(d-L-x)$, respectively, and the total force on the magnet is approximately:

$$F = \frac{4B(x)^2 - 4B(d-L-x)^2}{2\mu_0}A$$

where μ_0 is the magnetic permeability and A the cross-sectional area of the magnet. A plot of this force is given in the bottom half of Figure 4.6.

Referring to Figure 4.4, when the membrane has moved completely to the left, the embedded magnet opens the magnetically-actuated valve. The resulting pneumatic model is of an orifice charging a variable volume cylinder, with another orifice discharging that cylinder. When the membrane has moved completely to the right, the magnetically-actuated valve is closed, and the resulting pneumatic model is solely of the discharge orifice emptying the cylinder. The magnetically-actuated valve is modeled as either open or closed, open being defined as membrane within a small distance of the leftmost travel of the membrane, and closed being greater than this threshold.

Both the open magnetically-actuated valve and the discharge orifice are modeled following [Blackburn, 1960], where the mass flow rate $\dot{m}$ through an orifice is given by:

$$\dot{m} = \begin{cases} C_c A_0 \sqrt{P_1 \rho_1 \frac{2k}{k-1}} \sqrt{\left(\frac{P_2}{P_1}\right)^{\frac{2}{k}} - \left(\frac{P_2}{P_1}\right)^{\frac{k+1}{k}}} & \text{if } \frac{P_2}{P_1} \leq 0.528 \\ C_c A_0 \sqrt{P_1 \rho_1 \frac{2k}{k-1}} \sqrt{(0.528)^{\frac{2}{k}} - (0.528)^{\frac{k+1}{k}}} & \text{otherwise} \end{cases}$$

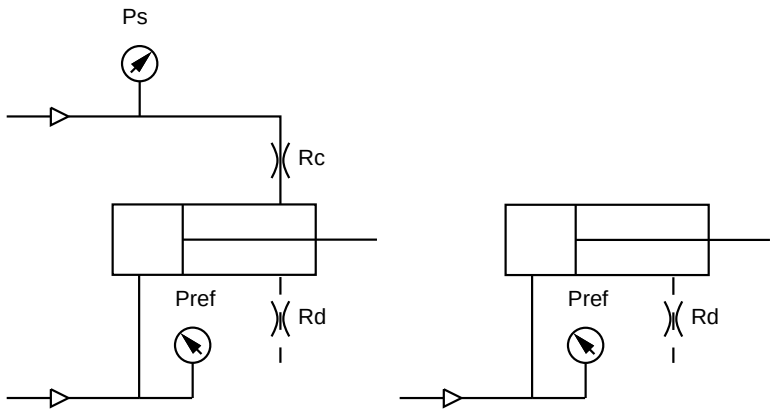

Figure 4.5: Pneumatic models of the oscillator with the magnetically actuated valve open (left) and with the magnetically actuated valve closed (right), corresponding to the left and right of Figure 4.4, respectively.

where C_c is the contraction coefficient, A_0 is the effective cross-sectional area of the orifice, P_1 is the upstream pressure, ρ_1 is the upstream density, P_2 is the downstream pressure, and k is the ratio of specific heats.

Under quasi-static assumptions, for the variable volume cylinder formed by the oscillator body and the membrane, the relationship between the change in pressure $\dot{P}$ and the mass flow rate $\dot{m}$ is Equation 2.4:

$$\dot{P} = \frac{nRT}{V}\dot{m}$$

where n is the process constant, R the gas constant, T the gas temperature, and V the cylinder volume. The process is assumed to be adiabatic, following [Shearer, 1956], so $n = k$, the ratio of specific heats as above.

Pneumatic models corresponding to the cases where the magnetically actuated valve are open and closed are shown in Figure 4.5.

A simulation was constructed using these equations, with relevant parameters given in Table 4.1. A representative trajectory is plotted in the upper half of Figure 4.6. With the membrane at its leftmost position of travel, the magnet embedded in the membrane holds the magnetically-actuated valve open, as shown in the left of Figure 4.4. The pressure in the working chamber begins

parameter	symbol	10:1 prototype	proposed 1:1
supply pressure	P_s	1.9 atm abs	2.0 atm abs
reference pressure	P_{ref}	1.25 atm abs	1.25 atm abs
exhaust pressure	P_{ex}	1 atm abs	1 atm abs
gas temperature	T	293 K	293 K
ratio of specific heats	k	1.4	1.4
valve diameter	D_c	0.66 mm	0.5 mm
discharge orifice diameter	D_d	0.41 mm	0.2 mm
contraction coefficient	C_c	0.6	0.6
valve switching threshold		0.25 mm	0.1 mm
cylinder diameter	D_{cyl}	24 mm	3 mm
cylinder initial volume	V_0	4500 mm^3	20 mm^3
membrane modulus	E_{mem}	400 kPa	400 kPa
membrane Poisson ratio	ν_{mem}	0.5	0.5
membrane radius	a_{mem}	12 mm	1.5 mm
membrane thickness	h_{mem}	2 mm	0.5 mm
membrane travel	x_{mem}	$0 - 2.5$ mm	$0 - 0.5$ mm
magnet radius	R_{mag}	2.38 mm	0.75 mm
magnet length	L_{mag}	7.94 mm	1 mm
residual flux density	B_r	0.575 T	0.64 T
magnet separation	L	13.44 mm	2.3 mm
magnet travel	x_{mag}	$1.5 - 4.0$ mm	$0.4 - 0.9$ mm
oscillation frequency	f	10 Hz	350 Hz
dielectric thickness	d_{es}	3 μm	2.5 μm
relative permittivity	ϵ	2	2
applied voltage	V_{es}	180 V	180 V
clamp pressure	P_{es}	32 kPa	46 kPa
clamp capacitance	C_{es}	2.7 nF	50 pF
theoretical power consumption for electrostatic clamp	P	0.44 mW at 5 Hz	160 μW at 100 Hz

Table 4.1: Simulation parameters for 10:1 scale prototype and proposed at-scale device.

at atmospheric pressure, and increases until the pressure difference across the membrane is great enough to overcome the attractive force between the embedded magnet and the valve, whereupon the membrane snaps to the right. As noted previously, this provides the desired hysteresis. With the membrane at its rightmost position, the valve closes and the working chamber pressure falls until the pressure difference is great enough to overcome the attractive force between the embedded magnet and the steel piece in the reference chamber, as shown at the right of Figure 4.4. The membrane then snaps to the left, and the cycle repeats. Note from the times indicated on the state trajectory that the snapping action happens relatively quickly compared to the charging and discharging times of the working chamber.

In an analogy to the electrical oscillator mentioned previously:

- once the membrane has crossed the center position, the magnet force provides the snap action that corresponds to the high gain of the desired hysteretic relation,
- while the membrane is at its extremes of travel, the membrane modulus and thickness, together with the magnet force, determine the pressures at which the membrane switches position,
- and the volume of the working chamber, the diameters of the magnetically-actuated valve and the discharge orifice, and the supply and exhaust pressures set the switching frequency.

Simulation results, with parameters set according to Table 4.1, have been compared to actual results from a 10:1 scale prototype of this oscillator, shown in Figure 4.7. The prototype, with the supply and reference pressures set appropriately and with the correct discharge orifice attached to the entire system, has been observed to oscillate without failure at $5 - 6$ Hz for approximately 15000 cycles, a portion of which is shown in Figure 4.8. Comparing Figure 4.9 with Figure 4.8, the simulation oscillates at approximately twice the frequency actually observed in the prototype, which is within reasonable limits.

Possible sources of error include:

- the membrane model may not be applicable for large strain conditions,

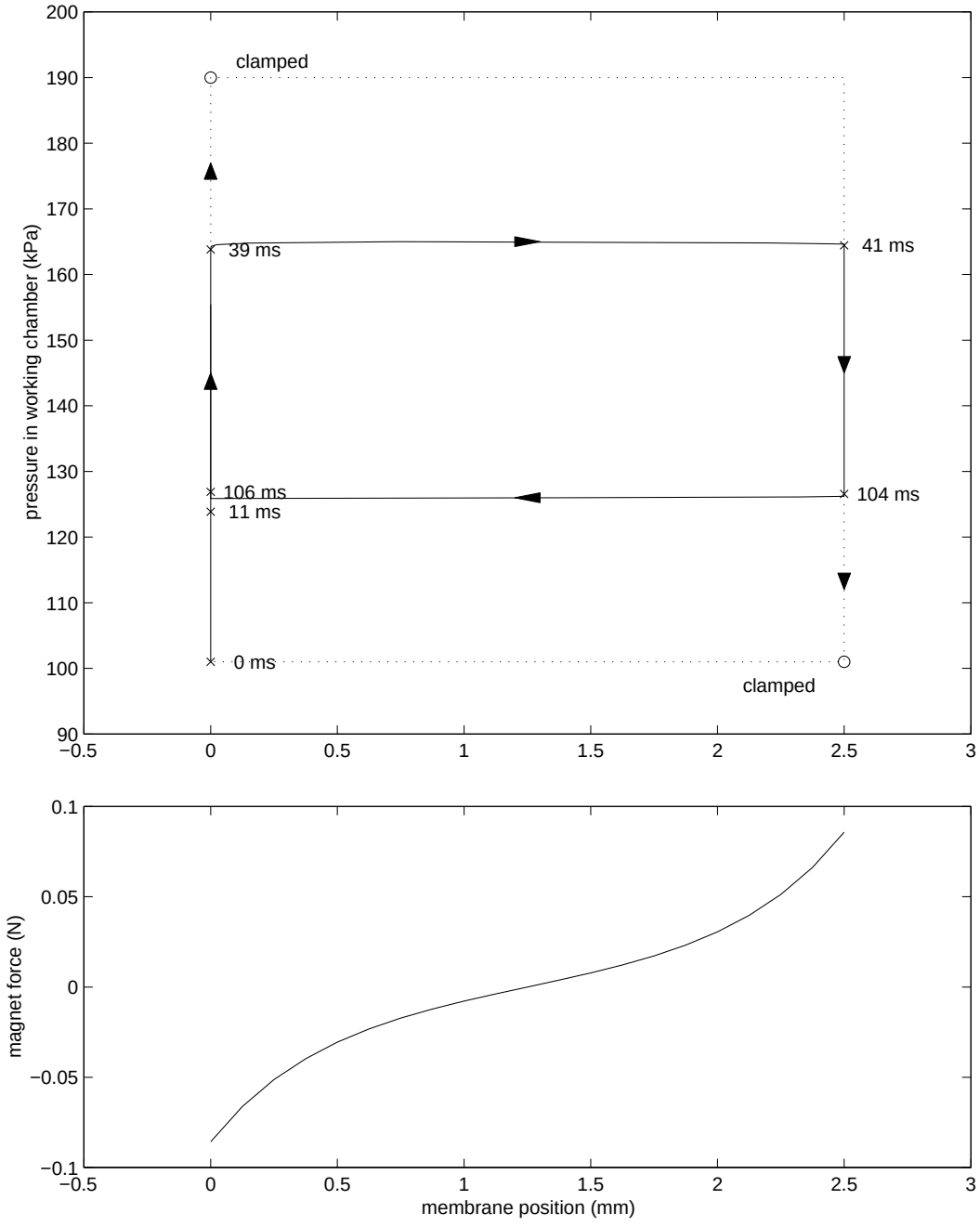

Figure 4.6: Simulated state trajectory (solid line in upper plot), relating membrane position and pressure in the working chamber, with force on membrane due to magnetic attraction between the embedded magnet and steel endpieces plotted below. When the membrane is clamped at either end of its travel, the system follows the dotted trajectory, and stops at the circled points in state space; when released, the system continues to follow the dotted trajectory until it rejoins the solid state trajectory. A position of 0 mm corresponds to the situation illustrated in the left of Figure 4.4, and a position of 2.5 mm corresponds to that illustrated in the same figure at the right.

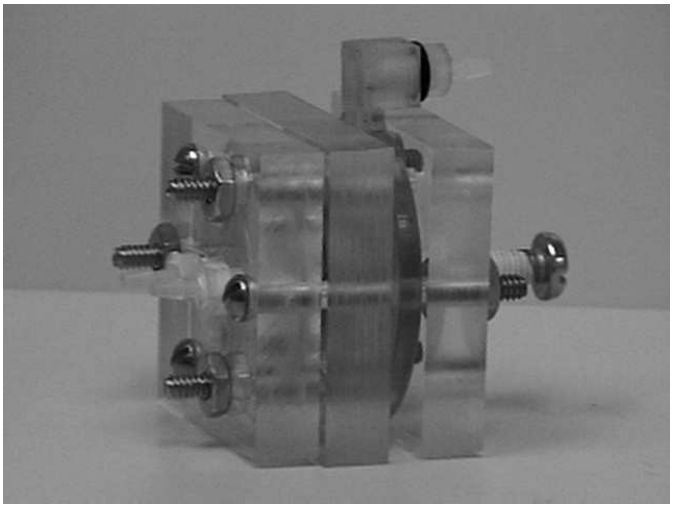

Figure 4.7: 10:1 scale prototype of the pneumatic oscillator, with dimensions 40x40x30 mm^3.

- the shape of the membrane forming one side of the variable volume cylinder is modeled as a cone,
- the magnet parameters are unverified, due to lack of a gaussmeter,
- the pressure losses through lines are unmodeled,
- the reference pressure is modeled as constant,
- and the magnetically actuated valve is modeled as being either open or closed, with a contraction coefficient of 0.6.

Oscillation in the simulation was not observed except for certain critical parameter values, indicating that the simulation is very sensitive to those parameters. Another major problem is that the peak magnet force was measured to be 1.1 N, as opposed to the 85 mN of the simulation. This discrepancy is most likely due to the assumptions made in the modeling of the membrane.

4.4 Electrostatic Clamp

Although the electrostatic clamp[Monkman, 1988] is as yet unfabricated, simulation results indicate that the oscillator prototype can be held at either end of its travel by a potential difference

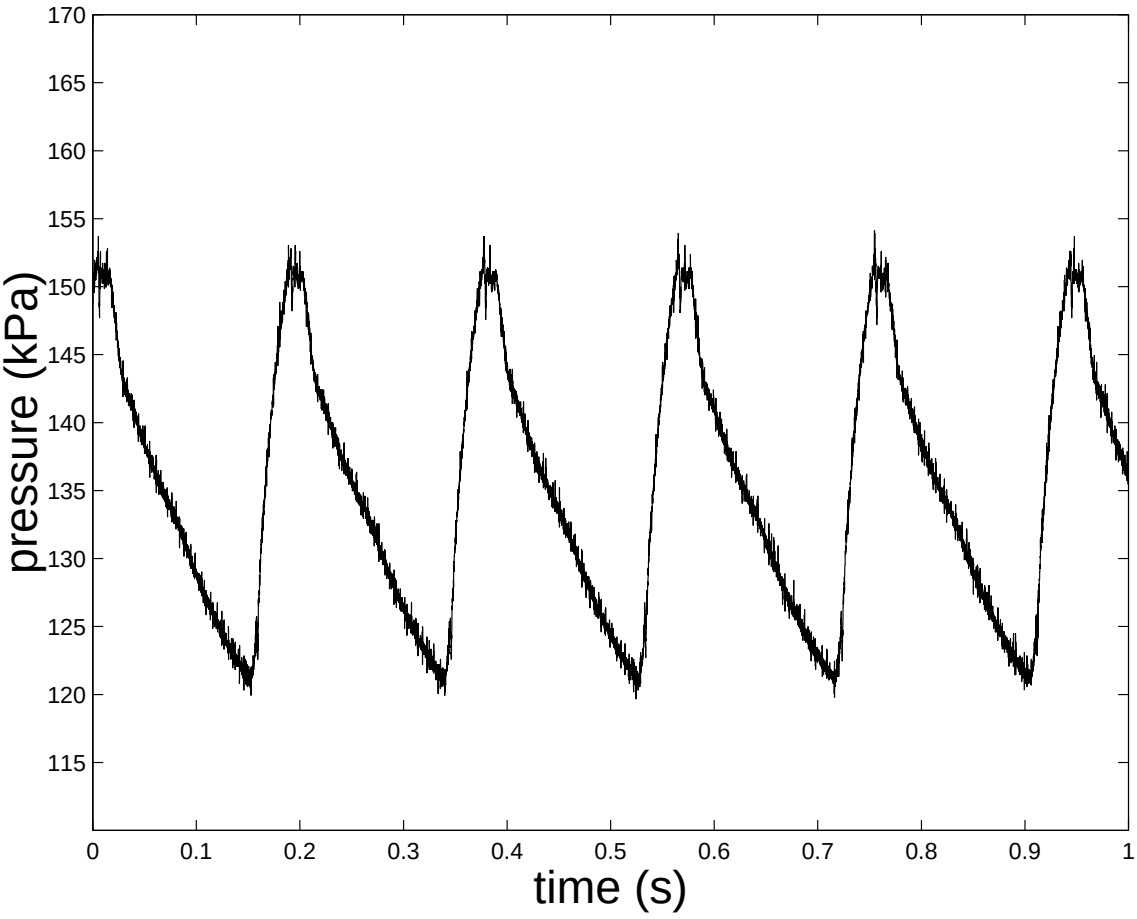

Figure 4.8: Pressure in the working chamber as a function of time for the 10:1 scale prototype of the pneumatic oscillator. The frequency of oscillation is thus correspondingly lower than the intended 100 Hz, because the cylinder volume is 500 times larger. The waveform is also asymmetric because the charge and discharge orifices have different diameters.

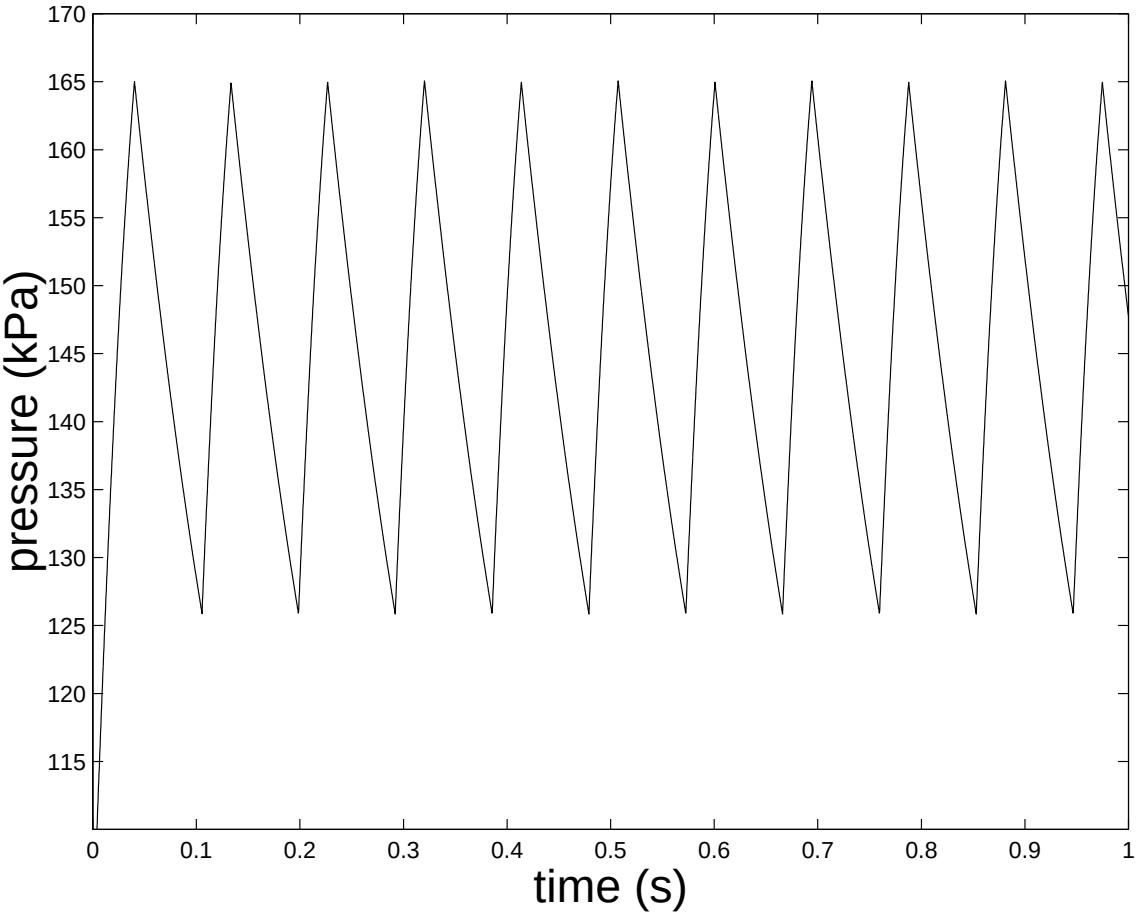

Figure 4.9: Pressure in the working chamber as a function of time for the simulation of a 10:1 scale prototype of the pneumatic oscillator. The oscillation frequency is twice that of the actual prototype, for reasons noted in the text.

V of 180 V applied across a dielectric with a permittivity ϵ of 2, with a thickness d of 3 μm. With this potential applied, the clamp exerts an equivalent pressure of $P_{es} = \frac{1}{2}\epsilon\epsilon_0(\frac{V}{d})^2$, or 32 kPa.

The clamping works because the equivalent pressure of the clamp adds to the pressure difference across the membrane. Consult Figure 4.6 and consider the case when the membrane is at 0 mm, and the working chamber pressure is at 125 kPa; if the clamp is applied then, the pressure in the working chamber, which ordinarily would rise to 165 kPa, would need to rise to 197 kPa before the membrane would snap away from the magnet and move to the 2.5 mm position. However, because the supply pressure is set to 190 kPa, that critical pressure would not be reached, effectively clamping the membrane at 0 mm. A similar argument can be made for the 2.5 mm position; with the clamp applied, the working chamber pressure would need to fall below $125 - 32$, or 93 kPa, but the exhaust pressure is set to 101 kPa.

Such an electrostatic clamp could be constructed by making the membrane out of a conducting material, and using the valve body as the other electrode. The valve body could be coated with a thin layer of dielectric material, and the potential difference applied across the membrane and body. For the 10:1 scale prototype switching at $f = 5$ Hz, the capacitance is $C_{es} = \frac{\epsilon\epsilon_0 A}{d}$, or 2.7 nF, and the power consumed is $P = C_{es}V^2 f$, or 0.44 mW.

4.5 Hybrid Actuator, Milliscale

Simulations were also performed with parameter values set for an at-scale prototype of the hybrid actuator, as given in Table 4.1. In all other respects, the model was the same as that for the 10:1 scale prototype, including a quasi-static membrane model. An oscillation frequency of approximately 350 Hz was predicted from the simulation results, although whether the quasi-static assumption can be said to hold is questionable. In addition, because the peak magnet force from the actual 10:1 scale prototype was an order of magnitude off from that of the simulation, extrapolation of the model to at-scale dimensions is also suspect.

However, the electrical oscillator, upon which the pneumatic oscillator is based, is in general robust to parameter variations, provided the gain of the Schmitt trigger is high enough. By appropriate membrane design and choice of magnet parameters, high gain can be achieved.

4.6 Conclusions/Future Work

Initial investigation of the oscillator and simulation seem encouraging, but the electrostatic clamp has not been implemented. Theoretical calculations for the clamp indicate the potential of the idea of driving a secondary actuator with an alternate power source and braking that secondary with an electrically-driven primary actuator, but the true test will come in the implementing and demonstrating a complete prototype that has both oscillator and clamp. Constructing the electrostatic clamp may be prove to be difficult, because of the thin coating and high field strength that would be required.

For an at-scale prototype, in addition to the clamp being a problem, embedding small magnets in the membrane that are sufficiently strong to provide hysteresis may also prove to be problematic.

Application of the hybrid actuator is more straightforward. The oscillating pressure in the working chamber can be tapped to drive another actuator, as long as it does not heavily load the oscillator. Perhaps an even simpler method might be to replace the steel piece in the reference chamber with another magnetically-actuated valve, which can then be driven in a pulse-width modulated fashion. If such a valve were to be attached, metering a 2 atm absolute pressure at a flow rate of 25 ml/s, the resulting milli-actuator potentially would have a power gain of 1100 from electrical to mechanical power at an operation frequency of 100 Hz.

Overall, initial results will need to be expanded upon before a definitive statement about this idea can be made. However, the design has a large number of degrees of freedom, specifically in the choice of magnet and membrane parameters. More generally, other mechanisms with hysteresis

may be employed, and certainly there is much room for further optimization.

Chapter 5

Conclusions

In order to actuate our tactile display with pneumatics, a microvalve array was necessary. Unfortunately, none of the commercially available valves was of the right size to satisfy our volume specification. Once the decision was made to fabricate our own valves, we needed an appropriate valve design.

Designing a valve requires an understanding of pneumatics. After examining the basic pneumatic elements, we discussed the major valve types and the force, displacement, and power required to actuate each type. In particular, single stage valve designs require greater forces and displacements that are difficult to obtain from conventional MEMS actuators.

However, multistage designs with primary and secondary actuators seemed promising. Specifically, we employed fluid power to drive the secondary actuator, and some sort of brake or clamp as the primary actuator. The fluid moves some slider or poppet, and the brake or clamp stops that element in one of two positions, to either keep the slider or poppet open or closed. The key idea is that although the brake may require a force on the same order as a single stage design, the stroke required may be significantly lower.

The turbine brake valve was the rotary version of this scheme, and the oscillator/clamp was the linearly reciprocating version. Although both showed promise, the TBV was rejected because

of the extremely tight tolerances needed and the resulting complicated alignments required. The oscillator/clamp could be made with looser tolerances, but its reduction to the desired at-scale dimensions will be future work.

Recently, multistage valve designs [Wang, 2000] have appeared to be a competitive alternative to the ideas proposed in this dissertation. Following the discussion of Section 2.5, consider a two-stage valve design with a secondary orifice of 0.5 mm in diameter, and a primary orifice with $\frac{1}{100}$ of the cross-sectional area of the secondary. The primary orifice is then 50 μm in diameter. Assuming that the primary experiences a worst case pressure difference of 5 atm, $A\Delta P$ is used to estimate the maximum force necessary to actuate the primary; the desired force is then 0.99 mN. $\frac{D}{4}$ can then be used to estimate the necessary displacement to arrive at the desired value of 12.5 μm.

Using the equations of Section 3.2.6, we can then sweep through all possible parallel piezoelectric bimorph dimensions, with length ranging from 1 to 10 mm in increments of 0.2 mm, width ranging from 0.1 to 2 mm in increments of 0.1 mm, and thickness ranging from 0.1 to 2 mm in increments of 0.1 mm. The resulting bimorph that meets the desired force and displacement with the minimum power consumption is 7.6 mm by 0.6 mm by 0.2 mm; with an applied voltage of 20 V, the bimorph exhibits a blocked force of 2.1 mN, a free displacement of 25 μm, and a power consumption of 56 μW at 100 Hz. The bimorph has a resonant frequency of 1.6 kHz, giving a lower bound on the actuation time of 0.61 ms. The best case times for the secondary can be estimated from the charging time from 1 atm absolute to 6 atm absolute and the discharging time from 6 atm absolute to 1 atm absolute for a fixed volume cylinder with a diameter of 1 mm and a height of 0.125 mm; this diameter is chosen because it provides for both the inlet and outlet orifices on the secondary, and the height is chosen because it is one quarter of the diameter of the secondary orifice. The resulting charging time for this volume is 325 μs, and the associated discharging time is 610 μs.

Table 5.1 provides a side-by-side comparison of four possible valve designs: the piezoelectric bimorph flap valve of Subsection 3.3.4, the at-scale turbine brake valve, the at-scale oscillator/clamp, and the two-stage design discussed above. Each of the multistage valve designs appears to be within

parameter	bimorph flap valve	turbine brake valve	oscillator/clamp	piezo primary, pneumatic secondary
dimensions	17.5×8 $\times 1$ mm^3	5×3 $\times 2$ mm^3	4×4 $\times 4$ mm^3	7.6×2 $\times 2$ mm^3
orifice diameter	0.5 mm	0.5 mm	0.5 mm	0.5 mm
turn-on/turn-off time	1.6 ms	1.1 ms	2.9 ms	$\approx$ 0.9 ms/1.2 ms
theoretical power consumption	54 mW	56 μW	160 μW	56 μW

Table 5.1: A theoretical comparison of a single stage piezoelectric bimorph flap valve, the at-scale turbine brake valve, the at-scale oscillator/clamp, and a two-stage piezoelectric primary valve with pneumatically-driven secondary. The dimensions given are estimates of the overall volume required, and it is assumed that both the bimorph flap valve and two-stage design can be actuated in less than 1 ms.

the same order of magnitude of power consumption. As for ease of fabrication, the piezoelectric primary with pneumatically driven secondary would be the hands-down winner, although contamination and sealing issues also need to be taken into account, since the primary orifice would be 50 μm across, necessitating good filtering of the compressed air. In addition, two primary valves would need to be constructed, although a single primary and discharge orifice can be used with some loss in the flexibility of the resulting control scheme. It is surprising that the piezoelectric primary valve with pneumatically-driven secondary has not been seen more frequently in the literature, other than in [Wang, 2000], because of the advantages it promises.

The idea of the electrically-driven brake with fluid-driven secondary still appears to have some merit. However, there is much work left to be done, most clearly of which is the fabrication of a working at-scale prototype of either the turbine brake valve or the oscillator/clamp. Theoretical calculations indicate that the idea holds promise, with power requirements more than two orders of magnitude lower than traditional single stage valves. The designs presented here take advantage of the fact that the actuators required need high force, but little stroke. However, whether or not the theoretical claim is borne up by experimental results is another story.

Bibliography

[Andersen, 1967] BW Andersen, *Analysis and Design of Pneumatic Systems*, New York: John Wiley and Sons, 1967.

[Ben-Dov, 1995] D Ben-Dov, SE Salcudean, "A Force Controlled Pneumatic Actuator," *IEEE Trans. on Robotics and Automation,* vol. 11, no. 6, pp. 906–911, December 1995.

[Blackburn, 1960] JF Blackburn, G Reethof, JL Shearer, *Fluid Power Control,* Cambridge: MIT Press, 1960.

[Caldwell, 1999] DG Caldwell, N Tsagarakis, C Giesler, "An Integrated Tactile/Shear Feedback Array for Stimulation of Finger Mechanoreceptor," *IEEE International Conference on Robotics and Automation,* Detroit, MI, May 1999, vol. 1, pp. 287-292.

[Carrozza, 1996] MC Carrozza, L Lencioni, B Magnani, P Dario, D Reynaerts, MG Trivella, A Pietrabissa, "A microrobot for colonoscopy," *MHS'96 Proceedings of the Seventh International Symposium on Micro Machine and Human Science,* Nagoya, Japan, 2–4 October 1996, pp. 223–228.

[Cengel, 1998] YA Cengel, MA Boles, *Thermodynamics: An Engineering Approach,* New York: McGraw-Hill, 1998, pp. 436.

[Cheung, 1997] P Cheung, AA Berlin, DK Bielgelsen, WB Jackson, "Batch Fabrication of Pneumatic

Valve Arrays by Combining MEMS with Printed Circuit Board Technology," *ASME MEMS 1997,* DSC-vol 62, HTD-vol 354, pp. 39–46.

[Chou, 1996] C-P Chou, B Hannaford, "Measurement and Modeling of McKibben Pneumatic Artificial Muscles," *IEEE Trans. on Robotics and Automation,* vol. 12, no. 1, pp. 90–102, February 1996.

[Cohn, 1992] MB Cohn, M Lam, RS Fearing, "Tactile feedback for teleoperation," *Proceedings of the SPIE – The International Society for Optical Engineering, Telemanipulator technology,* Boston, MA, USA, 15–16 November 1992, vol. 1833, pp. 240–54.

[Fearing, 1998] RS Fearing, "Powering 3 Dimensional Microrobots: Power Density Limitations," *1998 Tutorial on Micro Mechatronics and Micro Robotics, International Conference on Robotics and Automation.*

[Field, 1991] LA Field, *Fluid-Actuated Micromachined Rotors and Gears,* UC Berkeley PhD thesis, 1991.

[Goll, 1997] C Goll, W Bacher, B Bustgens, D Maas, R Ruprecht, WK Schomburg, "An Electrostatically Actuated Polymer Microvalve Equipped with a Movable Membrane Electrode," *Journal of Micromechanics and Microengineering,* vol. 7, no. 3, September 1997, pp. 224-226.

[Haji-Babaei, 1997] J Haji-Babaei, CY Kwok, RS Huang, "Integrable active microvalve with surface micromachined curled-up actuator," *Transducers '97,* Chicago, IL, 16–19 June 1997, pp. 833–836.

[Hayashi, 1975] S Hayashi, T Matsui, T Ito "Study of flow and thrust in nozzle-flapper valves," *Journal of Fluids Engineering,* vol. 97, no. 1, March 1975, pp. 39–50.

[Henning, 1997] AK Henning, J Fitch, D Hopkins, L Lilly, R Faeth, E Falsken, M Zdeblick, "A thermopneumatically actuated microvalve for liquid expansion and proportional control," *Transducers '97,* Chicago, IL, 16–19 June 1997, pp. 825–828.

[Hermida, 1998] A Hermida, "Deflection and Stresses in Circular Membranes Due to Transverse and In-Plane Loading Conditions," NASA Technical Brief GSC-14223.

[Hirano, 1997] M Hirano, K Yanagisawa, H Kuwano, S Nakano, "Microvalve with Ultra-Low Leakage," *Proceedings IEEE Micro Electro Mechanical Systems,* Nagoya, Japan, 26–30 January 1997, pp. 323–326.

[Hoerbiger-Origa] Hoerbiger-Origa, Piezo 2000 product literature, `www.hoerbiger-origa.com`.

[Johnston, 1991] DN Johnston, KA Edge, ND Vaughan, "Experimental Investigation of Flow and Force Characteristics of Hydraulic Poppet and Disc Valves," *Proceedings of the Institution of Mechanical Engineers, Part A: Journal of Power and Energy,* vol. 205, 1991, pp. 161–171.

[Kohl, 1999] M Kohl, KD Skrobanek, S Miyazaki, "Development of stress-optimized shape memory microvalves," *Sensors and Actuators A (Physical),* vol. A72, no. 3, February 1999, pp. 243–250.

[Landis/Staefa] Landis/Staefa, Digital Pneumatic Valve product literature, `www.landisstaefa.com`.

[Lee, 1996] AP Lee, J Hamilton, J Trevino, "A Low Power Tight Seal Polyimide Electrostatic Microvalve," *1996 Int. Mech. Eng. Cong. and Exposition, Microelectromechanical Systems,* DSC Vol. 59, Atlanta, 17–22 November 1996, pp. 345-349.

[Lee Company] Lee Company, High Density Interface 3-way solenoid valve product literature, `www.theleeco.com`.

[Lisec, 1996] T Lisec, M Kreutzer, B Wagner, "A Bistable Pneumatic Microswitch for Driving Fluidic Components," *Sensors and Actuators A (Physical),* vol. A54, no. 1–3, June 1996, pp. 746–749.

[Liu, 1988] S Liu, JE Bobrow, "An Analysis of a Pneumatic Servo System and Its Application to a Computer-Controlled Robot," *Journal of Dynamic Systems, Measurement and Control,* vol. 110, no. 3, September 1988, pp. 228–235.

[Louis, 1976] RJ Louis, E Logan, "Experimental Investigation of Flow-Induced Forces in Pneumatic Spool Valves," *Journal of Dynamic Systems, Measurement, and Control,* vol. 98, no. 3, September 1976, pp. 316–318.

[Lucas Novasensor] KR Williams, NI Maluf, EN Fuller, RJ Barron, DP Jaeggi, BP van Drieenhuizen, "A Silicon Microvalve for the Proportional Control of Fluids," *Transducers '99.*

[Magnet Sales and Manufacturing] Magnet Sales and Manufacturing Inc., *Magnet Design Guide,* `www.magnetsales.com`.

[Meckes, 1997] A Meckes, J Behrens, W Benecke, "Electromagnetically Driven microvalve Fabricated in Silicon," *Transducers 97,* Chicago, IL, 16–19 June 1997, pp. 821–824.

[Messner, 1998] S Messner, M Muller, V Burger, J Schaible, H Sandmaier, R Zengerle, "A Normally-Closed, Bimetallically actuated 3-Way Microvalve for Pneumatic Applications," *Proceedings MEMS 1998,* pp. 40–44.

[Monkman, 1988] GJ Monkman, PM Taylor, "Electrostatic Grippers, Principles and Practice," *Proceedings of the International Symposium on Industrial Robots,* April 1988, pp. 193–200.

[Morgan-Matroc] Morgan-Matroc piezoceramic product literature, `www.morganmatroc.com`.

[Moy, 2000] G Moy, C Wagner, RS Fearing, "A Compliant Tactile Display for Teletaction," *IEEE International Conference on Robotics and Automation,* April 2000.

[Nakada, 1980] T Nakada, Y Ikebe, "Measurement of the Unsteady Axial Flow Force on a Spool Valve," *Pneumatic and Hydraulic Components and Instruments in Automatic Control, Proceedings of the IFAC Symposium,* Warsaw, Poland, 20–23 May 1980, pp. 193–198.

[Ohnstein, 1990] T Ohnstein, T Fukiura, J Ridley, U Bonne, "Micromachined Silicon Microvalve," *Proceedings IEEE Micro Electro Mechanical Systems,* Napa Valley, CA, 11–14 February 1990, pp. 95–98.

[Orthwein, 1986] WC Orthwein, *Clutches and Brakes: Design and Selection,* New York: Marcel Dekker, 1986.

[Munson, 1994] BR Munson, DF Young, TH Okiishi, *Fundamentals of Fluid Mechanics,* New York: John Wiley and Sons, 1994.

[Pawluk] DTV Pawluk, CP van Buskirk, JH Killebrew, SS Hsiao, KO Johnson, "Control and Pattern Specification for a High Density Tactile Display," *7th Annual symposium on Haptic Interfaces for Virtual Environment and Teleoperator Systems, ASME IMECE,* Anaheim, CA, November 19-20, 1998.

[Peine/Howe] W Peine and R Howe, "Tactile Shape Displays for Small Scale Shape Feedback," `http://www.hrl.harvard.edu/~peine/display.html`.

[Redwood Microsystems] Redwood Microsystems, NC-1500 microvalve product literature, `www.redwoodmicro.com`.

[RMB Bearings] RMB Bearings, UL1304X stainless steel radial bearing product literature, `www.rmb-ch.com`.

[Robertson, 1996] JK Robertson, KD Wise, "An Electrostatically-Actuated Microvalve for Semiconductor Gas Flow," *Solid-State Sensor and Actuator Workshop,* Hilton Head, SC, 2–6 June 1996, pp. 148–151.

[Shearer, 1956] JL Shearer, "Study of Pneumatic Processes in the Continuous Control of Motion with Compressed Air-I," *Transactions of the ASME,* February 1956, pp. 233–242.

[Shikida, 1994] M Shikida, K Sato, "Characteristics of an electrostatically-driven gas valve under high-pressure conditions," *Proceedings IEEE Micro Electro Mechanical Systems,* Oiso, Japan, 25–28 January 1994 pp. 235–240.

[Shikida, 1996] M Shikida, K Sato, K Takeshita, S Suzuki, "Response time measurement of electrostatic S-shaped film actuator related to environmental gas pressure conditions," *Proceedings IEEE Micro Electro Mechanical Systems,* San Diego, CA, 11–15 February 1996, pp. 210–215.

[Shikida, 1997] M Shikida, K Sato, T Harada, "Fabrication of an S-shaped Microactuator," *Journal of Microelectromechanical Systems*, vol.6, (no.1), March 1997, pp. 18–24.

[Smelnitskii, 1972] SG Smelnitskii, AA Kalashnikov, VI Mindrin, "Investigation of the Hydrodynamic Forces Exerted on Valves of Control Systems," *Thermal Engineering,* vol. 19, no. 1, 1972, pp. 91–96.

[Stadler, 1995] W Stadler, *Analytical Robotics and Mechatronics*, New York: McGraw-Hill, 1995, pp. 321–338.

[Timoshenko, 1959] S Timoshenko, S Woinowsky-Krieger, *Theory of Plates and Shells,* New York: McGraw-Hill, 1959.

[TiNi Alloy] Tini Alloy Company, TiNi microvalve product literature, `www.sma-mems.com`.

[Trimmer, 1989] W Trimmer, R Jebens, "Actuators for Micro Robots," *IEEE International Conference on Robotics and Automation,* May 1989, pp. 1547–1552.

[Wang, 2000] G Wang, I Kao, "Intelligent Soft Contact Surface Technology with MEMS in Robotic and Human Augmented Systems," *IEEE International Conference on Robotics and Automation,* April 2000.

[Wang, 1999] XQ Wang, Q Lin, YC Tai, "A Parylene Micro Check Valve," *IEEE International MEMS 99 Conference* Orlando, FL, USA, 17–21 January 1999, pp. 177-182.

[Yang, 1997] X Yang, C Grosjean, YC Tai, CM Ho, "A MEMS Thermopneumatic Silicone Membrane Valve," *Proceedings IEEE Micro Electro Mechanical Systems,* Nagoya, Japan, 26–30 January 1997, pp. 114-118.

[Yang, 1999] X Yang, C Grosjean, YC Tai, "Design, fabrication, and testing of micromachined silicone rubber membrane valves," J-MEMS, IEEE, December 1999, pp. 393–402.

[Yang, 2000] F Yang, I Kao, "Analysis of Fluid Flow and Deflection for Pressure-Balanced MEMS Diaphragm Valves," *Sensors and Actuators A (Physical),* vol. A79, pp. 13–21.